UNIVERSITY OF CALIFORNIA
RIVERSIDE

# Inhibitory and Subcortical Contributions to Auditory Cortical Processing Deficits in Mouse Models of Fragile X Syndrome

A Dissertation submitted in partial satisfaction
of the requirements for the degree of

Doctor of Philosophy

in

Neuroscience

by

Mawaheb Kassir

June 2024

Dissertation Committee:
Dr. Khaleel Abdulrazak, Chairperson
Dr. Peter Hickmott
Dr. Jun-Hyeong Cho

The Dissertation of Mawaheb Kassir is approved:

_____

_____

_____

Committee Chairperson

University of California, Riverside

**Acknowledgements**

This study was funded by NIH/NICHD grant (1U54HD104461-01) and DOD/USARMY grant (W81XWH-19-1-0521). In addition, NIH/NIDCD fellowship (1F31DC019856-01A1) supported MHK in these studies. Funding was also provided by FRAXA Research Foundation. We thank members of the Razak lab for valuable discussions of the data and for providing comments on the manuscript.

ABSTRACT OF THE DISSERTATION

Inhibitory and Subcortical Contributions to Auditory Cortical Processing Deficits in Mouse Models of Fragile X Syndrome

by

Mawaheb Kassir

Doctor of Philosophy, Graduate Program in Neuroscience
University of California, Riverside, June 2024
Dr. Khaleel Abdulrazak, Chairperson

Autism spectrum disorder (ASD) is often associated with challenges in social communication and language delays, and it is characterized by sensory deficits such as hypo- or hypersensitivity. Auditory sensory hypersensitivity is a well-established phenotype of FXS, a leading genetic cause of ASD. Electroencephalogram (EEG) recordings show similar phenotypes in humans with FXS and in *Fmr1* knockout (KO) mouse models, namely increased baseline gamma power, impaired habituation of the event-related potential (ERP) in response to noise bursts, and reduced phase-locking to amplitude-modulated noise. These disruptions to auditory signals and sound processing may be a result of altered excitation and inhibition levels in the brain, and they may be differentially affected by cortical and subcortical auditory regions. Inhibitory and excitatory signals are associated with GABAergic neurons and glutamatergic signaling, respectively. In the present studies, we seek to identify the contribution of inhibitory neurons, namely parvalbumin-positive (PV) neurons, to sound processing in the AC, to

test whether targeting upregulated metabotropic glutamate activity (mGluR5) in FXS alleviates symptoms, and to further elucidate the role of subcortical auditory structures in regulating phase-locking to temporally modulated auditory signals. We found that PV neurons in the AC regulate resting gamma power and the 40-Hz click ASSR, while FMRP in the midbrain regulate temporal processing of gaps presented repeatedly in noise stimuli, presenting a double-dissociative role of the auditory cortex and midbrain. Furthermore, targeting mGluR5 in FXS showed benefits in resting gamma power when coupled with minocycline. These findings further our understanding of excitation and inhibition in auditory functioning in FXS and the differential contributions of cortical and subcortical regions.

**Table of Contents**

## List of Figures

## List of Tables

# Chapter 1: Introduction

The term “autism” often conjures up in our minds an image of developmental conditions involving social and cognitive challenges in young children. These challenges include social communication deficits, repetitive behaviors, hyper-anxiety, and language delays. Difficulty processing sensory stimulation does not typically come to mind first-hand, but it plays an essential role in autism spectrum (ASD) symptomology.

Sensory hypo- and hypersensitivity are present in children with ASD. For example, sensitivity to arbitrary noise is commonly cited as an anxiety-inducing factor in children with ASD. Auditory hypersensitivity reflects disruptions to neural mechanisms in the auditory pathway. A leading genetic cause of ASD characterized by sensory hypersensitivity is Fragile-X Syndrome (FXS). FXS is an X-linked monogenetic neurodevelopmental disorder that is present in 1 in 4,000 males and 1 in 8,000 females. It is caused by the absence of Fragile X ribonucleoprotein (FMRP) due to the silencing of the X-linked *Fmr1* gene. FMRP is an mRNA translation regulator and is involved in regulating neural morphology and function. Auditory sensory hypersensitivity is a well-established phenotype of FXS in humans and in *Fmr1*-knockout mouse models of FXS, and it can be electrophysiologically measured and characterized in humans and mice using electroencephalography (EEG). Auditory-evoked potentials and baseline neural activity are used to identify translationally relevant biomarkers and to characterize sensory deficits implicated in FXS and other autism spectrum disorders (ASD).

EEG records oscillatory changes in brain activity with high temporal precision. Neural oscillations in the brain are rhythmic changes in membrane voltage synchronized across a population of neurons associated with various sensory or cognitive processes;

they have become an established marker for observing brain states. Cortical rhythms likely reflect patterns of circuit excitation and inhibition, especially as relates to the temporal regulation of pyramidal cells elicited by local inhibitory interneurons as well as modulatory cortical and subcortical input (Merker, 2013; Buzsaki & Wang, 2012; Barth & MacDonald 1996; Metherate & Cruikshank, 1999; Sukov & Barth, 2001). Whether neural oscillations indicate cognitive processes or simply reflect excitation/inhibition balance involved in cortical processing remains an ongoing debate in the field (Merker, 2013; Buzsaki & Wang, 2012). In addition to these roles, neural oscillations may regulate precision of sensory processing, for the cortex displays measurable responses characterized by time-locked or phase-locked changes in oscillation as it receives and processes sensory stimuli. Common examples of these temporally locked responses are event-related potentials (ERP) and auditory steady state responses (ASSR). These measurements as well as resting brain activity provide markers for better understanding deficits that occur across different pathologies.

The auditory cortex (AC) is a key site in the central nervous system for processing sound stimuli across time (Wang et al., 2005). Both resting state and sound-evoked cortical oscillations are dictated by circuit level mechanisms, mediated in part by local interactions between pyramidal cells and gamma-amino butyric acid (GABA-)ergic inhibitory interneurons. Parvalbumin-positive (PV) interneurons comprise the largest subtype of inhibitory interneurons in the brain, and sensory-related changes in EEG in various sensory systems have been shown to be mediated by PV neurons (Chen et al., 2017; Veit et al., 2017; Cardin et al.. 2009; Kim et al., 2015). Furthermore, cross-cortical

modulations of the primary AC from the contralateral hemisphere (Nelson et al., 2013) and from secondary motor cortex (M2; Rock & Apicella, 2015) are mediated through PV neurons, producing feed-forward inhibition.

In the presence of sound stimuli, the cortex produces a response to the onset of a sound stimulus which, if averaged across many repetitions, creates the event-related potential (ERP). The ERP has distinct peaks that are thought to correspond to particular projections along the auditory pathway, namely thalamocortical projections (corresponding to P1), primary auditory cortical activity (corresponding to N1), and secondary auditory regions (corresponding to P2; Winkler et al., 2013). ERPs have been recorded across multiple species and are one of the most widely recorded auditory responses in humans. The ERP is useful for identifying central auditory deficits. It consists of the evoked component, which is phase-locked to the onset of the sound stimulus and across trials, as well as the induced component, which is non-phase-locked across trials and is characterized by long-latency (>100 ms post onset) changes in gamma and beta power compared to baseline. Changes in long-latency gamma power have been linked to stimulation of thalamocortical projections to the AC (Metherate & Cruikshank, 1999). Thalamic stimulation produces gamma oscillations in the AC (20-80 Hz in rats, 41-100 Hz in monkeys), and thalamic input to the AC modulates induced gamma band rhythm, which are likely mediated by local cortical inhibitory interneurons (Barth & MacDonald 1996; Metherate & Cruikshank, 1999), particularly PV neurons.

Temporal resolution and fidelity of auditory processing in the micro- to milli-second range is critical in speech processing and sound localization. The ASSR is used to

quantify phase-locking in the auditory cortex to an ongoing sound stimulus (e.g., a click train) with amplitude modulation occurring at a particular frequency. The phase locking factor is a measure of precision in temporal processing of the auditory system (Ross et al., 2003). ASSR in response to a modulation rate of 40 Hz has been well studied because of the robust phase-locked response that the auditory cortex produces (Galambos et al., 1981; Ross et al., 2003). The source of the ASSR recorded in the cortex is both cortical and subcortical, especially for modulation rates at 40 Hz (low gamma) and higher, respectively (Herdman et al., 2002). The ASSR is a useful stimulus for identifying the extent to which phase locking in the AC is impacted by conditions that involve alteration in excitation and inhibition levels (e.g., schizophrenia; Brenner et al., 2009) or aging-related effects on gap detection (Ross et al., 2010). PV neurons affect cortical responses to ongoing modulated stimuli and to gaps, both of which are key features of the ASSR stimulus. For instance, thalamocortical feedforward suppression to the auditory cortex is suppressed by PV cells (Phillips et al., 2017).

Key phenotypes present in humans and in global Fmr1 KO mouse models include increased power in resting gamma frequency, impaired habituation of the event-related potential (ERP) in response to noise bursts, elevated ERP amplitudes, and reduced phase-locking to amplitude-modulated noise (Ethridge et al., 2019; Lovelace et al., 2018). To alleviate neurodevelopmental sensory challenges in FXS, it is vital to (1) understand the underlying mechanisms of sensory processing deficits, (2) recapitulate the phenotypes in preclinical models, such as rodent models, to identify the best target strategies for treatment (3) and target and rescue these mechanisms successfully to pave the way for

medical treatment development. These key steps framed the research presented in this dissertation. The present research seeks to address the neural mechanisms underlying auditory sensory hypersensitivity in FXS and to further our understanding of ASD.

The first study presented identifies the role of PV neurons in the AC to resting-state EEG, ERP, and ASSR. Using chemogenetic inactivation of PV neurons alongside EEG recordings, we found that PV neurons are necessary to promote resting broadband gamma activity and the 40-Hz click ASSR in the AC. However, manipulating PV neuron activity in the AC does not alter the temporal precision of the gap-ASSR. This study helps to elucidate the underlying mechanisms of sensory processing deficits with respect to the role of cortical PV neurons in sound-evoked activity.

The second study presented tests the role of FMRP expression in the midbrain on sound-evoked activity and temporal processing in the AC and frontal cortex (FC). We measured EEG activity in mice with Cre-dependent midbrain deletion of FMRP. A series of previous studies (Lovelace et al., 2020a; Rais et al., 2022) using a similar approach to record EEG with forebrain-specific deletion of FMRP found that it recapitulated elevated resting gamma power, enhanced ERP, and non-phase-locked power during sound presentations present in FXS. With midbrain-specific deletion of FMRP, we found intact resting and sound-evoked activity in the AC, but temporal processing of gaps in noise was disrupted by the loss of FMRP in the midbrain. This study recapitulates specific phenotypes present in FXS, and, alongside the forebrain-deletion model, it provides an understanding of the differential contributions of the forebrain and midbrain expressions of FMRP to auditory sensory processing in the brain.

The third study presented targets a cellular pathway that is upregulated in FXS. The metabotropic glutamate receptor 5 (mGluR5) pathway is regulated by FMRP, and loss of FMRP results in upregulated translation of proteins downstream mGluR5. A number of studies have pointed to the mGluR5 pathway as a therapeutic target for treating FXS, from hippocampal slice work to audiogenic seizures and critical period development (Yan et al., 2005; de Vrij et al., 2008; Gandhi et al., 2014). We used a negative allosteric modulator of mGlurR5, CTEP, along with EEG to test whether reduction of mGluR5 expression rescues FXS phenotypes. Additionally, we tested combinatorial treatment approach by combining CTEP treatment with minocycline, an FDA-approved antibiotic that has been shown to improve FXS phenotypes and is associated with reduction of matrix metalloproteinase-9 (MMP-9) activity, which is upregulated in FXS and may disrupt inhibition by cleaving stabilizing extracellular matrix structures. We found that CTEP alone does not improve EEG phenotypes of FXS, but CTEP and minocycline in combination reduced elevated resting gamma power in the AC and FC. These effects are different than minocycline treatment alone, which improves phase-locking to temporally-modulated signals and reduces ongoing elevated gamma power during sound presentation (Lovelace et al., 2020b). Therefore, the combined treatment approach demonstrates that targeting multiple pathways, i.e., mGluR5 pathway and MMP-9, in FXS may have added or different beneficial effects compared to one drug alone, pointing to potential therapeutic effects of this approach for FXS.

In summary, in the following chapters, we used EEG in the *Fmr1*-KO model of FXS to test three key approaches to auditory hypersensitivity in FXS: elucidating underlying mechanisms at the circuit level by targeting inhibitory neurons, identifying the differential role of FMRP expression in the midbrain to temporal processing of sounds, and testing the benefits of combined treatment on EEG biomarkers of FXS. Collectively, our research provides insight on causes of auditory processing deficits in FXS and potential treatment approaches.

## References


Barth, D.S. and MacDonald, K.D., 1996. Thalamic modulation of high-frequency oscillating potentials in auditory cortex. *Nature*, *383*(6595), pp.78-81.

Brenner, C.A., Krishnan, G.P., Vohs, J.L., Ahn, W.Y., Hetrick, W.P., Morzorati, S.L. and O'Donnell, B.F., 2009. Steady state responses: electrophysiological assessment of sensory function in schizophrenia. *Schizophrenia bulletin*, *35*(6), pp.1065-1077.

Buzsáki, G. and Wang, X.J., 2012. Mechanisms of gamma oscillations. *Annual review of neuroscience*, *35*, pp.203-225.

Cardin, J.A., Carlén, M., Meletis, K., Knoblich, U., Zhang, F., Deisseroth, K., Tsai, L.H. and Moore, C.I., 2009. Driving fast-spiking cells induces gamma rhythm and controls sensory responses. *Nature*, *459*(7247), pp.663-667.

Chen, G., Zhang, Y., Li, X., Zhao, X., Ye, Q., Lin, Y., Tao, H.W., Rasch, M.J. and Zhang, X., 2017. Distinct inhibitory circuits orchestrate cortical beta and gamma band oscillations. *Neuron*, *96*(6), pp.1403-1418.

de Vrij, F.M., Levenga, J., Van der Linde, H.C., Koekkoek, S.K., De Zeeuw, C.I., Nelson, D.L., Oostra, B.A. and Willemsen, R., 2008. Rescue of behavioral phenotype and neuronal protrusion morphology in Fmr1 KO mice. *Neurobiology of disease*, *31*(1), pp.127-132.

Ethridge, L.E., De Stefano, L.A., Schmitt, L.M., Woodruff, N.E., Brown, K.L., Tran, M., Wang, J., Pedapati, E.V., Erickson, C.A. and Sweeney, J.A., 2019. Auditory EEG biomarkers in fragile X syndrome: clinical relevance. *Frontiers in integrative neuroscience*, *13*, p.60.

Galambos, R., Makeig, S. and Talmachoff, P.J., 1981. A 40-Hz auditory potential recorded from the human scalp. *Proceedings of the national academy of sciences*, *78*(4), pp.2643-2647.

Gandhi, R.M., Kogan, C.S. and Messier, C., 2014. 2-Methyl-6-(phenylethynyl) pyridine (MPEP) reverses maze learning and PSD-95 deficits in Fmr1 knock-out mice. *Frontiers in Cellular Neuroscience*, *8*, p.70.

Herdman, A.T., Lins, O., Van Roon, P., Stapells, D.R., Scherg, M. and Picton, T.W., 2002. Intracerebral sources of human auditory steady-state responses. *Brain topography*, *15*, pp.69-86.

Kim, T., Thankachan, S., McKenna, J.T., McNally, J.M., Yang, C., Choi, J.H., Chen, L., Kocsis, B., Deisseroth, K., Strecker, R.E. and Basheer, R., 2015. Cortically projecting basal forebrain parvalbumin neurons regulate cortical gamma band

oscillations. *Proceedings of the National Academy of Sciences*, *112*(11), pp.3535-3540.

Lovelace, J.W., Ethell, I.M., Binder, D.K. and Razak, K.A., 2018. Translation-relevant EEG phenotypes in a mouse model of Fragile X Syndrome. *Neurobiology of disease*, *115*, pp.39-48.

Lovelace, J.W., Rais, M., Palacios, A.R., Shuai, X.S., Bishay, S., Popa, O., Pirbhoy, P.S., Binder, D.K., Nelson, D.L., Ethell, I.M. and Razak, K.A., 2020a. Deletion of Fmr1 from forebrain excitatory neurons triggers abnormal cellular, EEG, and behavioral phenotypes in the auditory cortex of a mouse model of fragile X syndrome. *Cerebral cortex*, *30*(3), pp.969-988.

Lovelace, J.W., Ethell, I.M., Binder, D.K. and Razak, K.A., 2020b. Minocycline treatment reverses sound evoked EEG abnormalities in a mouse model of Fragile X Syndrome. *Frontiers in neuroscience*, *14*, p.550324.

Merker, B., 2013. Cortical gamma oscillations: the functional key is activation, not cognition. *Neuroscience & Biobehavioral Reviews*, *37*(3), pp.401-417.

Metherate, R. and Cruikshank, S.J., 1999. Thalamocortical inputs trigger a propagating envelope of gamma-band activity in auditory cortex in vitro. *Experimental Brain Research*, *126*, pp.160-174.

Nelson, A., Schneider, D.M., Takatoh, J., Sakurai, K., Wang, F. and Mooney, R., 2013. A circuit for motor cortical modulation of auditory cortical activity. *Journal of Neuroscience*, *33*(36), pp.14342-14353.

Phillips, E.A., Schreiner, C.E. and Hasenstaub, A.R., 2017. Cortical interneurons differentially regulate the effects of acoustic context. *Cell reports*, *20*(4), pp.771-778.

Rais, M., Lovelace, J.W., Shuai, X.S., Woodard, W., Bishay, S., Estrada, L., Sharma, A.R., Nguy, A., Kulinich, A., Pirbhoy, P.S. and Palacios, A.R., 2022. Functional consequences of postnatal interventions in a mouse model of Fragile X syndrome. *Neurobiology of Disease*, *162*, p.105577.

Rock, C. and junior Apicella, A., 2015. Callosal projections drive neuronal-specific responses in the mouse auditory cortex. *Journal of Neuroscience*, *35*(17), pp.6703-6713.

Ross, B., Draganova, R., Picton, T.W. and Pantev, C., 2003. Frequency specificity of 40-Hz auditory steady-state responses. *Hearing research*, *186*(1-2), pp.57-68.

Ross, B., Schneider, B., Snyder, J.S. and Alain, C., 2010. Biological markers of auditory gap detection in young, middle-aged, and older adults. *PLoS One*, *5*(4), p.e10101.

Sukov, W. and Barth, D.S., 2001. Cellular mechanisms of thalamically evoked gamma oscillations in auditory cortex. *Journal of Neurophysiology*, *85*(3), pp.1235-1245.

Veit, J., Hakim, R., Jadi, M.P., Sejnowski, T.J. and Adesnik, H., 2017. Cortical gamma band synchronization through somatostatin interneurons. *Nature neuroscience*, *20*(7), pp.951-959.

Wang, X., Lu, T., Snider, R.K. and Liang, L., 2005. Sustained firing in auditory cortex evoked by preferred stimuli. *Nature*, *435*(7040), pp.341-346.

Winkler I, Denhamb S, Escerac C. Auditory Event-related Potentials. Encyclopedia of Computational Neuroscience. (2013) Springer, New York, NY.

Yan, Q.J., Rammal, M., Tranfaglia, M. and Bauchwitz, R.P., 2005. Suppression of two major Fragile X Syndrome mouse model phenotypes by the mGluR5 antagonist MPEP. *Neuropharmacology*, *49*(7), pp.1053-1066.

# Chapter 2: Inactivating Parvalbumin Neurons in the Auditory Cortex Disrupts ASSR, Reduces Resting Gamma, and Elevates Beta Power in the Presence of Sound Exposure

**Abstract**

Functional deficits in GABAergic interneurons, namely parvalbumin-positive (PV) neurons, have been suggested in shaping electrophysiological changes in sensory circuits. PV neurons play a role in regulating the gain of stimulus-related responses and synchrony of neural responses in the cortex. However, the impact of altered PV neuron function on EEG biomarkers associated with hypersensitivity and sensory processing deficits, both stimulus-evoked and ongoing, is unknown. A particularly robust EEG biomarker is the auditory steady-state response (ASSR), which has been shown to be affected by gamma-amino butyric acid (GABA-)ergic neuron function and to reflect neural circuit dysfunction in multiple disease models including schizophrenia and autism spectrum disorders (ASD). In this study, we integrated electrophysiology and chemogenetics to manipulate the activity of PV neurons in the auditory cortex (AC) and to characterize changes to baseline resting neural oscillations, event-related potential (ERP) in response to noise bursts, and ASSR to amplitude-modulated sound stimulus. We injected a Cre-dependent adeno-associated virus (AAV) carrying designer receptors exclusively activated by designer drugs (DREADD) into the AC of PV-Cre mice. AC activity was recorded while mice were freely moving in a sound-insulated arena following a systemic injection of the DREADD ligand clozapine-*n*-oxide (CNO) or vehicle. We found that PV inactivation in the AC resulted in reduced gamma power in the resting EEG, elevated beta power during ongoing noise burst presentation, and reduced phase-locking of the ASSR to a 40 Hz click train. These changes are absent

when tested in control viral injections. This study generates novel insights into how interneuron dysfunction leads to altered sensory responses.

## 2.1 Introduction

Neural oscillations in the brain are rhythmic changes in membrane voltage synchronized across a population of neurons. Neural oscillations contain different frequencies of voltage fluctuations that are thought to reflect patterns of circuit excitation and inhibition involved with specific sensory, motor, and cognitive functions. The distribution of baseline EEG power across frequency ranges is altered in the auditory cortex (AC) of humans on the autism spectrum and mouse models of ASD, which is thought to reflect hyperexcitability in the cortex and altered inhibitory neuron function. However, the contributions of inhibitory neuron subtypes to the different frequency ranges and to ASD circuit pathophysiology remain debated.

The event-related potential (ERP) is one of the most recorded sensory responses in humans, and it is widely used as an objective electrophysiological marker to characterize sensory function biomarkers and to identify central deficits in neurodevelopmental and neurodegenerative disorders including autism spectrum disorders (ASD), schizophrenia, aging, and hearing loss. The ERP is a waveform representing the averaged EEG response following the repeated presentation of a stimulus. The ERP is characterized by distinct positive (abbreviated P1, P2, and P3) and negative (abbreviated N1 and N2) deflections that typically occur at specific latencies and reflect activity in different cortical projections along a sensory pathway (Winkler et al., 2013). The amplitude and latency of these deflections are useful for characterizing central auditory and other sensory deficits, and they have been used in humans and preclinical models across multiple species. For example, humans on the autism spectrum and mouse

models of ASD show altered P1 and N1 amplitudes of the auditory ERP (Modi & Sahin, 2017). In addition, humans with bipolar disorders may exhibit prolonged N2 latency and decreased P3 amplitudes in the visual ERP depending on the external emotions presented to them (Zhang et al., 2019). Changes in the ERP have been characterized in the aging human population, who often experience a decline in speech discrimination in noisy environments due to aging-related changes in the auditory system that are not yet entirely understood. ERPs of older adult humans performing audiovisual judgement tasks show decreased P1 and N1 amplitudes with aging (Setti et al., 2011). Observing these changes in the ERP provides translational biomarkers that can be further investigated in animal models to identify the underlying deficits in brain circuitry that impact sensory processing. Despite the widespread use of ERPs in characterizing translation-relevant biomarkers, very little is known about the circuit mechanisms that shape the ERP.

The ERP reflects synchronized neural firing in the cortex in response to stimuli, and the synchronization of these neural responses is likely guided by the action of inhibitory interneurons. gamma-amino butyric acid (GABA-)ergic interneurons, namely parvalbumin-positive (PV) neurons, play a role in regulating stimulus-related responses and synchrony of neural responses in the cortex (Kato et al., 2017; Phillips et al., 2017; Jang et al., 2020; Seay et al., 2020). In the cortex, PV neurons facilitate and synchronize bottom-up auditory signals and alters signal gain and tuning (Phillips et al., 2017; Jang et al., 2020; Seay et al., 2020). As, the impact of altered PV neuron function on the ERP remains unknown, we predict that inactivating PV+ neurons in the AC attenuates the

ERP under the hypothesis that PV neurons are necessary to facilitate and synchronize sensory signals reaching central regions of the auditory pathway.

Temporal resolution and fidelity of auditory processing in the micro- to milli-second range is critical in speech processing and sound localization. The auditory steady state response (ASSR) is used to quantify phase-locking in the AC to an ongoing sound stimulus (e.g., a click train) with amplitude modulation occurring at a particular frequency. The phase locking factor is a measure of precision in temporal processing of the auditory system (Ross et al., 2003). ASSR in response to a modulation rate of 40 Hz has been well studied because of the robust phase-locked response that the auditory cortex produces (Galambos et al., 1981; Ross et al., 2003). The source of the ASSR recorded in the cortex is both cortical and subcortical, especially for modulation rates at 40 Hz (low gamma) and higher, respectively (Herdman et al., 2002). The ASSR is a useful stimulus for identifying the extent to which phase locking in the AC is impacted by conditions that involve alteration in excitation and inhibition levels (e.g., schizophrenia; Brenner et al., 2009; Toso et al., 2024) or aging-related effects on gap detection (Ross et al., 2010). Activation of GABAergic signaling has been shown to enhance ASSR in the AC of humans (Toso et al., 2024), suggesting that inhibition enhances temporal fidelity of sensory signals in the cortex. PV neurons may play a crucial role in sensory temporal processing, as they can respond to ongoing stimuli after excitatory neurons show adaptation (Keller et al., 2017). Thus, in the present study we assess how ASSR is affected by PV cell inactivation in the AC. Furthermore, we use a gap-in-noise paradigm developed by Rumschlag & Razak (2021) to assess whether PV

neuron inactivation affects phase-locking to varied gap widths and amplitude-modulation depths, given their role in gap detection (Weible et al., 2014).

PV+ inhibitory neurons promote a broadband of frequencies in the local field potential (LFP) in the barrel and visual cortex (VC) that are canonically referred to as "gamma" (30-100 Hz; Cardin et al., 2009; Chen et al., 2017; Veit et al., 2017), which is further modulated by locomotion (Chen et al., 2017; although see Veit et al., 2017). Motor inputs from M2 to the primary AC synapse onto PV interneurons in the AC and ultimately produce an inhibitory effect, suggesting a relationship between auditory cortical signals and locomotion mediated through PV neurons. Thus, PV neurons in the AC have yet to be investigated in the mediation of resting state EEG and their effect across movement states.

Here, we measured the effects of PV neuron inactivation in the AC on sound-induced activity and baseline neural oscillations. In this study, we combined chemogenetic DREADD manipulations of PV cell activity in combination with electrophysiology to identify the impact of PV inactivation on auditory cortical oscillations in freely moving mice. We recorded EEG from epidural screw electrodes in the left and right AC in awake and freely moving mice to quantify power spectral density (PSD) across movement and sound-related activity in response to noise bursts and temporally dynamic signals.

We hypothesize that PV neurons in the AC promote broadband gamma in baseline EEG and promote the synchronizing of bottom-up auditory responses and the ASSR. We predict that silencing PV+ cell activity in the AC of mice will therefore

reduce resting gamma, attenuate ERP amplitudes, and reduce phase-locking of the ASSR. The understanding of PV cell contribution to the ERP, ASSR, and resting EEG will allow us to connect altered cellular processes to altered functional EEG measures.

## 2.2 Materials and Methods

Briefly, AAV8-hSyn-DIO-hm4Di-mCherry was injected into the right AC of a total of 20 C57 PV-Cre+ mice, and AAV5-hSyn-DIO-mCherry was injected into the right AC of 5 PV-Cre+ mice as controls. EEG recording screw electrodes were implanted onto the right and left AC and a reference electrode on occipital lobe. Following three weeks of recovery, clozapine-*n*-oxide (CNO) was injected intraperitoneally (IP) and EEG was recorded in each group, with vehicle injections and recordings to serve as within-subject controls.

### *2.2.1 Mice*

The study used C57/Bl6J male and female mice of the PV-Cre line at postnatal age P60-P90. Litters were obtained by breeding female $PV^{Cre/Cre}$ and male wild-type $PV^{-/-}$ mice to produce Het $PV^{Cre/-}$ male and female offspring, which the present study used at postnatal ages P60-P100. Pups were weaned at P21 and group-housed until surgery. Mice were maintained in an AAALAC accredited facility in 12 h light/dark cycles and fed standard mouse chow. All procedures were done according to NIH and Institutional Animal Care and Use Committee guidelines and approved protocols. Food and water were provided *ad libitum*. All mice were genotyped (Transnetyx, TN) using standard tail snip procedures.

### *2.2.2 Subjects*

Male and female PV-Cre C57Bl6/J mice were injected with AAV8-hSyn-DIO-hM4D(Gi)-mCherry, a neuron-targeting adeno-associated viral vector (AAV) carrying a

designer receptor exclusively activated by a designer drug (DREADD) in the form of a modified muscarinic G protein-coupled receptor that hyperpolarizes affected cells upon ligand (i.e., clozapine-*n*-oxide) binding (Roth, 2016). The AAV also carries a double-floxed inverse orientation (DIO) site consisting of a Cre-dependent lox-P site and an mCherry fluorescent protein for visualization. A control group of male and female mice of the same line were injected with AAV5-hSyn-DIO-mCherry, which carries the same components as the experimental vector but lacks the DREADD. This group served to control for procedural effects, namely potential effects of CNO on EEG in the absence of DREADD expression in the brain.

*2.2.3 Surgery*

At 2 mo. of age, mice underwent injection of the AAV and implantation of EEG screw electrodes in the right and left AC. Mice were anesthetized for the entire duration of the surgery via IP injections of 120 μg/g of ketamine and 5 μg/g of xylazine. The anesthetic state of mice was monitored through the toe pinch response tested every 10-15 mins. Half-dose supplements of ketamine were injected as necessary when mice showed signs of waking. Body temperature was monitored and maintained around 37° C using a rectal thermometer linked to temperature controller system connected to a heating pad (FHC Inc., ME). An ophthalmic ointment was administered to keep eyes moist throughout the procedure. Nair hair remover was applied on the head to remove hair and the skin was sterilized using alcohol wipes and gentle application of betadine. Prior to and after surgery, all surgical instruments and the bite bar used to support the mouse during surgery were ultrasonically cleaned with detergent to remove any trace of blood

and protein, then sterilized using a glass bead sterilizer then allowed to dry. An incision was made in the skin for skull exposure. 0.9% saline was applied to the skull intermittently to clean the skull and maintain moisture. A 1mm-diameter hole was drilled through the skull, exposing the right AC (4.5mm lateral, 2.2mm caudal to bregma).

*AAV Injection*. Using a Hamilton syringe and needle (model #1701), a total volume of 0.2ul of AAV was injected into the right AC at a depth of 300-600um (which approximates to laminar layers L2/3-L4 in the adult mouse) at a rate of 0.1ul/min (Stoica et al., 2013). The injections were made in 0.1uL increments, each at a different depth: the first injection of 0.1uL was made 600um deep in the primary AC (corresponding to L4), and the second injection of 0.1uL was made 300-400 um deep in the primary AC (corresponding to L2/3). Following AAV injection, 1mm-diameter holes were drilled above the left AC and occipital lobe.

*2.2.4 Electrode Implantation*

Following AAV injection, epidural screw electrodes connected to a three-channel headpost were installed above the right and left AC for recording and occipital lobe for reference. The right and left AC are connected through callosal projections that produce feed-forward inhibition facilitated by PV cells (Rock & Apicella, 2015). Recording from both hemispheres has direct relevance to our study, and we expect both hemispheres to be affected by the unilateral inactivation of PV cells during recording. Inactivating PV cells in the right AC may upregulate spike activity in the right AC, potentially enhancing the callosal input toward PV cells in the left AC. If PV cell activation promotes gamma

frequency power, we expect to see enhanced power in these frequencies in the left AC accompanied by reduced power in these frequencies in the right AC.

*Recovery*. Antibiotic ointment was applied around the incision site. Dental cement was applied onto the exposed skull and around the incision site, sealing the surgical site completely. Body temperature was further monitored until mice showed signs of waking. Upon waking, mice were administered with 0.1 ml buprenorphine subcutaneously. Surgical mice were placed, singly housed, in a new cage on top of a heat pad until fully awake and moving around. They were closely monitored for 48 hours, with buprenorphine, a potent analgesic (0.1 mg/kg body weight), administered subcutaneously approximately every 8 hours. Signs of recovery that were closely monitored include nest building and movement around the cage. Subsequently, they were allowed 3-4 weeks of recovery.

### *2.2.5 EEG Recording*

Following three weeks of recovery, CNO was systemically injected in mice 30 minutes prior to EEG recordings to elicit DREADD activation. Control recordings were preceded by vehicle injections. Mice received IP injections of 3mg/kg clozapine-*n*-oxide (CNO) in 0.5% dimethyl sulfoxide (DMSO) or vehicle (Roth, 2016).

The EEG recording and analysis methods are well established in the lab (Lovelace et al., 2018; Rumschlag et al., 2021). Electroencephalogram (EEG) recordings were collected and analyzed in 14 adult PV-Cre mice injected with adeno-associated virus AAV8-hSyn-DIO-hm4Di-mCherry and implanted with EEG screw electrodes in the auditory cortex

(AC), as well as 5 mice injected with AAV5-hSyn-DIO-mCherry as controls. Vehicle IP injections prior to recording served as within-subject controls within each group.

Following IP injections of CNO (or vehicle), awake and freely moving mice were placed in a plastic arena covered with bedding and surrounded by a wire mesh Faraday cage on a metal table inside a sound-insulated booth (Gretch-Ken Industries, OR). Mice were attached to an EEG cable via a freely rotating commuter tethered to the implanted headpost for recording. The cable was connected to a Tucker-Davis Technologies (TDT) RA4LI/PA head stage/preamplifier, which was connected via optic fiber to a TDT RZ6 I/O device. A TDT MF1 speaker placed 20 cm above the arena was connected to the RZ6 and played stimuli designed on OpenEx at a sampling rate of 24.414 kHz. Sound levels were calibrated using a ¼" Bruel and Kjaer (Nærum, Denmark) microphone. There were two recording channels (right and left AC) and a ground/reference channel (OC). TTL pulses marking stimulus onsets were recorded on a separate channel.

*2.2.6 Resting*

Following 10 minutes of habituation in the arena, resting EEG was recorded (5 minutes) during which no sounds were presented. Resting state EEG refers to signals recorded in the absence of sound presentation. Resting state EEG was recorded for five minutes, and recordings were divided into "move" and "still" based on Piezo movement detection and video analysis of mouse movement to allow for analysis of movement-related effects.

### *2.2.7 Event-related Potential*

After recording resting EEG, sound stimuli were repeatedly presented to record auditory ERPs. 1-12 kHz broadband noise bursts of 100 ms duration were played at 70 dB at a repetition rate of 0.25 Hz and a rise/fall rate of 5 ms for a total of 120 presentations. The ERP has been recorded across multiple species and is one of the most widely recorded auditory responses in humans for identifying central auditory deficits. The ERP displays two primary components: (1) changes in potential averaged across stimulus presentations, characterized by positive and negative deflections in the averaged response, (2) long-latency changes in power at specific frequencies, (3) total ongoing spectral power during noise burst presentation. Despite its widespread use and clinical relevance, the underlying circuit mechanisms that generate the ERP are unknown. We recorded auditory ERP amplitude and latency and non-phase locked induced power to identify how PV neurons modulate stimulus-related activity in the AC.

### *2.2.8 Auditory steady state response (ASSR)*

ASSR was recorded using an amplitude-modulated sound signal consisting of clicks presented at a rate of 40 Hz at 70 dB SPL. Each click train lasted 1 sec in duration. There were 200 repetitions of the click train. The 40 Hz ASSR has been used to study auditory temporal processing and is suggested as a biomarker in neurodevelopmental disorders such as schizophrenia (Thune et al., 2016) and autism spectrum disorders (Seymour et al., 2020). PV+ neurons in the frontal cortex (FC) have been shown to play a role in ASSR. Here we assess their role in the AC in regulating ASSR.

### *2.2.9 Gap-in-noise ASSR*

The 40 Hz gap-in-noise ASSR (henceforth, ‘gap ASSR’) stimulus uses gaps in continuous noise to elicit an ASSR. The stimuli consisted of 75 dB continuous noise periodically interrupted by 10 gaps placed 25 ms apart from onset to onset (for a presentation frequency of 40 Hz). A single stimulus began with 250 ms of noise, followed by 250 ms of gap-interrupted noise, followed by continuous noise, and so on, for a total of 10 presentations of the gap-interrupted noise. The stimulus ended with 250 ms of continuous noise, followed by a silent ISI of 500 ms. For each 250 ms segment, the gap width and modulation depth were randomly selected from a parameter space, consisting of 2-12 ms gaps (2 ms intervals) and modulation depths of 100%, 75%, and 50%, for a total of 18 possible combinations of gap width and modulation depth. Each stimulus was presented at least 100 times over the 35-minute presentation period. Gap-in-noise stimuli are commonly used to study auditory temporal processing acuity in humans and animals (Weible et al., 2014).

### *2.2.10 EEG Data Analysis*

Motion detection was achieved using a 27 mm piezoelectric pressure sensor (AW-PZT27L; Audiowell; Guangdong, China) placed beneath the arena. An infrared video camera was mounted above the arena to record mouse movements as the EEG recordings were made in the dark. OpenEx (TDT) was used along with the RZ6 to record EEG signals, record pressure signals, operate the LED light used to synchronize the video and waveform data, produce and store digital pulses, and to produce auditory stimuli. The EEG signals were captured at a sampling rate of 24.414 kHz and down-sampled to 1024

Hz. To correlate EEG power with movement, piezoelectric signals recorded during EEG recordings were analyzed for motion using a custom MATLAB script.

The EEG signal was transformed using a complex Morlet wavelet transform, with a constant wavelet parameter of 7, to provide instantaneous spectral power at frequencies ranging from 1–250 Hz.

*2.2.11 Resting EEG analysis*

The goal of resting EEG is to identify how power spectral density changes due to inactivation of PV+ neurons in the AC. We analyzed power spectral density (PSD) within each hemisphere of the AC. To measure PSD, each EEG trace was divided into 1 second segments with 50% overlap and Hanning-windowed to avoid edge artifacts and spectral splatter. The Fourier transform was used to extract the frequency content and calculate the average power across the different frequency bands: theta: 3-7 Hz, alpha: 8-13 Hz, beta: 14-29 Hz, low gamma: 30-60 Hz, and high gamma: 61-100 Hz (Rumschlag et al., 2020). The average power of each frequency bin across the 5-minute recording was calculated for each subject. A two-way analysis of variance (ANOVA) with Bonferroni's correction for multiple comparisons was used to analyze main effects of condition (CNO vs veh) across frequency bins.

*2.2.12 ERP analysis*

We previously published the analysis methods of ERP, ASSR, and gap ASSR and identical methods were used here (Rumschlag et al., 2021). Briefly, the ERP is the average of all recorded responses in the time-domain aligned to the stimulus onset. ERP

waveform provides insight into synchronized population activity resulting in distinct peaks (namely P1, N1 and P2) at specific latencies following sound onset. The event-related spectral perturbation (ERSP) was obtained by transforming the ERP from the time-domain into a time-frequency representation using the Morlet wavelet transform and baseline normalization of the EEG during segments at and until 1 s following presentation of noise bursts. Single trial power (STP) was obtained by using the Morlet wavelet transform and subtracting out sound-evoked changes in spectral power from baseline. Significant clusters were found using Monte-Carlo nonparametric permutations testing; a total of 2000 permutations were applied (Cohen, 2014; Rumschlag et al., 2021).

*ASSR, gap ASSR analysis.* ASSR and gap ASSR responses underwent Morlet wavelet transformation. ASSR facilitates a measurement of how well cortical generators synchronize to rapid temporal modulations in the signal. Inter-trial phase clustering (ITPC) is a value that reflects the fidelity of phase-locking to the temporal modulations across trials. ITPC was measured as a vector whose length represents the distribution of phase-locking values to an oscillating frequency across all stimulus presentations. ITPC was calculated for ASSR in response to clicks presented at a 40-Hz rate and was calculated for each combination of gap width and modulation depth. ITPC values are between 0 and 1; higher ITPC values indicate more consistent phase angles in EEG response to ASSR stimulus across trials. A two-way ANOVA was used to examine main effects and interaction of genotype, gap width, and modulation depth.

*2.2.13 Histology*

In total, mice were in the sound-insulated EEG recording arena for 70 minutes while EEG was recorded. At the end of the experiment, mice were euthanized with a lethal dose of sodium pentobarbital (i.p. injection, 125 mg/kg body weight). Absence of toe and pinna pinch reflexes were ensured before perfusion commenced. Mice were perfused with phosphate-buffered saline (PBS, 0.1 M) followed by 4% paraformaldehyde (PFA). The brains were extracted, incubated overnight in 4% PFA, incubated in 30% sucrose until they sank (~36–48 h at 4°C), cryoprotected, and sectioned into 40um slices on a cryostat (CM1860, Leica, IL, UK). Brain tissue were collected in a total of 20 adult PV-Cre mice injected with AAV8-hSyn-DIO-hm4Di-mCherry and 5 mice injected with AAV5-hSyn-DIO-mCherry. Six mice of the former injection group were analyzed for AAV transfection quantity and colocalization with PV cells in the injected location.

*2.2.14 Immunohistochemistry*

AC was identified using hippocampal landmarks. This method has been previously validated using tonotopic mapping and dye injection (Del Campo et al., 2012) and comparison with the Paxinos mouse atlas and other publications on mouse auditory cortex (Anderson et al., 2009). For each brain, an average of 6-8 slices containing AC were obtained. Sections were labeled using the following immunohistochemistry protocol. Briefly, free-floating brain slices were postfixed in 0.1 M PBS solution containing 0.1% sodium azide and then washed in 0.1 M PBS. Slices were then incubated in Permeabilization Solution (0.1M PBS, 3% Bovine Serum Albumin – Fisher Scientific catalog# 9 048468, 0.3% Triton X-100, 10% NaN3) at 4˚C for 6 hours with gentle

agitation, followed by overnight incubation with gentle agitation at 4˚C in primary antibody solution diluted in Permeabilization Solution supplemented with 5% normal donkey serum (NDS) to block nonspecific binding (250 uL per well in 24-well plate). The primary antibodies used were rabbit anti-dsRed (1:1000) to better enhance the mCherry signal, and mouse anti-PV (1:1000) to label PV interneurons. Slices were then washed three times for five minutes each in 0.1M PBS, followed by a 4-hour incubation with gentle agitation at room temperature in secondary antibody solution diluted in Permeabilization Solution supplemented with 5% NDS. Secondary antibodies used were donkey anti-rabbit 546 (1:1000) and donkey anti-mouse 488 (1:1000). Slices were washed three times for five minutes each in 0.1M PBS and mounted onto glass slides (Corning), dried upright, protected with Vectashield with a DAPI nuclei stain (Vector Labs, Burlingame, CA, USA, F2-135) mounting medium, covered by a glass coverslip, and sealed with nail polish.

*2.2.15 Imaging and Image Analysis*

Slices were imaged by confocal microscopy (model LSM 510, Carl Zeiss MicroImaging or Leica SP5) using a series of 20 high-resolution optical sections (1024 × 1024-pixel format) that were captured for each slice using a 10x or 20x objective (1.2 numerical aperture), with 0.6x zoom at 3 or 6 um step intervals (z-stack). Each z-stack was collapsed into a single image by projection (LSM Image Browser, Zeiss or Image J), converted to a TIFF file, cropped using ImageJ, and analyzed using ImageJ and Pipsqueak.

ImageJ/FIJI was used to obtain cell counts within laminar layers 1-5 of the AC by using the freehand selection tool and measure function to specify ROI. ROI was defined as the total area containing mCherry+ cells in the representative coronal section per brain. Pipsqueak PRO was used to identify and count PV-positive cells, mCherry-positive cells, and their colocalization. Biomarker-specific detection models "Parvalbumin" and "Somatic" were used for PV and mCherry, respectively, and detection sensitivity was set at 75 and overlap removal was set at 50. Semi-automatic detection was performed before manually selecting unmarked PV cells. Cell density of mCherry-expressing cells in the AC was calculated as (number of mCherry+ cells / area in $mm^2$). Percent colocalization of PV+ cells expressing mCherry in the ROI was defined as %colocalized expression / total PV+ cell count. The average percent colocalization in mice injected with the DREADD virus AAV8-hSyn-DIO-hm4Di-mCherry and with the control virus AAV5-hSyn-DIO-mCherry was 51% ± 21% (standard deviation; SD) and 79% ± 10% (SD), respectively. Example image of PV+ cells, mCherry+ cells, and an overlay to demonstrate colocalization is shown in **Figure 1**. AAV5-hSyn-DIO-mCherry was expressed in the sample image.

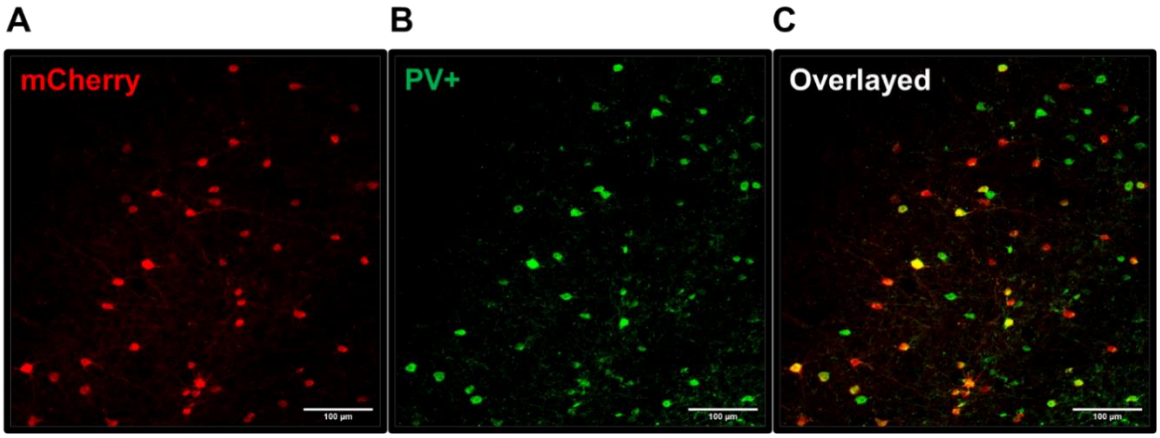


*Figure 2.1. Sample mCherry expression in PV+ cells at the injection site in the right AC*
Example image of (A) mCherry+ cells, (B) PV+ cells, and (C) an overlay to demonstrate colocalization. The average percent colocalization in mice injected with the DREADD virus AAV8-hSyn-DIO-hm4Di-mCherry and with the control virus AAV5-hSyn-DIO-mCherry was 51% ± 21% (standard deviation; SD) and 79% ± 10% (SD), respectively. This tissue was obtained from a mouse injected with AAV5-hSyn-DIO-mCherry. Scale bar is 100 µm.

### 2.3 Results

The main goal of this study was to quantify effects on resting and sound-related EEG with chemogenetic silencing of PV+ neurons in the AC in mice. PV-Cre mice on the C57 background were injected with DREADD-containing and Cre-dependent AAV to target PV cells in the right AC. PV cells have been shown in a wide set of studies that they regulate cortical oscillations in the brain, that they gate, facilitate, and/or tune bottom-up sensory responses including auditory signals in the cortex, and that they may be associated with various disease models/conditions in which temporal regulation of signal against noise may be implicated.

Clozapine-*n*-oxide was injected i.p. in mice prior to EEG recording to induce the inactivation of PV cells via DREADD action (n=14). As within-subject control, we injected mice with vehicle in a separate recording session and compared CNO vs veh in all the EEG measures shown below. Additionally, we recorded from a group of mice (n=5) that were injected with a control Cre-dependent AAV to reveal whether any effects seen in the AAV-DREADD group are due experimental procedure (e.g., CNO exposure) rather than inactivation of PV alone.

*2.3.1 PV+ neuron inactivation in the AC reduces resting gamma power in both hemispheres and increases theta power in the contralateral hemisphere*

Power spectral density (PSD; μV2/Hz) was analyzed within right and left AC to identify how spectral distribution in resting EEG was affected by PV neuron inactivation across movement states (**Figure 2**). The fast Fourier transform was applied to 1-s segments of the EEG trace to extract frequency content, and segments were separated into "move" and "still" based on the piezo and video analysis of the mouse's movement, in addition to analyzing the entire EEG trace ("all"). Frequency was divided into canonical frequency bands, and the average power was calculated for each band across the entire 5-minute resting recording (theta: 3-7 Hz, alpha: 8-13 Hz, beta: 14-29 Hz, low gamma: 30-60 Hz, high gamma: 61-100 Hz). ANOVA with Bonferroni's correction for multiple comparisons was used (we accounted for five frequency bands; $\alpha = 0.01$) to analyze main effects of condition (CNO vs veh) across frequency bins.

The right AC (injected) in AAV-DREADD mice showed significantly reduced high gamma power in the CNO condition (PV inactivation) compared to veh (Figure 2D

all: **p=0.0013; Figure 2E move: **p=0.0013; Figure 2F still: *p=0.0039). In the left AC of these mice, low gamma power was significantly reduced in the CNO condition compared to veh (Figure 2A all: **p=0.0013; Figure 2B move: *p=0.0068; Figure 2C still: *p=0.0045). These effects were seen across all movement states. In the left AC, theta power was increased in the "all" and "move" traces with CNO compared to veh, but this effect was absent in the "still" traces (Figure 2A all: *p=0.0050; Figure 2B move: p=0.0072; Figure 2C still: p>0.01). Theta oscillations in the brain are related to movement, and it is possible that the inactivation of PV neurons in the right AC prevented this movement-related change in theta to occur, especially considering that the motor cortex projects modulatory input onto the AC that act through PV neurons (Schneider et al., 2014). In the AAV-control mice, there were no significant differences in power across the frequency bands and across movement states in the CNO condition compared to vehicle (Figure 2G-L; all comparisons p>α), confirming that changes seen in the AAV-DREADD group are not due to procedural effects of the experiment.

### *2.3.2 PV+ neuron inactivation in the AC reduces auditory event-related potential (ERP) amplitudes in both hemispheres*

The ERP is the averaged EEG-recorded response to repeated presentation of noise bursts and is characterized by a distinct set of positive and negative deflections. Because it is the average response, all non-phase-locked activity is cancelled out, and we are left with positive (P) and negative (N) deflections that reflect the propagation of thalamocortical signal into the primary and secondary sensory cortical areas. The peaks of the ERP, named P1, N1, P2, and N2, are consistently timed and are evoked at specific

latencies after sound onset. Measuring the amplitudes and latencies of these waves allow for the assessment of response synchrony or hypersensitivity to sound presentation. The ERP is commonly used to characterize and identify human sensory processing deficits, and it is highly translational from animal models. In the present study we recorded ERPs during the presentation of 1-12 kHz broadband noise bursts, each lasting 100 ms and repeating every 4 s. The ERP is measured in the time-domain with respect to the stimulus onset (0 ms), and here it is averaged over 120 presentations from 0 to 250 ms post onset time. The amplitudes (μV) and latencies (ms) of the P1, N1, P2, and N2 fluctuations of the ERP were compared between CNO and vehicle conditions in the right and left AC in each group individually (AAV-DREADD and AAV-control) using paired Student's t-tests for each comparison (**Figure 3**). The ERP waveform of each group with CNO/veh conditions is shown in Figure 3 (Figure 3A, AAV-DREADD left AC; Figure 3B, AAV-DREADD right AC; Figure 3E, AAV-control left AC; Figure 3F, AAV-control right AC).

With the inactivation of PV neurons in the AC of AAV-DREADD mice, we found that P2 (Figure 2D; *p=0.0492) and N2 (Figure 2D; *p=0.0345) amplitudes were significantly reduced in the right AC (injected side) in CNO condition compared to vehicle. In the left AC (non-injected), there was a significant reduction in the P1 amplitude (Figure 2C; *p=0.0243) with CNO compared to veh. These effects were absent in the AAV-control group, as CNO had no significant effect on ERP amplitudes compared to veh. The latencies of the ERP positive and negative waves were also analyzed in the AAV-DREADD and AAV-control groups in the CNO condition

compared to vehicle for each respective group. The P1 latency (Figure 2D; **p=0.0054) was significantly increased in the right AC (injected) of AAV-DREADD mice in the CNO condition compared to vehicle, but it was unaltered in the left AC or in either hemisphere in the AAV-control group with CNO compared to vehicle ($p>0.05$ for all non-significant differences).

*2.3.3 PV+ neuron inactivation in the AC elevates power in beta frequency in the ongoing non-phase-locked power distribution during noise burst presentation.*

The inactivation of PV neurons in the AC during the repeated presentation of sound stimulation generates higher power in beta and lower frequencies in the right AC (injected hemisphere), but it does not alter phase-locked (induced) changes in power distribution. Non-phase-locked power is presented in a heat map on the time domain that represents ongoing power distribution across frequencies during repeated noise burst exposure (onset at 0 ms). We call this single trial power (STP; **Figure 4**). Additionally, we measure baseline-corrected changes in power across frequencies that are phase-locked to the time onset of the stimulus and across trials, which are the event-related spectral perturbations (ERSP; **Figure 5**). STP and ERSP are analyzed across 120 presentations of noise bursts, each presented every 4 s (onset at 0 ms; 100 ms duration) at 70 dB SPL, which is the same sound protocol and EEG trace that produced ERPs. These measures are important for identifying pathophysiological changes in spectral power distribution that may be characteristic to sensory processing deficits in disease models. In the present study, we seek to understand the contribution of PV neuron activity in the AC to these measures during sound exposure.

Figure 4A, B show the STP of AAV-DREADD injected mice in the CNO (top right panel) vs veh (top left panel) conditions, and the difference CNO-veh in the larger bottom panel, in the left AC (non-injected hemisphere, Figure 4A) and the right AC (injected hemisphere, Figure 4B). Monte-Carlo permutations (2000 total) were used to analyze clusters (contoured within the heat map) of frequencies along the time domain that are significantly different between the hemispheres. The left hemisphere shows no difference in STP between CNO and veh (Figure 4A), while the right hemisphere shows significant elevation in power in the beta and lower frequencies (<30 Hz) in the STP with CNO compared to veh. Stimulus-dependent beta frequency power is regulated (attenuated) by PV cells in the VC (Chen et al., 2017), and here we demonstrate a similar effect in the AC. These effects were absent in both hemispheres in the AAV-control group (Figure 4C, D), in which no significant clusters were present in right or left AC between CNO and veh comparisons.

Figure 5 shows the ERSP with CNO and veh conditions in AAV-DREADD (Figure 5A, B) and AAV-control mice (Figure 5C, D) in the left and right AC. There were no significant differences in ERSP between CNO and veh in the left (Figure 5A) and right (Figure 5B) AC of AAV-DREADD mice. However, in the AAV-control mice, significant clusters appeared in the CNO-veh panels in the left (Figure 5C) and right (Figure 5D) AC in a narrowband 60-80 Hz at around 500 and 750 ms post sound onset in the left AC (Figure 5C) and 750 ms post sound onset in the right AC (Figure 5D). These clusters may either be due to CNO exposure, or they may be offshoot results considering

that these effects were absent in the AAV-DREADD group when comparing CNO to veh. Significant clusters were found using Monte-Carlo permutation testing.

*2.3.4 PV+ neuron inactivation in the AC reduces phase-locking of the auditory steady state response (ASSR) to click train presented at 40 Hz repetition rate.*

The ASSR is spectrotemporally phase-locked to ongoing click trains, and it is useful in measuring phase-locking strength of cortical activity to temporally-modulated sound stimuli. PV+ neuron inactivation in the AC reduces phase-locking of the auditory steady state response (ASSR) to click train presented at 40 Hz repetition rate, but it does not affect phase-locking to gap-in-noise ASSR. Following noise-burst presentations, a 2-s click train presented repeatedly at a rate of 40-Hz was used to generate ASSR in the AC, recorded in the right and left AC of AAV-DREADD and AAV-control mice following CNO and veh injections. ASSR was evaluated by calculating inter-trial phase clustering (ITPC) which is a measure of consistency of phase angles of frequencies along the time domain across trials with respect to the click presentation. Across 200 trials, ASSR was averaged and differences between CNO and veh were analyzed in AAV-DREADD and AAV-control groups (**Figure 6**). Figure 6A, B show ITPC heatmaps of ASSR in the left (Figure 6A) and right (Figure 6B) AC of AAV-DREADD mice following CNO vs veh injections. As before, the top left panel in each subfigure represents ITPC in the veh condition, the top right panel represents CNO, and the bottom large panel is the subtraction CNO-veh. Monte-Carlo permutations were used to compare conditions across time and frequency: statistical cluster analysis reveals contiguous time × frequency (in this case, 40 Hz and its harmonics) regions that are significantly different between CNO

and vehicle conditions. Figure 6C shows the quantification of ITPC at 40 Hz across time (ms) during the 2-s duration of the click train. The top graph is ITPC in the right AC following CNO and veh injections, and the bottom graph is the left AC. (note for edits: typo on x-axis says “frequency” instead of “time”). There is reduced ITPC in the left (non-injected; Figure 6A) and right (injected; Figure 6B) AC with CNO compared to vehicle in the AAV-DREADD group, indicating that PV+ inactivation reduces phase-locking of the ASSR to 40-Hz click train. ITPC of the ASSR in AAV-control group is shown in the left AC (Figure 6D) and right AC (Figure 6E), and ITPC graphs are presented in Figure 6F. No significant clusters were found, indicating no differences in ITPC between CNO and veh were present in the control group.

Phase-locking to gaps-in-noise presented repeatedly at 40 Hz is unaffected by PV+ cell inactivation in the AC. The gap ASSR protocol was developed by our lab to provide complexity to the ASSR stimulus that allows for parameter changes, i.e., gap width and amplitude-modulation depth of gaps presented at a rate of 40 Hz in ongoing noise. We sought to test whether PV+ neurons in the AC, shown before to encode gap termination in the AC (Weible et al., 2014), play a role in regulating phase-locking to repeated gap presentation in ongoing noise. We found that phase-locking to gaps-in-noise presented repeatedly at 40 Hz is unaffected by PV+ cell inactivation in the AC (**Figure 7**). Example heat maps of ITPC across time during stimulus presentation are presented in Figure 7A-H, which represent mean ITPC to 12-ms gaps in noise with 100% AM in CNO and vehicle conditions in left and right AC of AAV-DREADD and AAV-control mice. The graphs in Figure 7I-P represent the average group ITPC for each gap width and

modulation depth in CNO and vehicle conditions. (Figure 7I, J, M, N) There is no significant effect of CNO on ITPC across gap widths for each modulation depth presented (100% AM, 75% AM) in the AAV-DREADD group or in the AAV-control group (Figure 7K, L, O, P). CNO effects were analyzed across gap widths using a two-way repeated measures ANOVA for each mouse group (condition x gap width) per modulation depth.

*Resting*

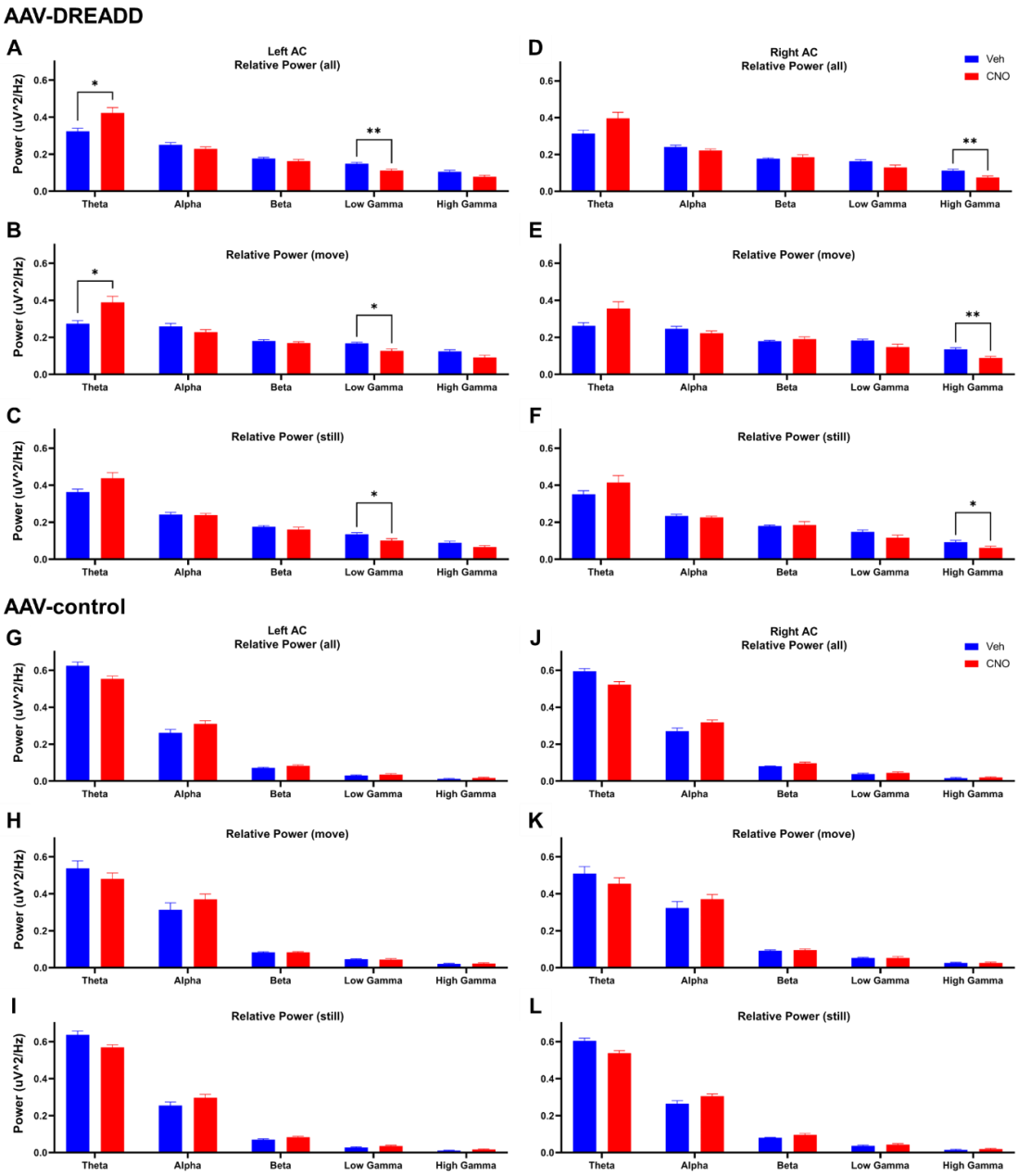
AAV-DREADD
A
Left AC
Relative Power (all)
D
Right AC
Relative Power (all)
Veh
CNO
B
Relative Power (move)
E
Relative Power (move)
C
Relative Power (still)
F
Relative Power (still)
Power (uV^2/Hz)
Theta
Alpha
Beta
Low Gamma
High Gamma
AAV-control
G
Left AC
Relative Power (all)
J
Right AC
Relative Power (all)
H
Relative Power (move)
K
Relative Power (move)
I
Relative Power (still)
L
Relative Power (still)

*Figure 2.2. Resting gamma power is reduced with PV+ cell inactivation in the injected and non-injected hemispheres of AC*

(A-C) The left hemisphere (non-injected) of the AC shows reduced low gamma power in all states of movement and increased theta power in the "all" and "move" states. (D-F) The right hemisphere (injected with AAV-DREADD) shows reduced high gamma power in all states of movement. (G-I) Resting EEG is not affected by CNO compared to vehicle in the left hemisphere (non-injected) of the AC or in the (J-L) right hemisphere (injected with AAV-control) of the AC across all movement states. Resting EEG was binned into six frequency bands, displayed on the x-axis. Power was averaged and relative power was calculated per frequency bin, displayed on the y-axis. n=14 mice with AAV-DREADD; n=5 mice with AAV-control. Multiple paired t-tests were computed with Bonferroni correction for multiple comparisons ($\alpha$=0.01). (A) Theta, *p=0.0050; Low Gamma, **p=0.0013 (B) Theta, *p=0.0072; Low Gamma, *p=0.0068 (C) Low Gamma *p=0.0045 (D) High Gamma, **p=0.0013 (E) High Gamma, **p=0.0013 (F) High Gamma, *p=0.0039. p>0.01 for all non-significant differences.

*Event-related potential (ERP)*

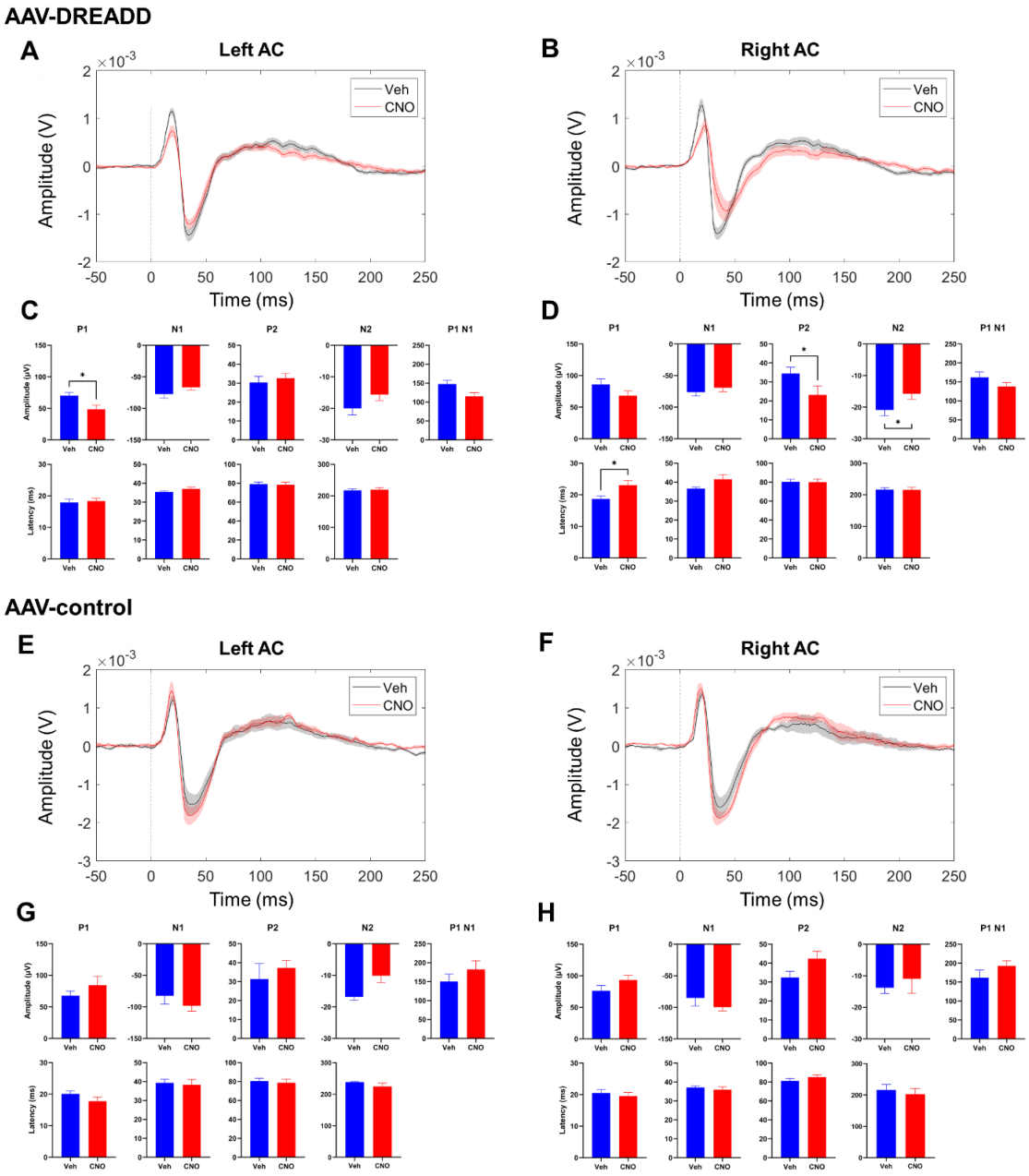

*Figure 2.3. The event-related potential (ERP) is altered by PV+ cell inactivation in the right AC (injected hemisphere) and left AC (non-injected hemisphere) and is unaffected in the control group*

(A, B, E, F) Average ERP waveform of the CNO and vehicle conditions in the (A, B) AAV-DREADD group and (E, F) AAV-control group in the left (non-injected) and right AC (injected), respectively. The positive (P) and negative (N) deflections in the order of their appearance (1, 2) of the ERP (C, D, J, H) Comparisons of amplitude and latency between CNO and vehicle conditions in the (C, D) AAV-DREADD group and (J, H) AAV-control group in the left (non-injected) and right AC (injected), respectively. (C) In the left hemisphere (non-injected) of the AAV-DREADD group, there is reduced P1 amplitude in the CNO condition compared to vehicle. (D) In the right hemisphere (injected) of the AAV-DREADD group, there is reduced P2 and N2 amplitude and increased P1 latency in the CNO condition compared to vehicle. (G, H) There is no difference in amplitude and latency of the positive and negative deflections of the ERP between CNO and vehicle in the AAV-control group. n=14 mice with AAV-DREADD; n=5 mice with AAV-control. Student's paired t-tests were computed for each comparison ($\alpha$=0.05). (C) P1 amplitude, *p=0.0243 (D) P2 amplitude, *p=0.0492; N2 amplitude, *p=0.0345; P1 latency, **p=0.0054. p>0.05 for all non-significant differences.

*Single trial power (STP) to noise burst*

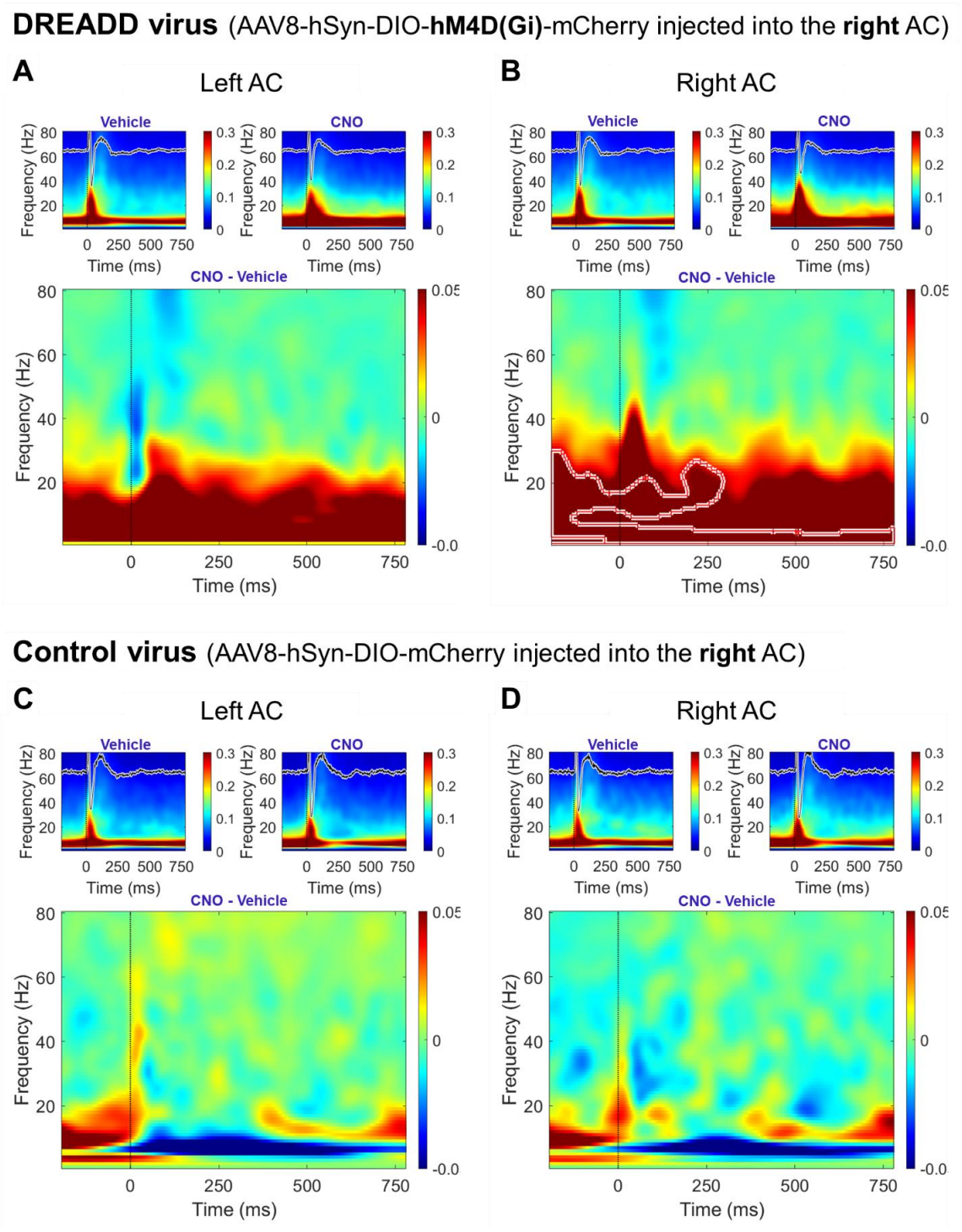

*Figure 2.4. PV+ cell inactivation in the AC results in elevated total power in the theta, alpha, and beta ranges during noise-burst presentation*

The single-trial power (STP) displayed here is a measure of total power (induced and non-induced) present across time in the right (injected) and left (non-injected) AC during noise burst presentation (onset at 0 ms). The top two panels show STP in the CNO (top right panel) and vehicle (top left panel) conditions, with the respective ERP superimposed across time (0 ms marks noise-burst onset). The bottom panel is the subtraction between the conditions (CNO - vehicle). (A) There is no difference between CNO and vehicle in the left AC (non-injected) of the AAV-DREADD group. (B) There is a significant increase in total power in the >0 Hz up to 30 Hz pre- and post-noise onset in the CNO condition compared to vehicle in the right AC (injected) of the AAV-DREADD group. This suggests that inactivation of PV+ cells results in elevated power in the low frequency range in the ipsilateral hemisphere (without impacting the contralateral side). (C) There is no difference between CNO and vehicle in the left (non-injected) or in the (D) right (injected) AC of the AAV-control group. n=14 mice with AAV-DREADD; n=5 mice with AAV-control. Significant clusters were found using Monte-Carlo permutation testing.

*Event-related spectral perturbation (ERSP) to noise burst*

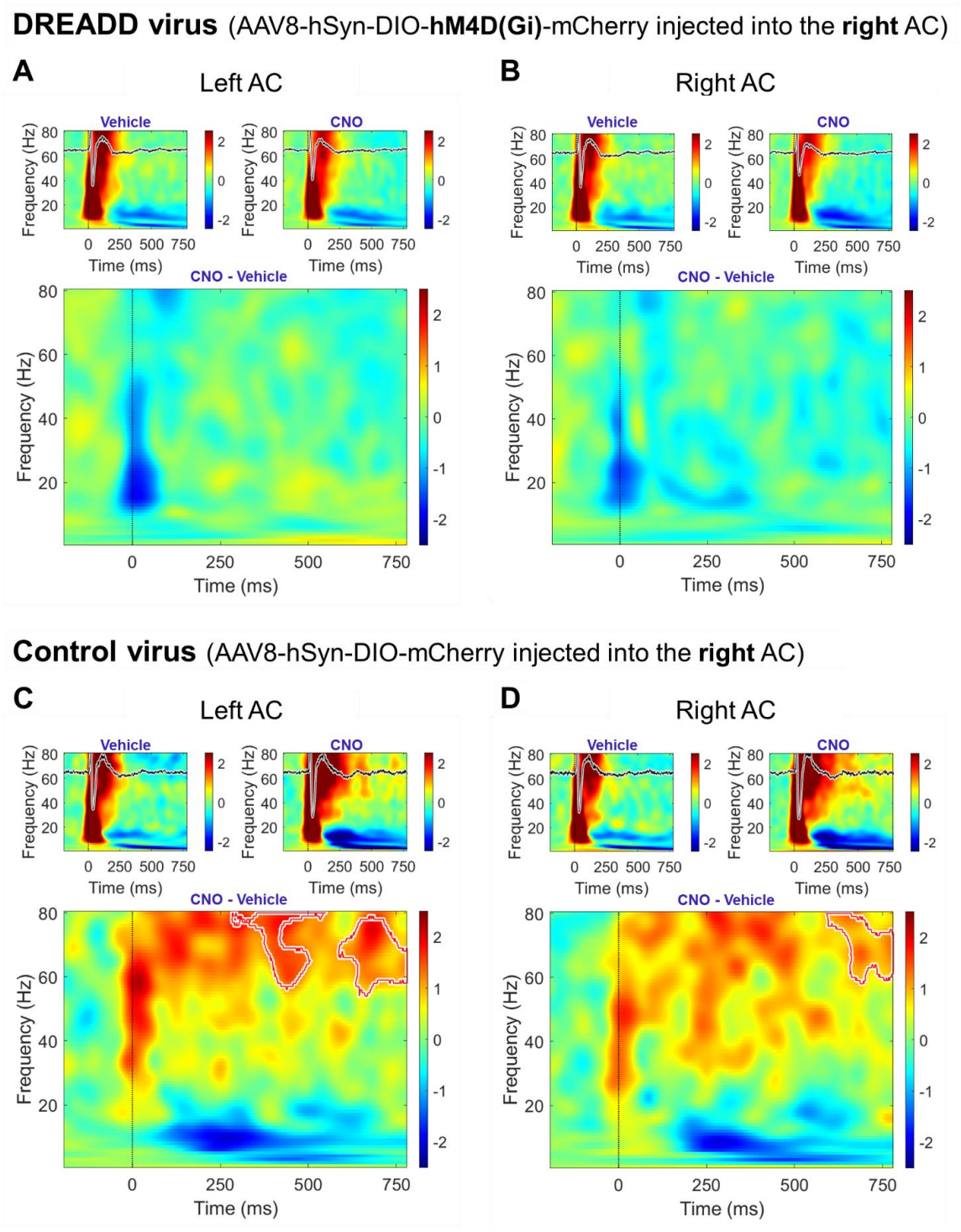

*Figure 2.5. The event-related spectral perturbation (ERSP) in response to noise burst presentations displays no alterations with PV+ cell inactivation in the AC*

The top left panel in A-D displays vehicle condition in each of these groups, the top right panel displays CNO condition, and the bottom large panel is the subtraction between the conditions (CNO - vehicle). The ERSP was calculated by computing the averaged baseline-subtracted noise-burst-induced power (dB) of each frequency at each timepoint across trials, represented by the heatmap. The top two panels display the ERP superimposed across time on each group ERSP. (A) There is no difference in induced power between CNO and vehicle in the left (non-injected) hemisphere of the AC nor in the (B) right (injected) hemisphere. (C) Surprisingly, significant clusters are present in the high gamma range (60-80 Hz) in the ERSP at 500 ms post noise-burst onset in the left (non-injected) and (D) right (injected) AC and at 750 ms post noise-burst onset in the left AC, indicating elevated induced gamma power in the CNO condition compared to vehicle in the AAV-control group, possibly due to effects of CNO alone in the absence of DREADD. n=14 mice with AAV-DREADD; n=5 mice with AAV-control. Significant clusters were found using Monte-Carlo permutation testing.

*Auditory steady state response (ASSR)*

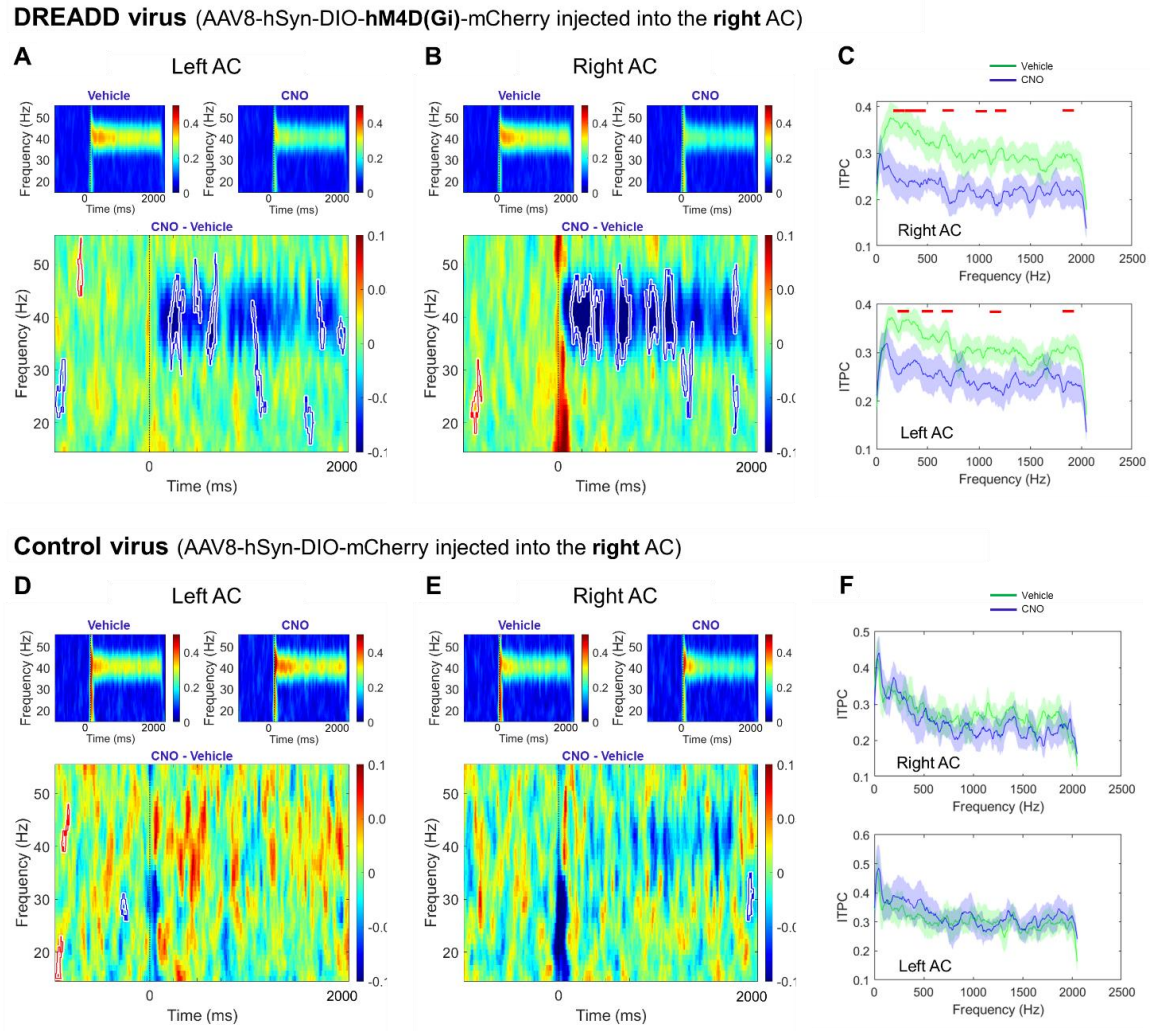

*Figure 2.6. Inactivation of PV+ cells in the right AC reduced phase-locking of the auditory steady state response (ASSR) to click trains presented at 40 Hz in both hemispheres of AC*

The ASSR is spectrotemporally phase-locked to ongoing click trains, and it is useful in measuring phase-locking strength of cortical activity to temporally-modulated sound stimuli. In A, B, D, E, the top panels represent inter-trial phase clustering (ITPC) to the 2-s 40-Hz click train in the CNO (top right panel) and vehicle (top left panel) conditions averaged across 200 trials. The bottom panel represents the difference between conditions (CNO – vehicle). C, F display the ITPC to the 40-Hz click train across the stimulus presentation (onset at 0 ms, offset at 2000 ms) in CNO and vehicle conditions in the right AC (top graph) and left AC (bottom graph). (A) There is reduced ITPC in the left (non-injected) and (B) right (injected) AC in the CNO condition compared to vehicle in the AAV-DREADD group, indicating that PV+ inactivation reduces phase-locking of the ASSR to 40-Hz click train. Significant clusters are outlined and were determined by Monte-Carlo permutation analysis. Visually, the clusters are larger and span longer in the right AC (B; injected hemisphere) vs the left AC (A; non-injected hemisphere). (C) Average ITPC values for each condition are presented, with red lines indicating timepoints of significant differences between the conditions. (D) There is no difference in ITPC values between CNO and vehicle in the left (non-injected) or in the (E) right (injected) AC. (F) Average ITPC values for each condition are presented in the right (top) and left (bottom) AC. n=14 mice with AAV-DREADD; n=5 mice with AAV-control. Significant clusters were found using Monte-Carlo permutation testing.

*Gap ASSR*

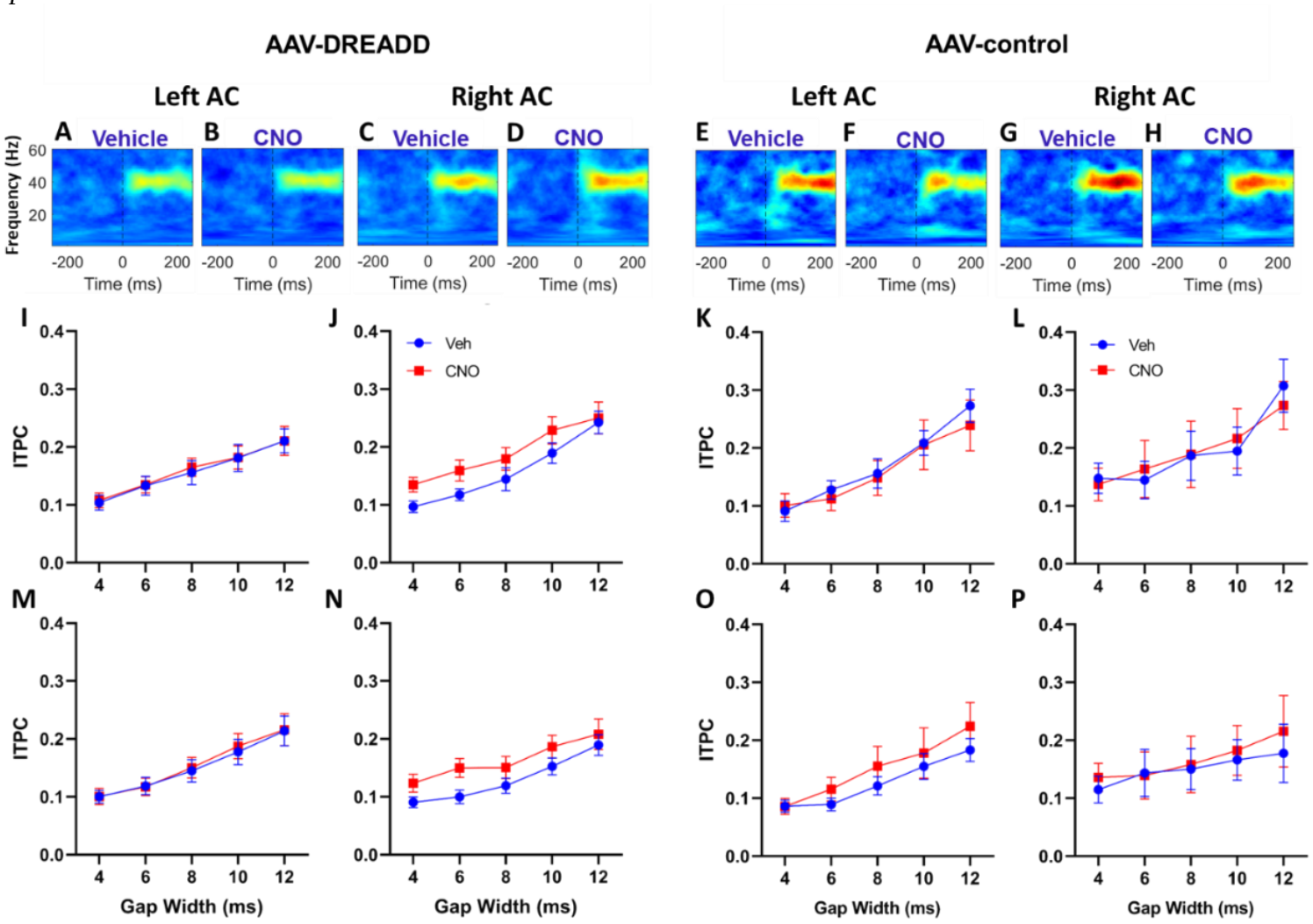
AAV-DREADD
AAV-control
Left AC
Right AC
A Vehicle
B CNO
C Vehicle
D CNO
E Vehicle
F CNO
G Vehicle
H CNO
Frequency (Hz)
60
40
20
-200
0
200
Time (ms)
I
J
K
L
M
N
O
P
ITPC
0.0
0.1
0.2
0.3
0.4
4
6
8
10
12
Gap Width (ms)
Veh
CNO

*Figure 2.7. Phase-locking to gaps-in-noise presented repeatedly at 40 Hz is unaffected by PV+ cell inactivation in the AC*

The heat maps in A-H represent mean ITPC to 12-ms gaps in noise with 100% AM in CNO and vehicle conditions in left and right AC of AAV-DREADD and AAV-control mice. The graphs in I-P represent the average group ITPC for each gap width and modulation depth in CNO and vehicle conditions. (I, J, M, N) There is no significant effect of CNO on ITPC across gap widths for each modulation depth (100% AM, 75% AM) in the AAV-DREADD group or in the (K, L, O, P) AAV-control group. n=14 mice with AAV-DREADD; n=5 mice with AAV-control. CNO effects were analyzed across gap widths using a two-way repeated measures ANOVA for each mouse group and for each modulation depth.

## 2.4 Discussion

The goal of this study was to elucidate the contribution of PV neurons in the AC to the regulation of baseline and sound-related oscillations. To our knowledge, these are the first studies to: (1) identify the contributions of PV neurons in AC to baseline resting EEG power across canonical frequencies and during movement, (2) identify the contribution of cortical PV neurons to amplitude and latency of event related potential (ERP) components, (3) demonstrate that PV neuron activity is necessary for phase-locking the ASSR to ongoing 40-Hz click train, but not to gap-in-noise ASSR, and (4) demonstrate that PV interneurons in the AC regulate ongoing spectral power in beta and lower frequencies. We used DREADD-based inactivation of PV+ neurons in the right AC to accomplish long-term cell manipulation in awake and freely moving mice while recording EEG using epidural screw electrodes to measure auditory responses in the right and left AC. Collectively, these studies investigated well-characterized response properties in the AC that provide fundamental insights on cortical synchrony and dynamics.

### *2.4.1 The role of inhibitory interneurons in synchronizing cortical activity*

The synchronization of neural activity depends largely on inhibitory interneuron activity (Merker, 2013; Buzsaki & Wang, 2012), and PV and SOM neurons in particular play crucial roles in synchronizing cortical activity at various oscillation frequencies (Merker, 2013; Buzsaki & Wang, 2012; Veit et al., 2017; Chen et al., 2017). In the visual cortex (VC) PV neurons play a role in de-synchronization of neural activity, whereas SOM neurons promote the synchronization of neural activity (Chen et al., 2017). In the

AC, PV and SOM facilitate sensory signals and differentially promote the synchronization of cortical auditory responses at low and high frequencies, respectively (Jang et al., 2020; Seay et al., 2020). On this basis of this principle, we expected that inactivating PV+ neurons in the AC would affect the ERP waveform by reducing the amplitudes of the positive and negative deflections as a reflection of reduced synchronization. We found trending increase in P1 amplitude in the left (non-injected) AC and trending reduction in P2/N2 amplitudes in the right (injected) AC, although this phenotype was not statistically robust.

In addition to the evoked positive and negative deflections, the auditory ERP is characterized by long-latency induced components, which are non-phase-locked responses that show a change in power following the ERP (Jeschke et al., 2008; Metherate & Cruikshank, 1999). In young, healthy mice, the long-latency component typically shows an increase in gamma power and a reduction in alpha and beta power compared to baseline. Thalamic stimulation has been shown to generate gamma activity in laminar layer L4 of the AC at a latency of 100-300 ms (Metherate & Cruikshank, 1999). This gamma activity propagated from primary to secondary AC, suggesting intracortical signal propagation within the AC following thalamocortical input. The long-latency gamma power following the initial stimulus-evoked activity in the AC may reflect polysynaptic thalamocortical transmission following the initial direct thalamocortical activation (Metherate & Cruikshank, 1999). It is likely that PV and SOM neurons may regulate the gamma and beta power based on their relationship to these frequency ranges in the visual system (Veit et al., 2017; Chen et al., 2017) and based on

the role of PV and SOM neurons in feedforward thalamocortical suppression (Phillips et al., 2017). However, in the present study we found no effect of PV inactivation on long-latency induced spectral changes in response to sound bursts.

*2.4.2 The contribution of PV+ neurons in baseline rhythmic oscillations in the AC*

Neural oscillations have become an established marker for observing brain states, especially relating to the stages of sleep or epilepsy. Oscillations in the cortex occur during resting, processing sensory information or while attending a task, but the underlying mechanisms producing these oscillations and their implications for behavioral performance remain a major question in the field. Cortical rhythms likely reflect patterns of circuit excitation and inhibition, especially as relates to the temporal regulation of pyramidal cells elicited by local inhibitory interneurons as well as modulatory cortical and subcortical input (Merker, 2013; Buzsaki & Wang, 2012; Barth & MacDonald 1996; Metherate & Cruikshank, 1999; Sukov & Barth, 2001). Whether neural oscillations indicate cognitive processes or simply reflect cortical activation remains an ongoing debate (Merker, 2013; Buzsaki & Wang, 2012). Both resting state and sound evoked cortical oscillations are mediated in part by local interactions between pyramidal cells and GABAergic inhibitory interneurons. In particular, PV neurons are thought to regulate neural oscillations, although their specific contributions remain debated. Chen et al. (2017) showed in the mouse visual system that PV neurons and SOM neurons promote the 20-80 Hz oscillations (broadband gamma range) and 5-30 Hz oscillations (theta to beta range), respectively. Similarly, Cardin et al. (2009) showed that stimulating PV neurons promotes 30-70 Hz power in the local field potential (LFP). Veit el al.

(2017) point to SOM neurons as the key regulators of the narrowband 25-35 Hz (low gamma) in the mouse visual cortex (VC), and they argued that PV neuron activity is instead correlated to the broadband gamma range starting at 40 Hz and extending into the high gamma range towards 100 Hz. The broadband high gamma power (>80 Hz) may be a readout of neuronal spike activity rather than an oscillatory phenomenon (Ray & Maunsell, 2011), suggesting different bands of gamma power stem from different underlying mechanisms. While cortical PV and SOM neurons have been studied in the context of short gap detection (Weible et al., 2014), the impact of these interneurons on auditory cortical oscillations remains largely unknown, although this is a key step to understanding the relationship between circuits and stimulus processing in the central auditory system. Our findings closely reflect the relationship suggested in the literature between PV+ neurons and 40 Hz gamma oscillation in the cortex. Specifically, we found that inactivation of PV+ cells in the right AC reduced phase-locking of the ASSR in the both left and right AC to the 40-Hz click train presentation. Furthermore, in resting EEG we found a reduction in low gamma power and high gamma power in the left (non-injected) and right (injected) hemispheres, respectively.

*2.4.3 Relationship between PV+ neurons and 40 Hz gamma*

The growing literature on the role of PV neurons in cortical oscillations are beginning to suggest that PV neurons may be more directly involved in regulating broadband activity rather than restricting to narrow-band 40 Hz oscillation (Whittington et al., 1995; Buzsaki & Wang, 2012). Specifically, published literature surrounding PV and SOM cell regulation of LFP in the primary VC show SOM cell regulation in the

narrow-band high beta/low gamma range and PV cell regulation of the broadband high gamma range (Chen et al., 2017; Veit el al., 2017). The main difference between these two studies is that Veit et al. (2017) define the range of frequencies close to 30 Hz as "gamma" rather than "beta" because they compare this frequency range in mice to a functionally analogous gamma band in primates. Chen et al. (2017) refer to this band as "beta" but ultimately show similar results to the former: SOM neurons in the VC regulate activity around 30 Hz, while PV neurons regulate a broad range of frequencies. In both studies, PV neurons appear to regulate high gamma more strongly than low gamma centered at ~40 Hz in awake and freely-moving mice. Our findings point to both. The results of this study suggest that at rest, PV+ neurons affect high gamma ipsilaterally and theta/low gamma contralaterally, while impacting 40-Hz steady state response in both hemispheres. Furthermore, we found that inactivation of PV+ neurons in the right AC enhanced ongoing power in beta and lower frequencies in the presence of noise burst stimulation (STP), which parallels the elevated beta power seen in VC with PV+ neuron inactivation (Chen et al., 2017). Overall, our findings provide evidence that in the AC, PV+ neurons facilitate the 40-Hz ASSR, promote baseline high gamma activity, and reduce beta and low frequency power during sound stimulation.

*2.4.4 Movement-related and interhemispheric effects of PV+ cell inactivation on resting EEG*

In addition to the expected changes in the power distribution across different frequency ranges, we predicted movement-related changes to be diminished with PV inactivation. This hypothesis is based on studies that describe motor input to the auditory

cortex that activates PV neurons and lead to motor inhibition of auditory activity (Nelson et al., 2013; Schneider et al., 2014). We found that PV+ cell inactivation in the right AC impacted theta power in the left AC in a movement-dependent manner. Specifically, theta power was increased in CNO conditions compared to vehicle during the "all" and "move" states, but not during the "still" state. This suggests that inactivation of PV+ cells in one hemisphere of the AC can induce changes in cortical oscillatory activity in the opposite hemisphere, alluding to cross-hemispheric connections.

*2.4.5 PV neurons in the cortical circuit*

PV neurons are involved in inhibitory feedforward mechanisms projected to the AC, as in other sensory cortices. The motor cortex sends excitatory projections to PV neurons in the AC, ultimately reducing auditory firing rate (Nelson et al., 2013), presumably while the animal is moving or vocalizing. This strongly suggests motor modulation of central auditory activity. Zhou et al. (2014) showed that locomotion reduces spontaneous and sound-evoked firing rate in laminar layer L2/3 of the mouse AC. This presents a contrast to the visual cortex, in which there is a locomotion-related increase in firing rate in L2/3 of the mouse (Lee et al., 2014; Niell & Stryker, 2010). Despite this difference, both cortices experience increased high-frequency band power (20-80 Hz in AC, 50-70 Hz in VC) and decreased low-frequency band power (1-10 Hz in AC, 10-30 Hz in VC) in the local field potential (LFP) upon stimulus presentation, although the frequency ranges differ between auditory and visual cortices across the studies (Lee et al., 2014; Niell & Stryker, 2010; Zhou et al., 2014). Furthermore, this effect is layer-specific in the AC. Locomotion reduces spontaneous and evoked firing

rate in L2/3 excitatory cells and in PV cells, but L4 spiking rate was unaffected. The study suggested that L1 may play a critical role in inhibiting L2/3 cells during locomotion, as L1 firing rate increased during locomotion, and silencing L1 with tetrodotoxin application increased L2/3 firing rate but did not affect L4 firing rate (Zhou et al., 2014). These findings suggest a different mechanism for motor-mediated inhibition of auditory cortical activity and a different role of PV neurons compared to that suggested by Nelson et al. (2013), in which stimulation of motor cortex activated PV neurons, producing feed-forward inhibition of AC. This difference requires further investigation in future studies.

In future studies, to quantify interhemispheric interactions, phase-phase coupling (PPC) and phase-amplitude coupling (PAC) can be measured between the left and right auditory cortices. PPC assesses whether there is a temporal relationship between the phases of frequency bands across the two hemispheres, which would suggest long-distance coherence between the two hemispheres. PAC assesses whether there is a coupling between the phase of a lower frequency band (e.g., theta) and the amplitude of a higher frequency band (e.g., gamma), which would suggest that power in the gamma range in one hemisphere temporally correlates to activity in the contralateral side. These measures may be performed by filtering the different frequency bands, extracting the phase or power content, and determining the consistency in phase differences between the phase of one frequency band and the phase or power of the other band, which are computed as a phase-locking value (Cohen, 2014; Munia & Aviyente, 2019). The goal

of these analyses would be to quantify the relationship between the activity in the two hemispheres during resting EEG measurements.

## References


Anderson, L.A., Christianson, G.B. and Linden, J.F., 2009. Mouse auditory cortex differs from visual and somatosensory cortices in the laminar distribution of cytochrome oxidase and acetylcholinesterase. *Brain research, 1252*, pp.130-142.

Barth, Daniel S. & MacDonald Kurt D. Thalamic modulation of high-frequency oscillating potentials in auditory cortex. Nature. (1996) 383:78-81.

Bidelman GM, Villafuerte JW, Moreno S, Alain C. Age-related changes in the subcortical-cortical encoding and categorical perception of speech. Neurobiology of Aging (2014) 35:2526-2540.

Brenner CA, Krishnan GP, Vohs JL, Ahn WY, Hetrick WP, Morzorati SL, O'Donnell BF. Steady State Responses: Electrophysiological Assessment of Sensory Function in Schizophrenia. Schizophrenia Bulletin (2009) 35(6):1065–1077.

Brosch M, Budinger E, Scheich H. Stimulus-Related Gamma Oscillations in Primate Auditory Cortex. J Neurophysiol (2002) 87:2715–2725.

Buzsaki, Gyorgy & Wang, Xiao-Jing. Mechanisms of Gamma Oscillations. Annu. Rev. Neurosci. (2012) 35:203–25.

Cardin JA, Carle´ M, Meletis K, Knoblich U, Zhang F, Deisseroth K, Tsai LH, Moore CI. Driving fast-spiking cells induces gamma rhythm and controls sensory responses. Nature (2009) 459:663-668.

Cearley, Cassia N. & Wolfe, John H. Transduction Characteristics of Adeno-associated Virus Vectors Expressing Cap Serotypes 7, 8, 9, and Rh10 in the Mouse Brain. Molecular Therapy (2006) 13(3):528-537.

Chen G, Zhang Y, Li X, Zhao X, Ye Q, Lin Y, Tao HW, Rasch MJ, Zhang X. Distinct Inhibitory Circuits Orchestrate Cortical beta and gamma Band Oscillations. Neuron (2017) 96:1403–1418.

Cohen, Mike X. *Analyzing Neural Time Series Data: Theory and Practice*. Cambridge, The MIT Press 17 Jan 2014.

Davis A, McMahon CM, Pichora-Fuller KM, Russ S, Lin F, Olusanya BO, Chadha S, Tremblay KL. Aging and Hearing Health: The Life-course Approach. Gerontologist (2016) 56(S2): S256–S267.

Del Campo, HN Martin, K. R. Measor, and K. A. Razak. "Parvalbumin immunoreactivity in the auditory cortex of a mouse model of presbycusis." *Hearing research 294*.1-2 (2012): 31-39.

Ethridge LE, White SP, Mosconi MW, Wang J, Pedapati EV, Erickson CA, Byerly MJ, Sweeney JA. Neural synchronization deficits linked to cortical hyper-excitability and auditory hypersensitivity in fragile X syndrome. Mol Autism (2017) 8:22.

Galambos R, Makeig S, Talmachoff PJ. A 40-Hz auditory potential recorded from the human scalp. Proc. Nati. Acad. Sci. USA (1981) 78(4):2643-2647.

Guyon N, Zacharias LR, de Oliveira EF, Kim H, Leite JP, Lopes-Aguiar C, Carlen M. Network Asynchrony Underlying Increased Broadband Gamma Power. J Neurosci (2021) 41(13):2944–2963.

Harris KC, Wilson S, Eckert MA, Dubno JR. Human evoked cortical activity to silent gaps in noise: effects of age, attention, and cortical processing speed. Ear and Hearing (2012) 33(3), 330–339.

Herdman AT, Lins O, Van Roon P, Stapells DR, Scherg M, Picton TW. Intracerebral Sources of Human Auditory Steady-State Responses. Brain Topography (2002) 15(2):69-86.

Jang HJ, Chung H, Rowland JM, Richards BA, Kohl MM, Kwag J. Distinct roles of parvalbumin and somatostatin interneurons in gating the synchronization of spike times in the neocortex. Science advances. 2020 Apr 22;6(17):eaay5333.

Jeschke M, Lenz D, Budinger E, Herrmann CS, Ohl FW. Gamma oscillations in gerbil auditory cortex during a target-discrimination task reflect matches with short-term memory. Brain Research (2008) 1220:70–80.

Kato HK, Asinof SK, Isaacson JS. Network-level control of frequency tuning in auditory cortex. Neuron. 2017 Jul 19;95(2):412-23.

Keller AJ, Houlton R, Kampa BM, Lesica NA, Mrsic-Flogel TD, Keller GB, Helmchen F. Stimulus relevance modulates contrast adaptation in visual cortex. eLife (2017) 6:e21589.

Lee AM, Hoy JL, Bonci A, Wilbrecht L, Stryker MP, Niell CM. Identification of a Brainstem Circuit Regulating Visual Cortical State in Parallel with Locomotion. Neuron (2014) 83:455–466.

Lovelace JW, Ethell IM, Binder DK, Razak KA. Translation-relevant EEG phenotypes in a mouse model of Fragile X Syndrome. Neurobiol Dis. (2018) 115:39–48.

Merker, Bjorn. Cortical gamma oscillations: the functional key is activation, not cognition. Neuroscience and Biobehavioral Reviews. (2013) 37:401-417.

Metherate, Raju & Cruikshank, Scott J. Thalamocortical inputs trigger a propagating envelope of gamma-band activity in auditory cortex in vitro. Exp Brain Res (1999) 126:160–174.

Modi, Meera E & Sahin, Mustafa. Translational use of event-related potentials to assess circuit integrity in ASD. Nat Rev Neurol (2017) 13(3):160-170.

Munia, Tamanna TK & Aviyente, Selin. Time-Frequency Based Phase Amplitude Coupling Measure For Neuronal Oscillations. Scientific Reports (2019) 9:12441.

Natan RG, Rao W, Geffen MN. Cortical Interneurons Differentially Shape Frequency Tuning following Adaptation. Cell Reports (2017) 21:878–890.

Nelson A, Schneider DM, Takatoh J, Sakurai K, Wang F, Mooney R. A Circuit for Motor Cortical Modulation of Auditory Cortical Activity. J Neurosci (2013) 33(36):14342–14353.

Nguyen AO, Binder DK, Ethell IM, Razak KA. Abnormal development of auditory responses in the inferior colliculus of a mouse model of Fragile X Syndrome. J Neurophysiol (2020) 123(6):2101-2121.

Niell, Cristopher M & Stryker, Michael P. Modulation of Visual Responses by Behavioral State in Mouse Visual Cortex. Neuron (2010) 65:472–479.

Phillips EAK, Schreiner CE, Hasenstaub AR. Cortical Interneurons Differentially Regulate the Effects of Acoustic Context. Cell Reports (2017) 20:771–778.

Picton TW, Skinner CR, Champagne SC, Kellett AJC, Maiste AC. Potentials evoked by the sinusoidal modulation of the amplitude or frequency of a tone. The Journal of the Acoustical Society of America (1987) 82:165-178.

Ray, Supratim & Maunsell, John HR. Different Origins of Gamma Rhythm and High-Gamma Activity in Macaque Visual Cortex. PLoS Biology (2011) 9(4):e1000610.

Rock, Crystal & Apicella, Alfonso junior. Callosal Projections Drive Neuronal-Specific Responses in the Mouse Auditory Cortex. J Neurosci (2015) 35(17):6703– 6713.

Ross B, Draganova R, Picton TW, Pantev C. Frequency specificity of 40-Hz auditory steady-state responses. Hearing Research (2003) 186:57-68.

Ross B, Schneider B, Snyder JS, Alain C. Biological Markers of Auditory Gap Detection in Young, Middle-Aged, and Older Adults. PLoS ONE (2010) 5(4):e10101.

Roth, Bryan L. DREADDs for Neuroscientists. Neuron (2016) 89(4): 683–694.

Rotschafer, Sarah & Razak, Khaleel. Altered auditory processing in a mouse model of fragile X syndrome. Brain Res (2013) 1506:12-24.

Rumschlag JA, Lovelace JW, Razak KA. Age- and movement-related modulation of cortical oscillations in a mouse model of presbycusis. Hearing Research (2021) 402:108095

Rumschlag, J.A. and Razak, K.A., 2021. Age-related changes in event related potentials, steady state responses and temporal processing in the auditory cortex of mice with severe or mild hearing loss. *Hearing Research*, *412*, p.108380.

Schneider DM, Nelson A, Mooney R. A synaptic and circuit basis for corollary discharge in the auditory cortex. Nature (2014) 513(7517):189–194.

Seay MJ, Natan RG, Geffen MN, Buonomano DV. Differential short-term plasticity of PV and SST neurons accounts for adaptation and facilitation of cortical neurons to auditory tones. Journal of Neuroscience. 2020 Nov 25;40(48):9224-35.

Setti A, Finnigan S, Sobolewski R, McLaren L, Robertson IH, Reilly RB, Kenny RA, Newell FN. Audiovisual temporal discrimination is less efficient with aging: an event-related potential study. Neuroreport (2011) 22(11):554-8.

Seymour, R.A., Rippon, G., Gooding-Williams, G., Sowman, P.F. and Kessler, K., 2020. Reduced auditory steady state responses in autism spectrum disorder. *Molecular autism*, *11*, pp.1-13.

Stoica L, Ahmed SS, Gao G, Esteves MS. AAV-mediated gene transfer to the mouse CNS. Curr Protoc Microbiol. (2013) 0 14: Unit14D.5.

Sukov, William & Barth, Daniel S. Cellular Mechanisms of Thalamically Evoked Gamma Oscillations in Auditory Cortex. J Neurophysiol (2001) 85(3):1235-45.

Thompson KJ, Khajehali E, Bradley SJ, Navarrete JS, Huang XP, Slocum S, Jin J, Liu J, Xiong Y, Olsen RHJ, Diberto JF, Boyt KM, Pina MM, Pati D, Molloy C, Bundgaard C, Sexton PM, Kash TL, Krashes MJ, Christopoulos A, Roth BL, Tobin AB. DREADD Agonist 21 Is an Effective Agonist for Muscarinic-Based DREADDs in Vitro and in Vivo. ACS Pharmacol. Transl. Sci. (2018) 1(1):61–72.

Thuné, H., Recasens, M. and Uhlhaas, P.J., 2016. The 40-Hz auditory steady-state response in patients with schizophrenia: a meta-analysis. *JAMA psychiatry*, *73*(11), pp.1145-1153.

Toso, A., Wermuth, A.P., Arazi, A., Braun, A., Grent, T., Uhlhaas, P.J. and Donner, T.H., 2024. 40 Hz Steady-State Response in Human Auditory Cortex Is Shaped by GABAergic Neuronal Inhibition. *Journal of Neuroscience*.

Trujillo, M. & Razak, KA. Altered cortical spectrotemporal processing with age-related hearing loss. J Neurophysiol (2013) 110(12):2873-2886.

Veit J, Hakim R, Jadi MP, Sejnowski TJ, Adesnik H. Cortical gamma band synchronization through somatostatin interneurons. Nature Neurosci (2017) 20:951-959.

Wang X, Lu T, Snider RK, Liang L. Sustained firing in auditory cortex evoked by preferred stimuli. Nature (2005) 435:341-346.

Weible AP, Moore AK, Liu C, DeBlander L, Wu H, Kentros C, Wehr M. Perceptual Gap Detection Is Mediated by Gap Termination Responses in Auditory Cortex. Current Biology (2014) 24(13):1447–1455.

Wen TH, Lovelace JW, Ethell IM, Binder DK, Razak KA. Developmental changes in EEG phenotypes in a mouse model of Fragile X Syndrome. Neuroscience (2019) 398:126–143.

Whittington MA, Traub RD, Jefferys JGR. Synchronized oscillations in interneuron networks driven by metabotropic glutamate receptor activation. Nature (1995) 373:612-615.

Winkler I, Denhamb S, Escerac C. Auditory Event-related Potentials. Encyclopedia of Computational Neuroscience. (2013) Springer, New York, NY.

Zhang B, Jia Y, Wang C, Shao X, Wang W. Visual event-related potentials in external emotional conditions in bipolar disorders I and II. Neurophysiologie Clinique (2019) 49(5):359-369.

Zhou M, Liang F, Xiong XR, Li L, Li H, Xiao Z, Tao HW, Zhang LI. Scaling down of balanced excitation and inhibition by active behavioral states in auditory cortex. Nature Neurosci (2014) 17(6):841–850.

# Chapter 3: Loss of FMRP in the Mouse Midbrain Causes Temporal Processing Deficits, but not Abnormal Power, in Cortical Response

**Abstract**

Autism spectrum is associated with sensory processing deficits in the brain, including cortical hyperexcitability and abnormal temporal processing, but their underlying mechanisms are unclear. These sensory deficits are present in Fragile X Syndrome (FXS), a leading monogenetic cause of developmental intellectual disability that results from the loss of Fragile X messenger ribonucleoprotein 1 (*Fmr1*) expression, which prevents the expression of *Fmr* protein (FMRP). In the mouse model of FXS, electroencephalogram (EEG) recordings of auditory (AC) and frontal cortex (FC) reveal elevated resting gamma band power, enhanced single trial power (STP) during acoustic stimulation (particularly in the gamma range), increased amplitudes of auditory event-related potentials (ERP), reduced phase-locking to temporally-modulated sounds, and hyperactive behavior in the open field (OF). We previously showed that deletion of *Fmr1* in the forebrain alone reproduces the auditory evoked-power deficits and hyperactive behavior but does not reveal phase-locking deficits. This suggests that removal of FMRP in the forebrain does not impact temporal processing. To identify whether the midbrain is important for this function, in the present study we recorded AC and FC EEG activity in mice with Cre-dependent midbrain deletion, via the *Ntsr1* promoter, of *Fmr1*. Resting EEG recordings were analyzed for distribution of spectral power, and noise train-evoked responses were analyzed for STP. In addition, to examine temporal processing, we recorded gap-in-noise auditory steady state responses (gap-ASSR) to a 40 Hz-modulated stimulus. We found that midbrain deletion of *Fmr1* did not impact resting EEG power, ERP, or STP, but it reduced phase-locking to gap-ASSR

stimuli in the AC, suggesting deficits in auditory temporal processing. There were no changes in expression of perineuronal nets (PNN) in the midbrain, nor was behavioral hyperactivity seen in the OF. These findings, together with our prior forebrain-specific deletion studies, point to differential roles of forebrain and midbrain FMRP in regulating auditory function in the brain and hyperactivity behavior. Our results suggest different origins of deficits in resting or evoked power compared to deficits in temporal processing of sound signals, which need to be considered in therapeutic approaches to FXS and autism.

## 3.1 Introduction

Autism spectrum (ASD) is often comorbid with delays in language and speech function. Auditory hyper- or hypo-sensitivity and variability in neural temporal responses during development are likely important underlying factors (Anderson et al., 2010a; 2010b). Fragile X Syndrome (FXS) is a leading monogenetic cause of developmental intellectual disability that is characterized by sensory hypersensitivity and ASD-like behaviors. FXS affects 1 in 4,000 males and 1 in 8,000 females, causing symptoms that include deficits in learning, speech and language, anxiety and hyperactive behavior, and sensory hypersensitivity. FXS is caused by a mutated Fragile X messenger ribonucleoprotein 1 gene (*Fmr1*), an X-linked gene that is preceded by repeats of CGG trinucleotide segments. The neurotypical number of CGG repeats is between 6 and 50 copies. An extensive number of copies of the CGG segment (>200 copies) is present in individuals with FXS, preventing expression of Fragile X messenger ribonucleoprotein (FMRP). FMRP is an mRNA-binding protein localized in synaptic terminals which regulates translation of various genes in the brain and other tissues. With the loss of FMRP, there is impaired synapse development, altered excitatory/inhibitory synaptic balance, and an increase in neuronal activity, including in the sensory cortex.

Individuals with FXS display debilitating auditory hypersensitivity and cortical hyperexcitability. Abnormal auditory processing has been quantified in both humans with FXS and in the *Fmr1* KO mouse model using resting and sound evoked EEG recordings (reviewed in Razak et al., 2021). Adolescents and adults with FXS show impaired

habituation and elevated amplitudes of cortical event-related potentials (ERP) in response to repeated noise bursts compared to typically-developing adults (Castren et al., 2003; Van der Molen et al., 2012; Rotschafer & Razak, 2014; Rais et al., 2018; Ethridge et al., 2016; 2019). Phase-locking to amplitude-modulated stimuli is reduced in FXS. Both in resting EEG and in single trial background power during acoustic stimulation, there is a significant enhancement of gamma band power in FXS, implicating abnormally high ongoing power in the cortex. These EEG differences are correlated with clinical measures in humans with FXS. Remarkably similar physiological responses associated with abnormal auditory processing are seen in the global *Fmr1* KO mouse in which FMRP is removed embryonically from all brain regions (and other tissues). This includes reduced phase-locking to chirp stimuli, increased ERP amplitude, reduced ERP habituation, increased gamma resting power, and increased gamma band STP during acoustic stimulation (Lovelace et al., 2018). In addition, global FMRP deletion results in hyperactivity behaviors in the open-field (OF) paradigm in the mouse. Hyperactivity is also seen in humans with FXS. These similarities in phenotype increase the translational relevance of the *Fmr1* KO animal model to understand pathophysiological mechanisms involved in FXS.

The similarity in objective physiological underpinnings of auditory hypersensitivity and temporal processing deficits in FXS and *Fmr1* KO mice provides an opportunity to examine systems and circuit level mechanisms of sensory dysfunction in a model for ASD. FMRP is expressed across the auditory pathway from the cochlear nucleus to the cortex, but it remains unclear how cortical and subcortical brain regions

along the auditory pathway contribute to the electrophysiological and behavioral phenotypes of FXS. Previously, we showed that forebrain deletion of FMRP using *Nex*-Cre (Lovelace et al., 2020) or *CamKII*-Cre (Rais et al., 2022) reproduced the elevated spectral gamma power, the increased auditory ERP amplitudes, and hyperactivity behaviors, which are seen in the global *Fmr1* KO model (Lovelace et al., 2018). However, in the forebrain-specific deletion models, phase-locking to amplitude-modulated sounds was unaltered, suggesting that temporal processing relies on subcortical structures. To test whether cortically recorded temporal processing abnormalities may be inherited from the loss of FMRP in subcortical sites, we examined how midbrain deletion of FMRP using the *Ntsr1* promoter in mice impacts resting EEG, evoked auditory responses, and phase-locking of the AC and FC to temporally-modulated sounds. In addition, we tested if abnormal FMRP expression in the midbrain causes hyperactivity behaviors in the OF.

Loss of FMRP globally, and in forebrain-specific models, results in elevated matrix metalloproteinase-9 (MMP-9) levels in the brain. There is also elevated MMP-9 in the midbrain inferior colliculus (IC) in global *Fmr1* KO mice (Kokash et al., 2019). Abnormally high MMP-9 may result in loss of perineuronal nets (PNN) surrounding inhibitory interneurons in the cortex, resulting in disrupted inhibition in cortical circuits (Sidhu et al., 2014; Gkogkas et al., 2014; Wen et al., 2018). Therefore, we examined PNN expression in the AC and IC of the midbrain deletion model.

We predict that midbrain deletion of *Fmr1* is sufficient to reduce phase-locking to amplitude-modulated sounds but does not result in elevated non-phase-locked power.

We tested this prediction by measuring ITPC in a mouse model with *Ntsr1*-mediated deletion of FMRP when presented with amplitude modulation of ongoing noise. We also assessed if FXS biomarkers in resting EEG and auditory ERP are present with midbrain deletion of *Fmr1*, namely elevated gamma power and N1 amplitude. If a double-dissociation is present between forebrain and midbrain contributions to the aforementioned EEG biomarkers of FXS, then we expect resting EEG and ERP in the mouse model with *Ntsr1*-mediated deletion of FMRP to appear similar to wild-type (WT), as these markers were affected by forebrain deletion of FMRP.

## 3.2 Materials and Methods

### *3.2.1 Mice*

Male mice with midbrain deletion of FMRP were obtained by breeding $Ntsr1^{-/Cre}$ and $Fmr1^{flox/flox}$ C57/Bl6J mice. Control littermate mice expressed the *Fmr1*-flox allele but not *Ntsr1*-Cre. Global *Fmr1* KO male mice were obtained by breeding WT male $Fmr1^{x/-}$ with heterozygous female $Fmr1^{x/-}$ which generated *Fmr1* KO and control (*Fmr1*-expressing) littermates. Pups were weaned at P21 and group-housed until surgery. The present study used n=16 C57/Bl6J male mice of the *Ntsr1*-Cre x *Fmr1*-flox line and n=10 *Fmr1* KO along with their respective control littermates (n=12 $Fmr1^{flox}$ and n=8 *Fmr1* WT littermates) at postnatal ages P60-P100. Mice were maintained in an AAALAC accredited facility in 12 h light/dark cycles and fed standard mouse chow. Food and water were provided *ad libitum*. All mice were genotyped (Transnetyx, TN) using standard tail snip procedures. All procedures were done according to the National Institute of Health (NIH) and Institutional Animal Care and Use Committee guidelines.

*3.2.2 EEG surgeries*

The EEG screw electrode implantation surgical methods described here were previously published (Lovelace et al., 2018; Rumschlag & Razak, 2021). Mice were anesthetized for the duration of the surgery through intraperitoneal (i.p.) injections of 120 μg/g of ketamine and 5 μg/g of xylazine. The anesthetic state of mice was monitored through the toe-pinch reflex tested every 10-15 minutes. Surgery commenced only when the mouse did not react (withdrawal reflex) to this procedure. Half-dose supplements of ketamine were further administered if required. Each mouse was placed into a standard rodent stereotactic frame. Body temperature was monitored and maintained around 37° C using a rectal thermometer linked to a temperature controller system connected to a heating pad (FHC Inc., ME). An ophthalmic ointment was administered to keep eyes moist throughout the procedure. Nair hair remover was applied on the head to remove hair and the skin was sterilized using alcohol wipes and gentle application of betadine. An incision was made in the skin for skull exposure. 0.9% saline was applied to the skull intermittently to clean the skull and maintain moisture. Three 1mm-diameter holes were drilled through the skull, exposing the right AC (-2.2mm caudal, +4.8mm lateral to bregma), the right FC (+3.0 mm rostral, +1.6 mm lateral to bregma) and the left occipital lobe (−4.8 mm caudal, −2.95 mm lateral). Epidural screw electrodes connected to a three-channel headpost were implanted in the right AC and FC for EEG recording and in the occipital lobe for reference.

Antibiotic ointment was applied around the incision site. Dental cement was applied onto the exposed skull and around the incision site, sealing the surgical site

completely. Body temperature was further monitored until mice showed signs of waking. Before surgery, mice were administered with long-acting buprenorphine (Ethiqa), a potent analgesic (0.1 mg/kg body weight), subcutaneously. The analgesic effects are present during and following surgery for 48 hrs. Mice were placed, singly housed, in a new cage on top of a heat pad until fully awake and moving around. They were closely monitored for 48 hours and were allowed 4-5 days of recovery before EEG recordings.

*EEG Recording and Stimuli*. The EEG recording and analysis methods described here were previously published (Lovelace et al., 2018; Rumschlag & Razak, 2021). Awake and freely moving mice were placed in a plastic arena covered with bedding and surrounded by a wire mesh Faraday cage on a metal table inside a sound-insulated booth (Gretch-Ken Industries, OR). Mice were attached to an EEG cable via a freely rotating commuter tethered to the implanted headpost for recording. The cable was connected to a Tucker-Davis Technologies (TDT) RA4LI/PA head stage/preamplifier, which was connected via optic fiber to a TDT RZ6 I/O device. A TDT MF1 speaker placed 20 cm above the arena was connected to the RZ6 and played stimuli designed on OpenEx at a sampling rate of 24.414 kHz. Sound levels were calibrated using a ¼" Bruel and Kjaer (Nærum, Denmark) microphone. There were two recording channels (AC and FC) and a ground/reference channel (OC). TTL pulses marking stimulus onsets were recorded on a separate channel.

### *3.2.3 Resting EEG*

Resting EEG is defined as EEG recordings obtained in the absence of auditory stimulation. Following 10 minutes of habituation in the arena, resting EEG was recorded

for 5 minutes. Resting EEG was recorded because abnormal power spectrum distribution is a robust and replicable finding in humans with FXS and in global *Fmr1* KO mouse.

*Auditory Event-Related Potentials (ERP).* Following resting EEG, 120 presentations of 1-12 kHz narrow-band noise bursts (100 ms duration) were played at 70 dB SPL at a repetition rate of 0.25 Hz and a rise/fall rate of 5 ms to record auditory ERPs.

### *3.2.4 Auditory steady state response (ASSR)*

ASSR was recorded using an amplitude-modulated sound signal consisting of clicks presented at a rate of 40 Hz at 70 dB SPL. Each click train lasted 1 sec in duration. There were 200 repetitions of the click train. The 40 Hz ASSR has been used to study auditory temporal processing and is suggested as a biomarker in neurodevelopmental disorders such as schizophrenia (Thune et al., 2016) and autism spectrum disorders (Seymour et al., 2020). Global *Fmr1* KO mice show reduced phase locking fidelity to this stimulus.

### *3.2.5 Gap-in-noise ASSR*

The 40 Hz gap-in-noise ASSR (henceforth, ‘gap ASSR’) stimulus uses gaps in continuous noise to elicit an ASSR. The stimuli consisted of 75 dB continuous noise periodically interrupted by 10 gaps placed 25 ms apart from onset to onset (for a presentation frequency of 40 Hz). A single stimulus began with 250 ms of noise, followed by 250 ms of gap-interrupted noise, followed by continuous noise, and so on, for a total of 10 presentations of the gap-interrupted noise. The stimulus ended with 250 ms of continuous noise, followed by a silent ISI of 500 ms. For each 250 ms segment, the

gap width and modulation depth were randomly selected from a parameter space, consisting of 2-12 ms gaps (2 ms intervals) and modulation depths of 100%, 75%, and 50%, for a total of 18 possible combinations of gap width and modulation depth. Each stimulus was presented at least 75 times over the 30-minute presentation period. Gap-in-noise stimuli are commonly used to study auditory temporal processing acuity in humans and animals (Weible et al., 2014; Harris et al., 2012).

### *3.2.6 EEG Data Analysis*

Motion detection was achieved using a 27 mm piezoelectric pressure sensor (AW-PZT27L; Audiowell; Guangdong, China) placed beneath the arena. An infrared video camera was mounted above the arena to record mouse movements as the EEG recordings were made in the dark. OpenEx (TDT) was used along with the RZ6 to record EEG signals, record pressure signals, operate the LED light used to synchronize the video and waveform data, produce and store digital pulses, and to produce auditory stimuli. The EEG signals were captured at a sampling rate of 24.414 kHz and down-sampled to 1024 Hz. To correlate EEG power with movement, piezoelectric signals recorded during EEG recordings were analyzed for motion using a custom MATLAB script.

The EEG signal was transformed using a complex Morlet wavelet transform, with a constant wavelet parameter of 7, to provide instantaneous spectral power at frequencies ranging from 1–250 Hz.

### *3.2.7 Resting EEG analysis*

The goal of resting EEG is to identify how power spectral density changes due to FMRP deletion in the midbrain, especially in comparison to forebrain deletion (Lovelace et al., 2020; Rais et al., 2022) and global *Fmr1* KO (Lovelace et al., 2018). Resting EEG data was analyzed by applying the fast Fourier transform on the EEG trace in the time-domain. Frequency ranges were binned according to canonical frequency ranges: Delta, 1-3 Hz; Theta, 4-7 Hz; Alpha, 8–13 Hz; Beta, 14-30 Hz; Low Gamma, 30-59 Hz; High Gamma, 60-100 Hz. The average power of each frequency bin across the 5-minute recording was calculated for each subject. A two-way analysis of variance (ANOVA) with Bonferroni's correction for multiple comparisons was used to analyze main effects of genotype across frequency bins.

### *3.2.8 ERP analysis*

We previously published the analysis methods of ERP, ASSR, and gap ASSR and identical methods were used here (Rumschlag & Razak, 2021). Briefly, the ERP is the average of all recorded responses in the time-domain aligned to the stimulus onset. ERP waveform provides insight into synchronized population activity resulting in distinct peaks (namely P1, N1 and P2) at specific latencies following sound onset. Single trial power (STP) was obtained by using the Morlet wavelet transform and subtracting out sound-evoked changes in spectral power from baseline. Significant clusters were found using Monte-Carlo nonparametric permutations testing; a total of 2000 permutations were applied (Cohen, 2014; Rumschlag & Razak, 2021).

### *3.2.9 ASSR and gap ASSR analysis*

ASSR and gap ASSR responses underwent Morlet wavelet transformation. ASSR facilitates a measurement of how well cortical generators synchronize to rapid temporal modulations in the signal. Inter-trial phase clustering (ITPC) is a value that reflects the fidelity of phase-locking to the temporal modulations across trials. ITPC was measured as a vector whose length represents the distribution of phase-locking values to an oscillating frequency across all stimulus presentations. ITPC was calculated for ASSR in response to clicks presented at a 40-Hz rate and was calculated for each combination of gap width and modulation depth. ITPC values are between 0 and 1; higher ITPC values indicate more consistent phase angles in EEG response to ASSR stimulus across trials. A two-way ANOVA was used to examine main effects and interaction of genotype, gap width, and modulation depth.

### *3.2.10 PNN Staining*

All steps were performed at room temperature unless stated otherwise. Mice were injected with a lethal dosage of sodium pentobarbital and then transcardially perfused using a peristaltic pump (Harvard Apparatus, MA, USA) with 0.1 M phosphate buffer saline (PBS) followed by 4% paraformaldehyde (PFA, pH 7.4). Brains were immediately removed and post-fixed in 4% PFA for 2 h at 4°C. Following post-fixation, brains were placed in a 30% sucrose solution until they sank (~36–48 h at 4°C) and then sectioned into 40 μm slices on a cryostat (CM1860, Leica, IL, UK) and stored in a 0.1 M PBS solution containing 0.1% sodium azide.

For each animal, 2-3 slices containing AC and inferior colliculus (IC) were taken and processed for PNN staining. Approximately the same rostral-caudal range of slices was used for each animal. Staining was performed on free-floating sections with agitation at room temperature. Sections were rinsed for 5 min with 0.1 M PBS solution three times and then treated with 50 mM ammonium chloride for 15 min, followed by three rinses in 0.1 M PBS for 5 min each. Sections were incubated for three hours in a 1:500 dilution of fluorescein-tagged Wisteria floribunda Lectin (4μg/mL WFA, Vector Laboratories Cat# FL-1351, RRID: AB_2336875). Finally, sections were washed three times with 0.1 M PBS for 5 min and mounted onto glass slides. Vectashield with a DAPI nuclei stain (Vector Labs, Burlingame, CA, USA, F2-135) was used as the mounting medium. Slides were cover-slipped and sealed prior to imaging on a Zeiss 880 Inverted confocal microscope (10x objective). Microscope settings were consistent across all images for intensity comparisons.

Imaged Z-stacks were selected from each slice and 3-D projections of similar sizes were created using ImageJ. A box of 400μm width and spanning from pia to white matter was used to analyze AC. A box of 400μm by 400μm was used to analyze central IC (ICc), which was further subdivided into “upper” and “lower” IC. We used PIPSQUEAK, a standardized detection program, for analyzing cell counts with PNN (Slaker et al. 2016; https://ai.RewireNeuro.com). PIPSQUEAK was run in “semi-automatic mode” to select ROIs identifying PNNs, which were then verified by a trained experimenter who was blinded to the experimental conditions. T-tests were used to

compare cell counts between genotypes for each region. It is important to note that PNN staining in this study is limited to WFA+ PNNs.

*3.2.11 Behavior*

Mice were tested at ages between postnatal ages P60 and P90 in the open field and elevated plus maze tests. Mice tested for behavior had no other procedure performed prior to the open field test.

*3.2.12 Open Field Test*

The OF arena was 50 × 50-cm with 38-cm-high walls. The OF arena was placed in a brightly lit room with two lamps providing extra illumination on the arena, and one mouse at a time was placed in a corner of the open field and allowed to explore for 10 min while being recorded with digital video camera from above, and only the first 5 minutes of behavior were analyzed. The floor was cleaned with 70% ethanol, 3% acetic acid, and then Millipore filtered water between tests to eliminate odor trails. Mice were tested between the hours of 1400 and 1800, and this test was always performed prior to the elevated plus maze. The arena was subdivided into a 4 × 4 grid of squares with the middle of the grid defined as the center. The percent time spent in thigmotaxis, the center, and the rest of the arena was quantified as a measure of exploratory behavior, and total distance was used to quantify hyperactivity. A line 4 cm from each wall was added to measure thigmotaxis. A bout was defined as one entrance and one exit from a section of the arena (thigmotaxis, center, rest of arena). Activity was scored using TopScan Lite

software (Clever Sys., Inc., Reston). Statistical analysis was performed with Wilcoxon rank sum test, and data represent median and interquartile ranges.

*3.2.13 Elevated Plus Maze*

After the OF, mice were placed in the elevated plus maze (EPM). The EPM consisted of 4 arms in a plus configuration. The EPM was placed in a brightly lit room with a lamp providing extra illumination on the maze. Two opposing arms had 15-cm tall walls (closed arms), and two arms were without walls (open arms). The entire maze sat on a stand 39 cm above the table it was placed on. Each arm measured 30 cm long and 5 cm wide. Mice were allowed to explore the maze for 10 min while being recorded by digital video camera from above, and only the first 5 minutes of behavior were analyzed. The maze was wiped with 70% ethanol, 3% acetic acid, and then Millipore filtered water between each test to eliminate odor trails. Time spent in closed arms was used as a measure of anxiety, and total distance traveled and number of bouts were used to assess hyperactivity. A bout was defined as one entrance and one exit from a section of the arena (closed arms and open arms + center). Statistical analysis was performed with Wilcoxon rank sum test, and data represent median and interquartile ranges.

**3.3 Results**

The main goals of this study were to quantify EEG and behavioral responses in the $Cre^{Ntsr1}/Fmr1^{Flox/y}$ cKO mice in which FMRP is removed from midbrain auditory region excitatory neurons and is not affected in AC, FC, and auditory thalamus. The $Fmr1^{Flox/y}$ control mice were recorded for comparison. Additionally, we also recorded EEG from global *Fmr1* KO mice and their littermate WT controls. The reason for the

latter comparison is that the gap-ASSR paradigm we used in this study for the cKO mice on the C57bl6/J background has not been tested previously in adult littermate mice.

*3.3.1 Midbrain deletion of Fmr1 does not change resting cortical power spectral density*

Five minutes of resting EEG data (in the absence of auditory stimulation) from electrodes implanted in the AC and FC of *Fmr1* KO (n=10), WT (n=8), $Fmr1^{Flox/y}$ (n = 12) and $Cre^{Ntsr1}/Fmr1^{Flox/y}$ cKO mice (n = 16) was recorded. Spectral power density ($\mu V^2/Hz$) was calculated for each 1-s segment of the EEG trace using fast Fourier transform, followed by averaging all segments for a given mouse in the AC and FC. These individual averages then contributed to the grand average for each genotype. Power spectral density was compared for canonical frequency bands (Theta, 4-7 Hz; Alpha, 8–13 Hz; Beta, 14-30 Hz; Low Gamma, 30-59 Hz; High Gamma, 60-100 Hz). Multiple Mann-Whitney analysis was used with Bonferroni correction for multiple comparisons, resulting in $\alpha = .0083$ to account for six frequency bands. Global *Fmr1* KO mice showed elevated resting gamma band power elevation compared to WT mice as reported in previous studies in both AC (Figure 1A: low gamma, *p = .0033; high gamma, ***p < .0001) and FC (Figure 1B: low gamma, *p = .0079; high gamma, ***p < .0001). However, when $Fmr1^{Flox/y}$ and $Cre^{Ntsr1}/Fmr1^{Flox/y}$ cKO mice were compared, no differences were seen in any band in either cortical region (Figure 1C, D). These data indicate that abnormal FMRP expression in sub-cortical sites does not result in abnormal cortical resting EEG.

*3.3.2 ERP amplitudes were not affected in either global or midbrain specific Fmr1 KO mice*

Event related potentials (ERPs) show consistently timed peaks (named P1, N1, P2), which are evoked at specific latencies after sound onset. The peaks reflect population synchronous activity with P1 being mostly related to thalamocortical input, N1 relating to cortical processing and P2 related to arousal mechanisms. Measuring the amplitudes and latencies of these waves allow for the assessment of response synchrony or hypersensitivity to sound presentation. While the ERPs reflect time domain synchrony, it is also possible to measure single trial non-phase locked power (STP) during the ERP stimulus train. STP reflects the background activity of neural generators during acoustic stimulation. Previous studies have shown elevated ERP amplitudes and increased gamma band STP in both humans with FXS and global *Fmr1* KO mice.

The ERP waveform is the averaged response, across 200 presentations of noise bursts (onset at 0 ms; 100 ms duration) presented at 70 dB SPL with a repetition rate of 0.25 Hz from WT (n=8), *Fmr1* KO (n=10), $Fmr1^{Flox/y}$ (n = 12) and $Cre^{Ntsr1}/Fmr1^{Flox/y}$ cKO mice (n = 16). We used Student's unpaired t-test with correction for multiple comparisons to analyze the amplitude (μV) and latency (ms) of the positive (P) and negative (N) peaks of the P1, N1, P2, and N2 deflections of the ERP waveform. For each cortical region (AC and FC), comparisons were made for global-KO mice (Figure 2A, B) and cKO mice (Figure 2C, D) with their respective littermate controls. Mice with global deletion of *Fmr1* (*Fmr1* KO) did not display elevated N1 amplitude phenotype reported

previously. No significant differences in amplitude between *Fmr1*$^{Flox/y}$ and *Cre*$^{Ntsr1}$*/Fmr1*$^{Flox/y}$ cKO were found in AC or FC either.

*3.3.3 Elevated single trial power is seen in global Fmr1 KO mice but not with midbrain specific deletion*

Single-trial power (STP) is a measure of the average total non-phase-locked power during ERP stimulus presentation and was calculated for each mouse. Grand average matrices were calculated for each genotype across 200 presentations of noise bursts (onset at 0 ms; 100 ms duration) at 70 dB SPL. This is an estimate of background 'noisy' activity during acoustic stimulation. STP is significantly increased in global *Fmr1* KO mice compared to littermate controls in the AC and the FC (Figure 3A, B), as seen in previous studies. In each panel, the top two small panels show the average STP in the control groups and the KO mouse models. The larger bottom panel in each figure panel shows the KO-control (subtraction). Significant differences between groups are outlined in the larger panels. Monte-Carlo permutations were used to compare genotypes across time and frequency: statistical cluster analysis reveals contiguous time × frequency regions that are significantly different between genotypes in AC and FC in the >30 Hz range (Figure 3A,B). i.e., the global *Fmr1* KO mice show significantly higher power in the gamma range compared to WT mice in both AC and FC. However, in the *Cre*$^{Ntsr1}$*/Fmr1*$^{Flox/y}$ cKO mice, the STP was similar to the flox-controls. (AC, Figure 3C). In the FC, there is a significant difference between groups, but the *Cre*$^{Ntsr1}$*/Fmr1*$^{Flox/y}$ cKO mice showed reduced STP (FC, Figure 3D) compared to the control. Taken

together, these data show abnormally high background cortical activity in the global *Fmr1* KO, but not if FMRP is deleted sub-cortically.

### *3.3.4 Temporal processing deficits are seen in global and midbrain specific Fmr1 KO mice*

The 40 Hz gap-ASSR paradigm was used to test temporal processing fidelity in cortical responses across groups. In this paradigm, gaps of different widths (2, 4, 6, 8, 10, 12 ms) and modulation depths (50, 75, and 100%) are introduced with a repetition rate of 40 Hz in continuous noise. If the neural generators in the AC and FC detect the gaps and respond with consistent phase angles across trials with respect to the gaps, then the inter-trial phase clustering (ITPC) will be high, with a theoretical maximum of 1, if all responses had the same phase relationship with the stimulus. The theoretical low is 0, if every trial produced a different phase relationship between stimulus and response. For each mouse, ITPC was measured to determine the degree of phase locking across trials for each combination of gap width and modulation depth. Figure 4A-H show heat maps representing mean ITPC measured in AC and FC (100% modulation depth and 12 ms gap width) across the 4 groups. The population statistics are shown in Figure 4I-P. Repeated measures two-way Anova with Geisser-Greenhouse correction was run to identify main effects and interaction of genotype and gap width. Bonferroni correction was applied to multiple comparisons. There is reduced ITPC in the global *Fmr1* KO group compared to WT (Figure 4I, J, M, N). Significant genotype difference is seen between global *Fmr1* KO and WT littermates in AC for 100% modulation depth (*p=0.0342, Figure 4K) and significant interaction for gap x genotype for 75% depth (*p=0.023, Figure 4M). In the

FC, significant differences are seen for 100% modulation depths (*p=0.0073, Figure 4J) and 75% depth (*p=0.0324, Figure 4N). Line graphs depicting ITPC values of adult $Cre^{Ntsr1}/Fmr1^{Flox/y}$ cKO mice compared to *Fmr1*-flox littermates (Figure 4K, L, O, P) show that the midbrain specific deletion also affects gap-ASSR ITPC. Significant interaction effect between gap width x genotype were seen in the AC for 75% AM (*p<0.0001, Figure 4O), but not for 100% AM (Figure 4K). No genotype differences in ITPC or significant interactions were found in the FC in the midbrain specific *Fmr1* KO mice. Taken together, both FC and AC of the global *Fmr1* KO mice show impaired temporal processing. When FMRP is removed from the midbrain, there are ITPC deficits in the AC, but not the FC.

*3.3.5 PNN expression is unaltered by deletion of FMRP in the midbrain and brainstem*

Reduced PNN expression surrounding inhibitory neurons has been reported in the AC of global *Fmr1* KO mouse models of FXS, which may be a result of abnormally high MMP-9 enzymatic cleavage activity in the cortex, resulting in disrupted inhibition in cortical circuits (Sidhu et al., 2014; Gkogkas et al., 2014; Wen et al., 2018). We examined PNN expression in the AC and IC of the midbrain deletion model (**Figure 5**) in cKO mice (n=6) and littermate controls (n=6; labeled as "WT"). PNN expression was measured using two variables: PNN density and intensity. Density was calculated as PNN count/$mm^2$ area, and intensity was the fluorescence level for each brain region analyzed The central IC was separated into "upper" and "lower" IC. There was no difference in density or intensity found in the AC, upper IC, and lower IC between cKO and control

littermates. Student's t-tests were used to compare PNN density and intensity between genotypes for each region (all $p>0.05$).

### *3.3.6 Hyperactivity is absent in mice with subcortical deletion of FMRP*

We used the OF and EPM behavioral paradigms to measure hyperactivity and anxiety-like behavior in mice with subcortical deletion of *Fmr1*. Global KOs of FMRP display anxiety-like behaviors and hyperactivity in the OF and EPM, demonstrated through thigmotaxis levels and number of entries into different subdivisions of the arenas. The OF is a square arena surrounded by high walls all around, and mouse behavior within the arena is analyzed based on its movement within the center and surrounding areas. Thigmotaxis is used as a measure of anxiety (time spend near wall and away from center of arena), and bouts of entry into the various subdivisions of the arena is measured as a read-out of hyperactivity. The EPM is a 4-arm maze with two open and two closed arms; time spent in closed vs open arms and center is measured as a reflection of anxiety levels, and number of bouts into the different arms is measured for hyperactivity. In the OF and EPM paradigms (**Figure 6**), hyperactivity is absent in mice with subcortical deletion of FMRP. On the contrary, mice with *Ntsr1*-mediated KO of FMRP show significantly less distance traveled in the EPM compared to control littermates ($*p<0.05$). No difference in the # bouts (entry into closed or open arms) or in the percent time spent in the individual arms was present between the genotypes. In the OF, cKO showed no difference compared to control in the distance traveled in the open field arena, in number of bouts between thigmotaxis and center, or in the percent time spent in the center of the arena or

thigmotaxis. For OF and EPM, statistical analysis was performed with Wilcoxon rank sum test, and data represent median and interquartile ranges.

*Resting*

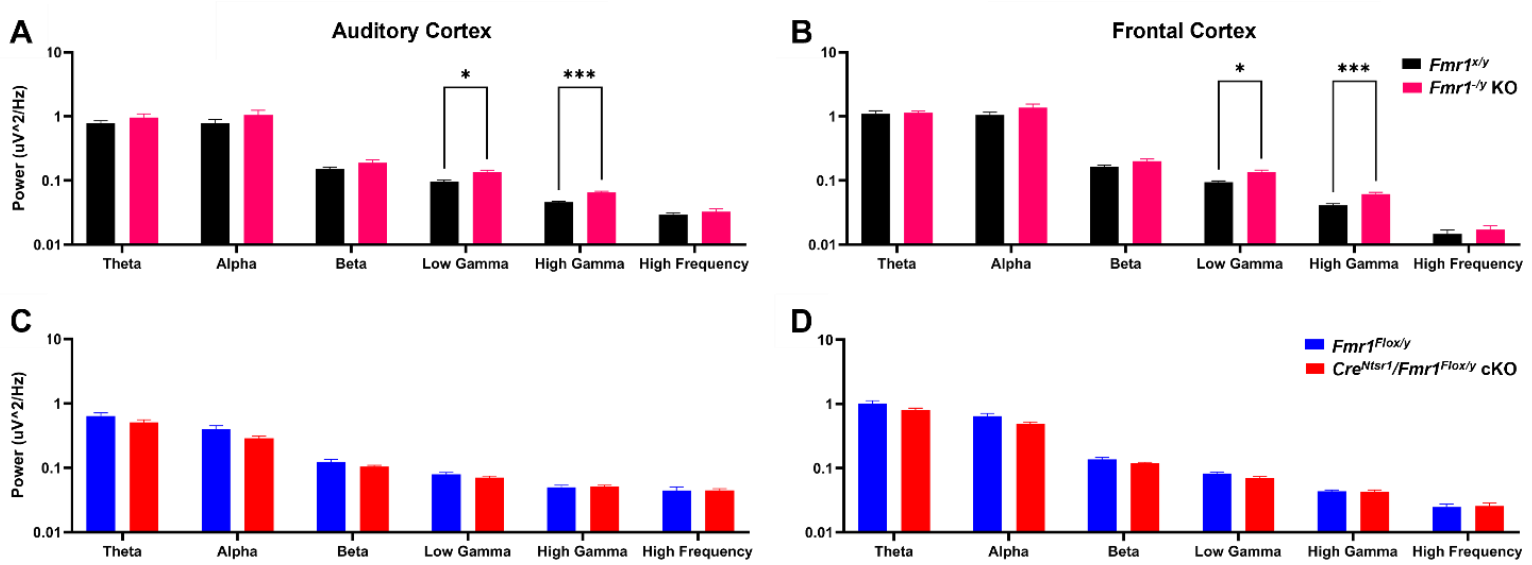


*Figure 3.1. Midbrain excitatory neuron-specific deletion of Fmr1 does not change resting power spectral density in auditory (AC) or frontal cortex (FC) of adult mice*

Five minutes of resting EEG data (in the absence of auditory stimulation) from electrodes implanted in the AC and FC of *Fmr1* KO (n=10), WT (n=8), $Fmr1^{Flox/y}$ (n = 12) and $Cre^{Ntsr1}/Fmr1^{Flox/y}$ cKO mice (n = 16) was recorded. Spectral power density (μV2/Hz) was calculated for each segment using fast Fourier transform, followed by averaging all segments for a given mouse in the AC (A, C) and FC (B, D). These individual averages then contributed to the grand average for each genotype. Values were divided into standard frequency bins (Theta, 4-7 Hz; Alpha, 8–13 Hz; Beta, 14-30 Hz; Low Gamma, 30-59 Hz; High Gamma, 60-100 Hz). (A, B) Full *Fmr1* KO mice displayed the KO phenotype in resting EEG, namely increased power in the gamma band compared to WT. AC: low gamma, *p = .0033; high gamma, ***p < .0001; FC *low gamma, p = .0079; high gamma, ***p < .0001 (C, D) No significant differences in relative power between $Fmr1^{Flox/y}$ and $Cre^{Ntsr1}/Fmr1^{Flox/y}$ cKO were found in AC or FC. Multiple Mann-Whitney analysis was used with Bonferroni correction for multiple comparisons, resulting in $\alpha = .0083$ to account for six frequency bands.

*Event-Related Potential*

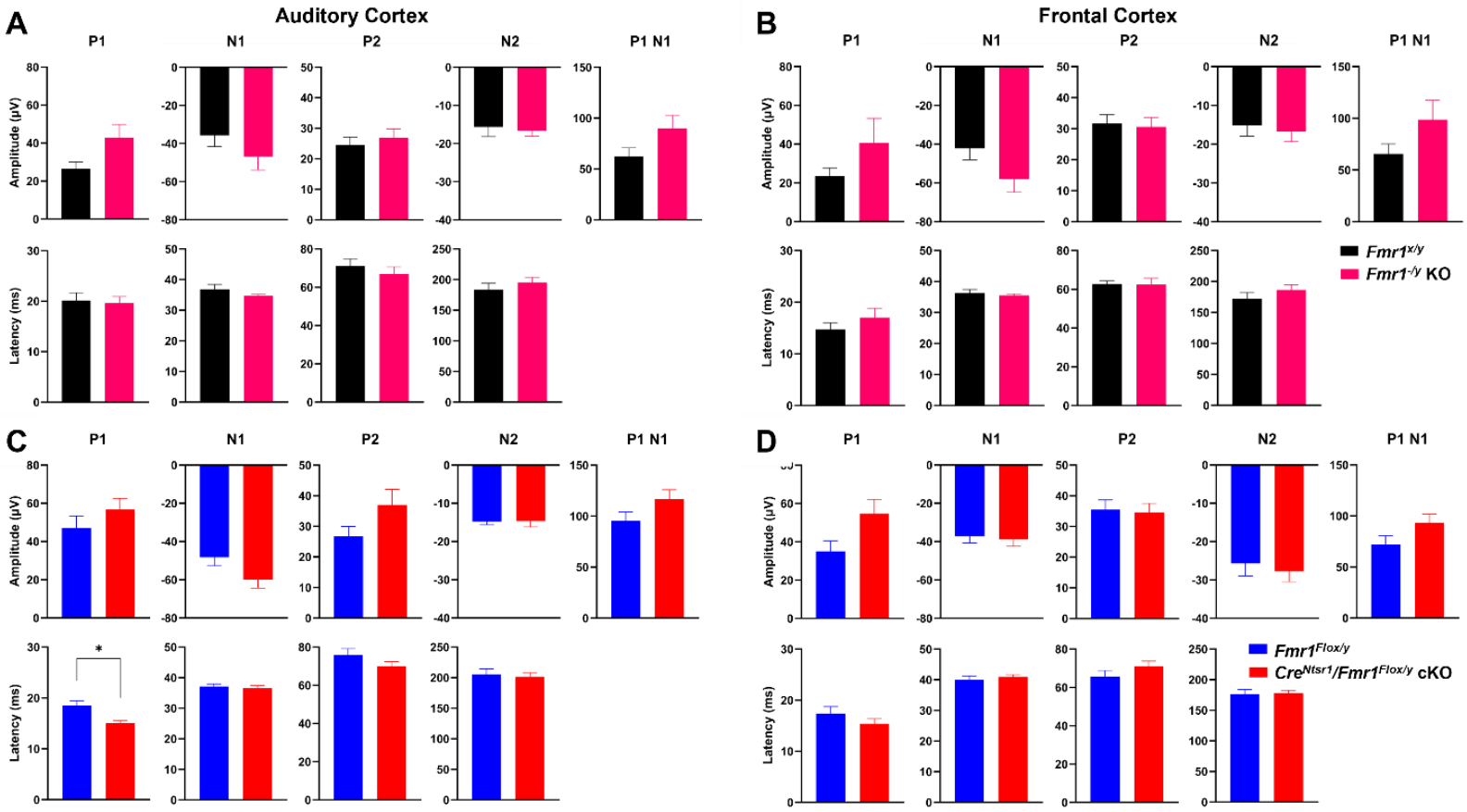

*Figure 3.2. Midbrain excitatory neuron-specific deletion of Fmr1 does not change ERP amplitude in the AC or FC of adult mice*

The ERP waveform is the averaged response, across 200 presentations of noise bursts (onset at 0 ms; 100 ms duration) played at 70 dB at a repetition rate of 0.25 Hz and a rise/fall rate of 5 ms, recorded from the AC and FC of WT (n=8), *Fmr1* KO (n=10), $Fmr1^{Flox/y}$ (n = 12) and $Cre^{Ntsr1}/Fmr1^{Flox/y}$ cKO mice (n = 16). We used Student's unpaired t-test with correction for multiple comparisons to analyze the amplitude (μV) and latency (ms) of the positive (P) and negative (N) peaks of the P1, N1, P2, and N2 deflections of the ERP waveform, as well as the combined magnitude size of P1 and N1 (P1 N1). For each cortex (AC and FC), comparisons were made for global-KO mice (A, B) and cKO mice (C, D) with their respective littermate controls, resulting in $\alpha = 0.0056$ to account for 9 comparisons. (A, B) Mice with global deletion of *Fmr1* (*Fmr1* KO) did not display elevated N1 amplitude phenotype characteristic to FXS. (C, D) No significant differences in amplitude between $Fmr1^{Flox/y}$ and $Cre^{Ntsr1}/Fmr1^{Flox/y}$ cKO were found in AC or FC. (C) The bottom left-most comparison reveals significantly shorter P1 latency in $Cre^{Ntsr1}/Fmr1^{Flox/y}$ cKO mice compared to $Fmr1^{Flox/y}$ ($p=0.0016$). All comparisons otherwise had p-value $p>0.0056$.

*Single-trial Power (STP)*

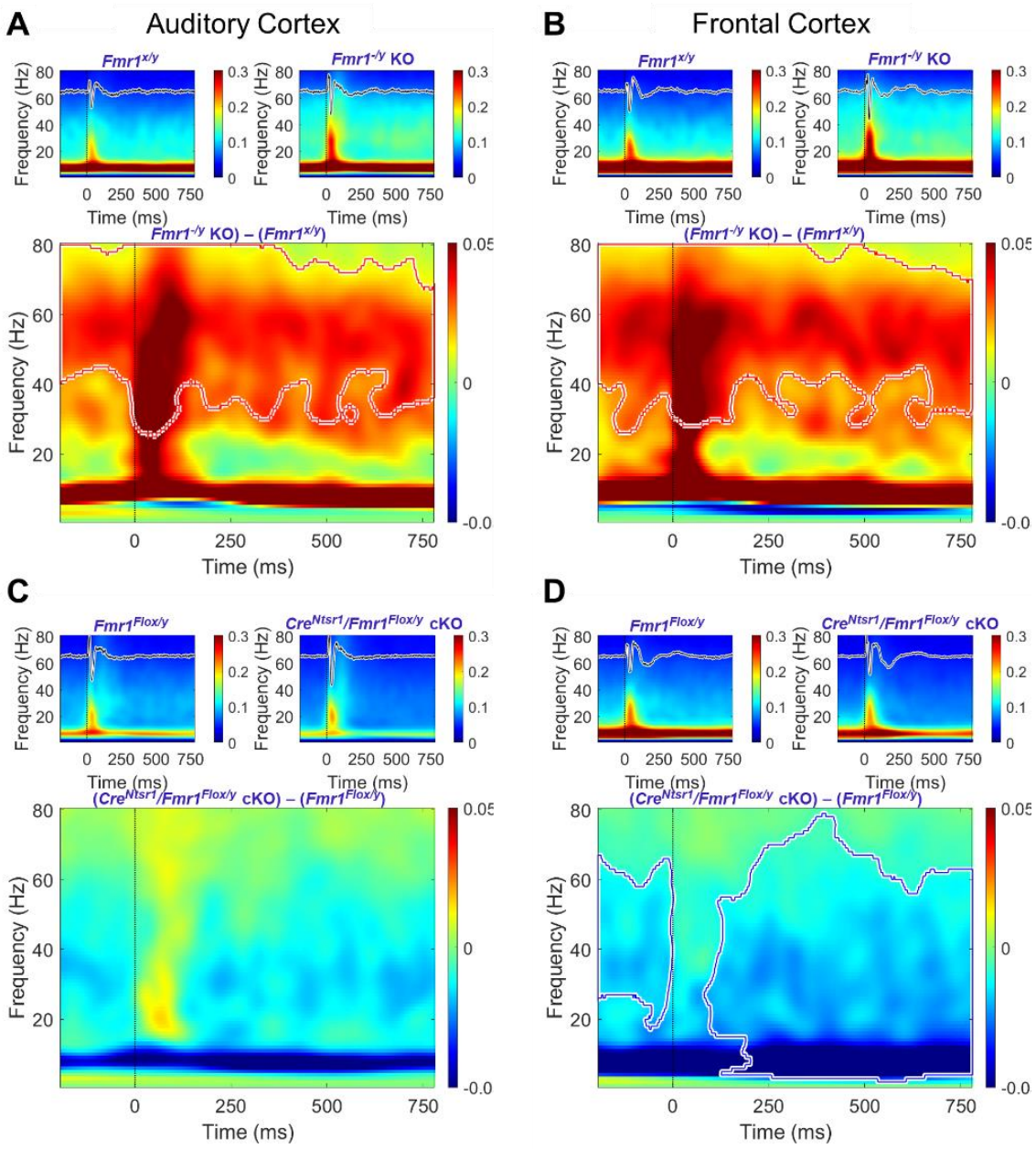

*Figure 3.3. Single-trial power (STP) is increased in global Fmr1 KO compared to littermate controls*

This is not seen in the midbrain specific deletion model. Indeed, STP is reduced in the frontal (FC) but not in auditory cortex (AC) of adult $Cre^{Ntsr1}/Fmr1^{Flox/y}$ cKO mice (n=16) during broad-band noise burst stimulation compared to $Fmr1^{Flox/y}$ controls (n=12). STP is a measure of the average total non-phase-locked power during sound presentation and was calculated for each mouse. Grand average matrices were calculated for each genotype across 200 presentations of noise bursts (onset at 0 ms; 100 ms duration) played at 70 dB at a repetition rate of 0.25 Hz and a rise/fall rate of 5 ms.
Top two panels within (A) and (B) show the average STP in the $Fmr1^{x/y}$ (left; n=8) and $Fmr1^{-/y}$ KO mice (right; n=10) groups with the ERP waveform superimposed. The bottom panel shows a subtraction of group STP ($Fmr1^{-/y}$ KO – $Fmr1^{x/y}$). KO show significantly higher power in the gamma range compared to WT. Monte-Carlo permutations were used to compare genotypes across time and frequency: statistical cluster analysis reveals contiguous time × frequency regions that are significantly different between genotypes in AC and FC in the >30 Hz range. Red dashed contours (mean positive group difference) indicate these significant clusters. Top two panels within (C) and (D) show the average STP in the $Fmr1^{Flox/y}$ (left; n=12) and $Cre^{Ntsr1}/Fmr1^{Flox/y}$ cKO mice (right; n=16) groups with the ERP waveform superimposed. The bottom panel shows a subtraction of group STP ($Cre^{Ntsr1}/Fmr1^{Flox/y}$ cKO – $Fmr1^{Flox/y}$). Monte-Carlo permutations were used to compare genotypes across time and frequency: significant clusters were found in FC but not in AC. Red solid contours (mean negative group difference) indicate these significant clusters.

*Gap ASSR*

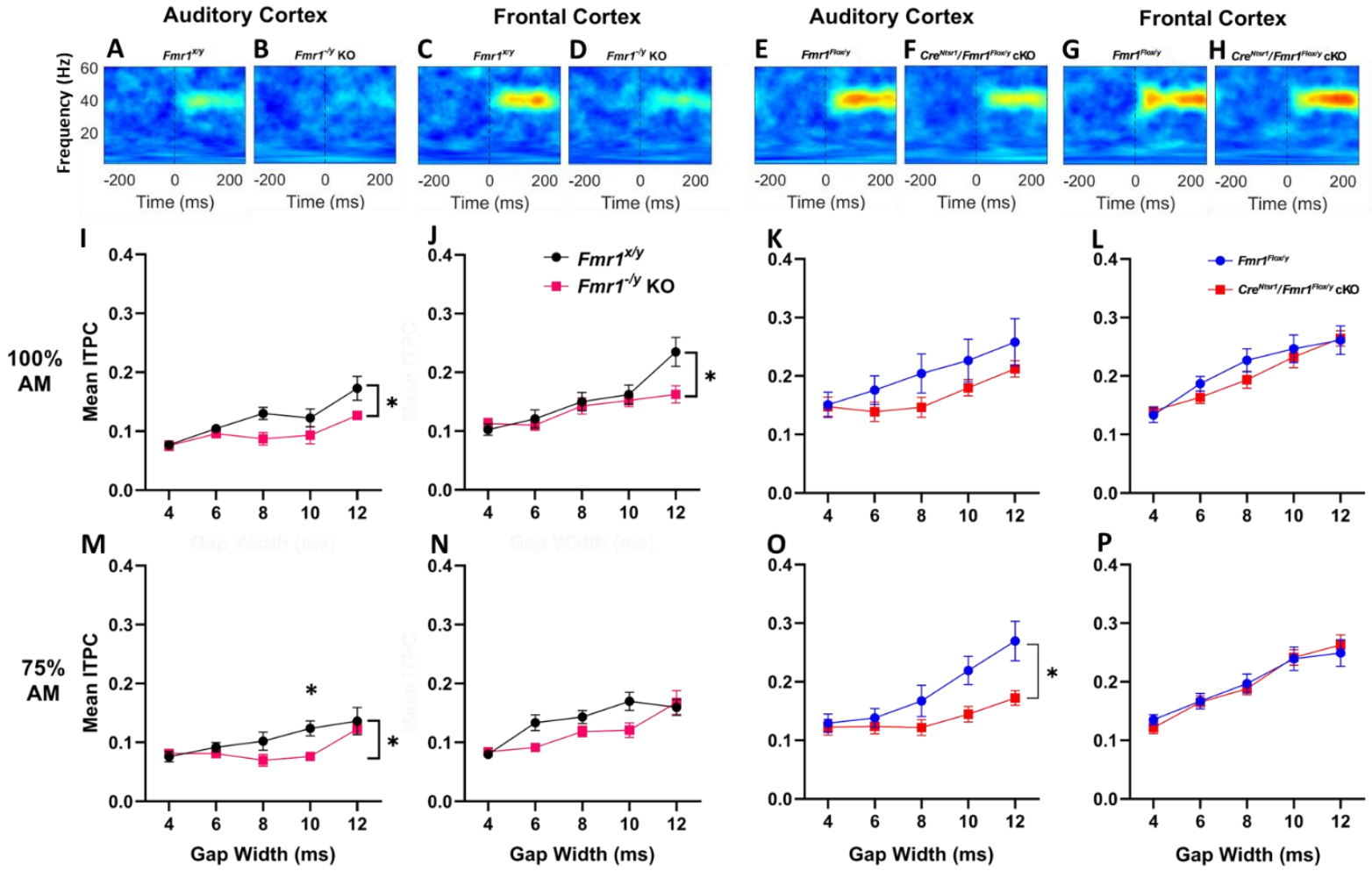
Auditory Cortex
Frontal Cortex
Auditory Cortex
Frontal Cortex
A Fmr1x/y
B Fmr1-/y KO
C Fmr1x/y
D Fmr1-/y KO
E Fmr1Flox/y
F CreNtsr1/Fmr1Flox/y cKO
G Fmr1Flox/y
H CreNtsr1/Fmr1Flox/y cKO
Frequency (Hz)
60
40
20
-200 0 200
Time (ms)
I
J
K
L
100% AM
Mean ITPC
Fmr1x/y
Fmr1-/y KO
Fmr1Flox/y
CreNtsr1/Fmr1Flox/y cKO
0.4
0.3
0.2
0.1
0.0
4 6 8 10 12
Gap Width (ms)
M
N
O
P
75% AM
*

*Figure 3.4. Reduced inter-trial phase clustering (ITPC) in phase-locking to auditory "gap ASSR" stimuli is present in the auditory (AC) and frontal cortex (FC) of adult global Fmr1 KO mice compared to control littermates, and this phenotype is reproduced in the AC but not FC by midbrain deletion of FMRP*

Constant noise presentation was interspersed with gaps of sound attenuation presented at a rate of 40 Hz and of varying widths (2, 4, 6, 8, 10, 12 ms) and amplitude modulation (AM) depths (100% and 75%). For each mouse, ITPC was measured to determine the degree of phase locking across trials within each combination of gap width and modulation depth. (A-E) Heat maps representing mean ITPC measured in AC and FC in response to gaps in noise across trials with 100% modulation depth and 12 ms gap width in the (A) WT littermates and (B) global *Fmr1* KO mice in the AC, (C) WT littermates and (D) global *Fmr1* KO mice in the FC, (E) control *Fmr1*-flox littermates and (F) *Ntsr1*-Cre mediated *Fmr1* conditional KO mice in the AC, and (G) control *Fmr1*-flox littermates and (H) *Ntsr1*-Cre mediated *Fmr1* conditional KO mice in the FC. (I-J, M-N) Line graphs depicting ITPC values of adult global *Fmr1* KO mice compared to WT littermates in response to gap in noise across 2-12 ms gap widths and (I, J) 100% and (M, N) 75% AM in the (I, M) AC and (J, N) FC. There is reduced ITPC in the KO group compared to WT. Significant genotype difference between global *Fmr1* KO and WT littermates in AC for (K) 100% AM (*p=0.0342) and significant interaction for gap x genotype for (O) 75% AM (*p=0.023) and for in FC for (J) 100% AM (*p=0.0073) and (N) 75% AM (*p=0.0324). (K-L, O-P) Line graphs depicting ITPC values of adult $Cre^{Ntsr1}/Fmr1^{Flox/y}$ cKO mice compared to *Fmr1*-flox littermates in response to gap in noise across 2-12 ms gap widths and (K, L) 100% and (O, P) 75% AM in the (K, O) AC and (L, P) FC. Significant interaction effect between Gap Width x Condition in AC for (O) 75% AM (*p<0.0001) but not for (K) 100% AM. No genotype differences in ITPC or significant interactions were found in the FC. Repeated measures two-way Anova with Geisser-Greenhouse correction was run to identify main effects and interaction of genotype and gap width. Bonferroni correction was applied to multiple comparisons.

*PNN Expression*

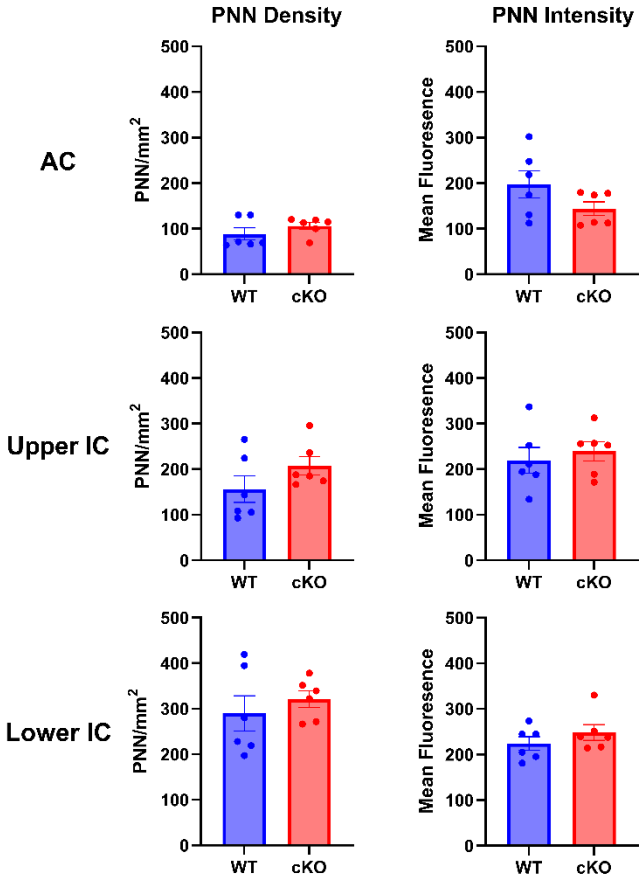


*Figure 3.5. PNN expression is unaltered in the AC and IC by subcortical deletion of FMRP*

PNN density was calculated as PNN count/mm$^2$ area, and PNN intensity was measured as the mean fluorescence across mouse brain slices for each brain region analyzed (AC, central IC). The central IC was separated into two ROIs, indicated as "upper" and "lower" IC. Each row displays PNN density (left) and PNN intensity (right) for each ROI: AC (top row), upper IC (middle row), and lower IC (bottom row). There were no differences between cKO and WT flox-littermates in PNN density or intensity in any of the brain regions analyzed. T-tests were used to compare cell counts between genotypes for each region. PNN staining in this study is limited to WFA+ PNNs. For each animal, 2-3 slices containing AC and inferior colliculus (IC) were taken and processed for PNN staining. n=6 cKO and n=6 WT flox-littermate controls.

*Behavior*

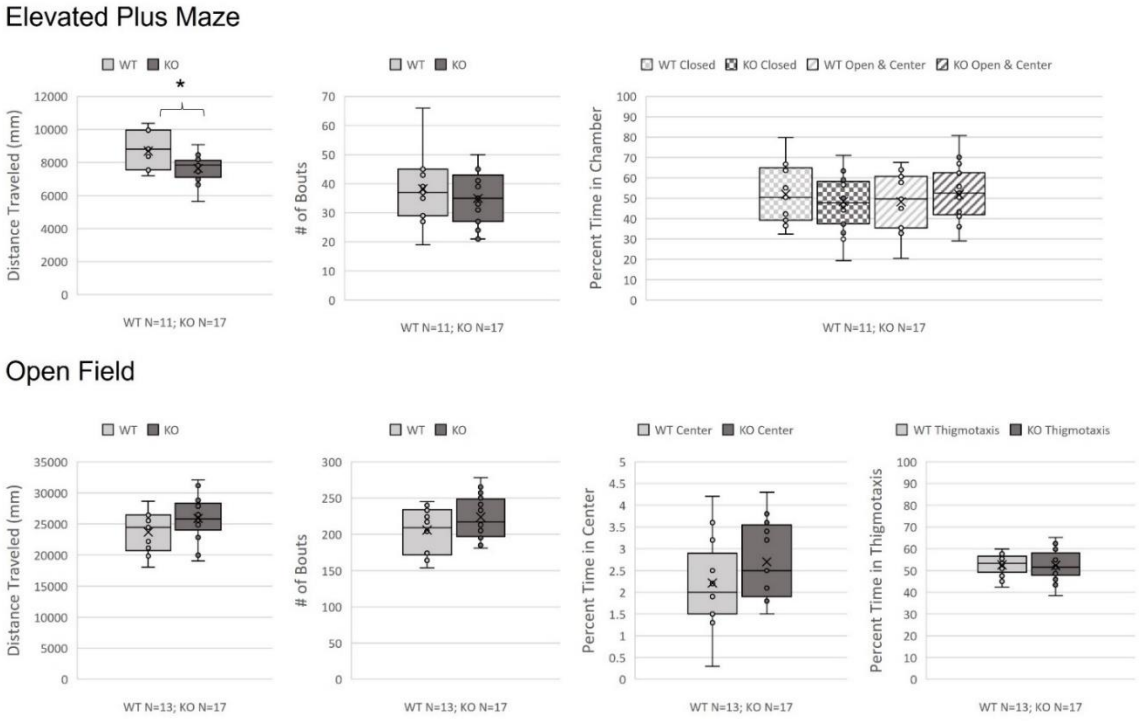


*FIGURE 3.6. Behavior: Elevated Plus Maze. KO show significantly less distance traveled in the EPM compared to Control (Wilcoxon rank sum test, and data represent median and interquartile ranges; *p<0.05)*

No difference in the # bouts (entry into closed or open arms) or in the percent time spent in the individual arms. Open Field. KO show no difference compared to control in the distance traveled in the open field arena, number of bouts between thigmotaxis and center, or in the percent time spent in the center of the arena or thigmotaxis (Wilcoxon rank sum test, and data represent median and interquartile ranges).

### 3.4 Discussion

The goal of this study was to investigate the contribution of FMRP expression in the midbrain and brainstem to FXS biomarkers in resting EEG, evoked and single trial power, and phase-locking to amplitude-modulated sounds in the AC and FC of mice, as well as hyperactive behavior in the OF and PNN expression levels in the AC and IC. We found that midbrain and brainstem deletion of FMRP reduced phase-locking in the AC to amplitude-modulated sound signals, while resting EEG and evoked auditory responses were unaffected. Our results suggest that temporal-processing deficits in FXS originate from the loss of FMRP in the auditory midbrain and brainstem. Furthermore, we measured PNN levels in the AC and IC, a key auditory brain region located in the midbrain, and tested hyperactivity levels using the OF paradigm. We found no effects on PNN expression or on hyperactivity in the OF.

We also recorded ERP, resting EEGs and quantified ITPC of global *Fmr1* KO mice compared to littermate controls in response to gaps in continuous noise. In the global *Fmr1* KO mouse model, EEG signals in the AC showed elevated gamma power at rest and elevated STP during noise burst stimulation. We did not see a significant elevation of ERP N1 amplitudes in the global KO, although a trend was seen. Global *Fmr1* KO mice showed deficits in ITPC in response to gap ASSR stimulus in both AC and FC. Taken together, these results show similar deficits in power and temporal processing reported previously (Lovelace et al., 2018).

*Ntsr1* is expressed in the midbrain (superior, inferior colliculus, periaqueductal gray), cerebellum and cochlear nucleus (GENSAT, 2003). In the present study, we found

that *Ntsr1*-mediated deletion of FMRP does not result in resting power or STP deficits that are seen in the global KO mice. Behavioral abnormalities or PNN deficits were also not present. However, a significant temporal processing deficit was observed as measured with ITPC in the gap-ASSR paradigm. Interestingly, the ITPC deficit was only seen in the AC, but not the FC.

FMRP is expressed throughout the auditory pathway. Deleting FMRP in the global KO model has implications throughout the auditory system. Lovelace et al. (2020) used the Nex-1 promoter in male C57bl/6 J mice for deletion of FMRP in the forebrain, leaving FMRP expression intact elsewhere. They found elevated low gamma power in resting EEG, elevated induced power, increased single-trial power (STP) in the 20-60 Hz range, but no change in ITPC to a chirp stimulus. Behaviorally, they found hyperactivity in the conditional KO (cKO) group compared to wild-type (WT) mice. These findings suggest that forebrain expression of FMRP is critical to regulating resting EEG, induced power, and behavioral phenotypes connected to hyperactivity, but not to phase-locking to amplitude modulation of sound signals. Another paper published by Rais et al. (2022) uses the Camkii promoter to test two forebrain FMRP cKO models: cOFF, in which FMRP is deleted only in the forebrain excitatory cells, and cON, in which FMRP is only expressed in forebrain excitatory cells starting at P14. cOFF mouse model replicated elevated gamma power compared to WT, elevated STP in the 40-60 Hz range and elevated induced power. cON mouse model compared to full KO showed reduced low gamma power, reduced STP in the 30-70 Hz range, elevated ITPC in the 40-60 Hz range in response to chirp, and reduced induced power compared to global *Fmr1* KO.

Combined with forebrain-specific deletion models which showed resting power. STP, ERP increase and hyperactivity, these studies suggest a systems level double dissociation of FXS outcomes – with forebrain FMRP playing a dominant role in cortical power and hyperexcitability, and the midbrain FMRP expression playing an important role in cortical temporal processing. This interpretation is also supported by Holley et al. (2022) who found that re-expression of FMRP in the midbrain using the Ntsr1 promoter restores cortical ITPC suggesting that midbrain expression of FMRP is sufficient to rescue temporal deficits in processing amplitude-modulated sounds. Behaviorally, hyperactivity and anxiety-like behaviors in the OF and EPM previously described to be present in *Fmr1* KO models of FXS (cite papers) were not seen with midbrain deletion of FMRP, though this set of behaviors was recapitulated with forebrain deletion of FMRP (Lovelace et al., 2020; Rais et al., 2022), suggesting that anxiety-like behaviors are largely mediated by the forebrain.

### *3.4.1 Significance of gap ASSR protocol: association between gap ASSR stimulus and speech*

The gap ASSR protocol was developed by Rumschlag & Razak (2021) to synthetically mimic specific elements of speech and to elucidate auditory acuity. It is continuous noise interspersed by repeated gaps presented at a rate of 40 Hz to generate a steady-state response in the AC that phase-locks to the gaps across trials. Our goal was to maximize how closely the protocol the natural, constant amplitude fluctuations and gaps in sounds, including speech. The gap ASSR protocol was designed to resemble speech envelope of sounds by capturing two major factors in sound processing: gaps between the

different components of the sounds and amplitude modulation. Therefore, it was designed to operate on two key parameters of speech: amplitude-modulation depth and gap width. The gap widths chosen are 2-12 ms because it is in the range of gap detection in humans, mice, and gerbils, and it resembles the time-range of voice-onset sounds (Harris et al., 2012). Furthermore, we chose noise rather than pure tone presentation to further resemble naturally occurring noise. Overall, the gap ASSR protocol is close enough to the naturally occurring variability in sounds and speech that can be tested in a mouse model.

### *3.4.2 How does the expression of FMRP in the midbrain regulate phase-locking in the AC and FC*

Phase-locking to temporal dynamics of auditory signals depends largely on midbrain function (Anderson et al., 2010a; 2010b). Elevated excitability in the IC in FXS (Nguyen et al., 2020) may produce increased noise in neural encoding of auditory signals that propagate to the AC, ultimately reducing precision in neural timing. Furthermore, elevated excitatory compared to inhibitory inputs in the brainstem suggests an even earlier station in the auditory pathway where hyperexcitability to sounds is present (Garcia-Pino et al., 2017), contributing to elevated excitation/inhibition ratio. Additionally, various human conditions which have implications for hearing and/or speech and language demonstrate reduced signal-to-noise ratio (Kraus et al., 2017). Inhibitory interneurons play a pivotal role in temporal regulation and gap encoding in the cortex. Optogenetic suppression of PV and somatostatin-positive neurons in the AC during pre-gap and post-gap intervals decrease and increase gap detection, respectively (Weible et al., 2014). Ultimately, midbrain projections, if altered, may disrupt the

precision of these mechanisms, and may reduce temporal fidelity of signal propagation to and within the AC. We found in the present study that the signal in AC displays phase-locking deficits in the absence of FMRP expression in the midbrain, while phase-locking in the FC continues to resemble the control-littermate phenotype. This discrepancy may be a result of circuits in the FC that entrain 40 Hz resonance independently of IC function. GABAergic neurons in the basal forebrain, namely PV+ neurons, facilitate 40 Hz oscillations, and their activity is necessary and sufficient for this cortical entrainment in the FC and for 40 Hz ASSR in response to click train presentation (Kim et al., 2015). PV neurons in the basal forebrain may entrain PV neurons in the FC, thus propagating a 40 Hz oscillator to the FC independent of the strength of ASSR in the AC.

*3.4.3 Subcortical role for phase-locking to auditory signals*

There is vast evidence in the literature that suggests that subcortical auditory structures in the midbrain and brainstem play a crucial role in following rapid temporal fluctuations in auditory signals. The frequency following response (FFR) is an example of this phenomenon. The frequency following response (FFR), sometimes known as the auditory brainstem response to complex sounds (cABR), is an auditory evoked potential recorded electrophysiologically from the scalp that phase-locks to auditory stimuli with periodic characteristics (Kraus et al., 2017). The FFR has been widely studied in various human conditions that impact auditory function, including ASD, noise-induced hearing loss, aging, and language and speech impairment. The FFR reflects the neural encoding of the spectrotemporal structure of sounds. FFRs have been recorded in humans and animal models in response to pure tones repeatedly presented and to more complex

stimuli such as consonant vowels and other speech stimuli (Chandrasekaran & Kraus, 2010). The level of phase-locking present in the FFR has been studied in various human conditions that have implications for hearing, including aging (Clinard et al., 2010; Anderson et al. 2013a, b; Clinard & Tremblay, 2013), language and speech impairments (Basu et al. 2010; Rocha-Muniz et al., 2012; White-Schwoch et al., 2015b), and hearing loss (Kraus et al., 2017). The FFR originates from the midbrain and brainstem (Smith et al., 1975; Glaser et al., 1976; Batra et al., 1986; Galbraith 1994), i.e., the cochlear nucleus, superior olive, and inferior colliculus, which are understood to generate high-frequency phase-locking in the auditory system and transmit this information to the cortex. The FFR has been demonstrated to be a "composite response," in that it originates from cortical and subcortical areas and composed of their simultaneous activities (Tichko & Skoe, 2017).

The FFR has been much explored in the context of language, especially in understanding how the auditory system encodes speech (Krishnan 2002). Notably, language impairments in ASD have been shown to be related to auditory processing deficits in the auditory brainstem, in which children with ASD demonstrate deficient encoding of pitch, i.e., pitch tracking (Russo et al., 2008), although this was shown to be only in a subset of children with ASD (Russo et al., 2010). Children with ASD show reduced encoding of signal in background noise (Russo et al., 2010), which is also present in age-related deficits of auditory processing (Anderson et al., 2011).

The phase-locking characteristic of the FFR and its origin in the midbrain and brainstem suggest a relationship to our findings in this study. With midbrain deletion of

FMRP, we see a decline in the phase-locking of the AC steady state to gaps presented at a rate of 40 Hz. Interestingly, this effect is not in the FC, nor is there an impact to phase-locking of the AC or FC to the classic 40-Hz click ASSR stimulus involving clicks presented at 40 Hz.

*3.4.4 Connectivity between forebrain and midbrain*

Direct projections from the AC to the IC have been shown to exert corticofugal modulation of the IC neuron tuning and responses to sounds. Layer V cortical neurons in the primary AC and anterior auditory field (AAF) connect to all subsections of the IC (dorsal, ventral, and central), with the majority of connections to dorsal and ventral layers. Layer VI also provides an additional 10% of corticocollicular projections. The majority of the corticollicular connections are ipsilateral, and 15% are contralateral (reviewed by Bajo & King, 2013). The tunings of neurons in the IC are sharpened and made more precise ("compressed representation") by cortical neurons of matched tuning, or they may be shifted by neurons of different tuning, creating a broader frequency representation ("expanded representation;" reviewed by Suga 2012). IC neuron populations exhibit "sub-millisecond precision" of encoding speech signals in the gerbel (Garcia-Lazaro et al., 2013), alluding to the critical role of temporal precision in the IC. Furthermore, in layer V of AC, there is a population of pyramidal neurons known as intrinsic bursting cells, which exhibit brief intrinsic bursts at high frequencies (<25 ms). Based on their physiological properties, burst action potentials represent and relay information more reliably than non-bursting action potentials, thus playing an essential

role in cortical oscillations and information processing of signals with temporal accuracy (Lisman 1997).

Multiple defining elements of sounds are encoded in the IC, and the IC neuronal population encoding of these elements are affected by the manipulation of A1 (i.e., stimulation or deactivation. These include sound frequency, intensity, duration, and location (Ma and Suga, 2001a; 2001b; Yan & Ehret, 2002; Yan & Zhang, 2005; Zhou & Jen, 2005; Nakamoto et al., 2008). This degree of modulation provides a mechanism for the cortex to selectively strengthen the bottom-up representation of relevant auditory signals, further enhancing auditory processing in the IC up to the cortex (Bajo & King, 2013).

### 3.5 Conclusion

The key finding in this study is that the auditory midbrain and brainstem are critical to temporal processing of sounds. Altering the subcortical auditory structures produces temporal processing deficits, while altering forebrain structures produces resting, evoked, and induced power deficits. Elevated oscillatory power in the forebrain and reduced phase-locking in cortical and subcortical structures may be associated with altered excitation/inhibition balance, altered signal-to-noise ratio, and reduced spectrotemporal acuity of auditory signals. We propose that future treatments for FXS target the underlying mechanisms of auditory sensory deficits while considering nuances of cortical and subcortical contributions.

**References**


Anderson S, Skoe E, Chandrasekaran B, Kraus N. Neural timing is linked to speech perception in noise. J Neurosci. 2010a Apr 7;30(14):4922-6. doi: 10.1523/JNEUROSCI.0107-10.2010. PMID: 20371812; PMCID: PMC2862599.

Anderson S, Skoe E, Chandrasekaran B, Zecker S, Kraus N. Brainstem correlates of speech-in-noise perception in children. Hear Res. 2010b Dec 1;270(1-2):151-7. doi: 10.1016/j.heares.2010.08.001. Epub 2010b Aug 12. PMID: 20708671; PMCID: PMC2997182.

Anderson S, Parbery-Clark A, Yi HG, Kraus N. A neural basis of speech-in-noise perception in older adults. Ear Hear. 2011 Nov-Dec;32(6):750-7. doi: 10.1097/AUD.0b013e31822229d3. PMID: 21730859; PMCID: PMC3189261.

Anderson S, Parbery-Clark A, White-Schwoch T, Kraus N. Auditory brainstem response to complex sounds predicts self-reported speech-in-noise performance. J Speech Lang Hear Res. 2013a Feb;56(1):31-43. doi: 10.1044/1092-4388(2012/12-0043). Epub 2012 Jul 3. PMID: 22761320; PMCID: PMC3648418.

Anderson S, Parbery-Clark A, White-Schwoch T, Drehobl S, Kraus N. Effects of hearing loss on the subcortical representation of speech cues. J Acoust Soc Am. 2013b May;133(5):3030-8. doi: 10.1121/1.4799804. PMID: 23654406; PMCID: PMC3663860.

Bajo, V.M. and King, A.J., 2013. Cortical modulation of auditory processing in the midbrain. *Frontiers in neural circuits*, *6*, p.114.

Basu M, Krishnan A, Weber-Fox C. Brainstem correlates of temporal auditory processing in children with specific language impairment. Dev Sci. 2010 Jan 1;13(1):77-91. doi: 10.1111/j.1467-7687.2009.00849.x. PMID: 20121865.

Batra, R., Kuwada, S. and Maher, V.L., 1986. The frequency-following response to continuous tones in humans. *Hearing research*, *21*(2), pp.167-177.

Castrén, M., Pääkkönen, A., Tarkka, I. M., Ryynänen, M., & Partanen, J. (2003). Augmentation of auditory N1 in children with fragile X syndrome. *Brain topography*, *15*, 165-171.

Chandrasekaran, B. and Kraus, N., 2010. The scalp-recorded brainstem response to speech: Neural origins and plasticity. *Psychophysiology*, *47*(2), pp.236-246.

Clinard, C.G., Tremblay, K.L. and Krishnan, A.R., 2010. Aging alters the perception and physiological representation of frequency: evidence from human frequency-following response recordings. *Hearing research*, *264*(1-2), pp.48-55.

Clinard CG, Tremblay KL. Aging degrades the neural encoding of simple and complex sounds in the human brainstem. J Am Acad Audiol. 2013 Jul-Aug;24(7):590-9; quiz 643-4. doi: 10.3766/jaaa.24.7.7. PMID: 24047946.

Cohen, Mike X. Analyzing Neural Time Series Data: Theory and Practice. United States, MIT Press, 2014.

Ethridge, L.E., White, S.P., Mosconi, M.W., Wang, J., Byerly, M.J. and Sweeney, J., 2016. Reduced habituation of auditory evoked potentials indicate cortical hyper-excitability in Fragile X Syndrome. *Translational psychiatry*, *6*(4), pp.e787-e787.

Ethridge, L.E., De Stefano, L.A., Schmitt, L.M., Woodruff, N.E., Brown, K.L., Tran, M., Wang, J., Pedapati, E.V., Erickson, C.A. and Sweeney, J.A., 2019. Auditory EEG biomarkers in fragile X syndrome: clinical relevance. *Frontiers in integrative neuroscience*, *13*, p.60.

Galbraith, Gary C. "Two-channel brain-stem frequency-following responses to pure tone and missing fundamental stimuli." *Electroencephalography and Clinical Neurophysiology/Evoked Potentials Section* 92.4 (1994): 321-330.

Garcia-Lazaro JA, Belliveau LA, Lesica NA. Independent population coding of speech with sub-millisecond precision. J Neurosci. 2013 Dec 4;33(49):19362-72. doi: 10.1523/JNEUROSCI.3711-13.2013. PMID: 24305831; PMCID: PMC3850048.

Garcia-Pino E, Gessele N, Koch U. Enhanced Excitatory Connectivity and Disturbed Sound Processing in the Auditory Brainstem of Fragile X Mice. J Neurosci. 2017 Aug 2;37(31):7403-7419. doi: 10.1523/JNEUROSCI.2310-16.2017. Epub 2017 Jul 3. PMID: 28674175; PMCID: PMC6596706.

GENSAT, 2003, GENSAT, Cre Images for Neurotensin Receptor 1 (Ntsr1), Founder Line GN209, Rockefeller University, New York (2003) Available from http://www.gensat.org/creGeneView.jsp?founder_id=44880&gene_id=511&backcrossed=false

Gkogkas CG, Khoutorsky A, Cao R, Jafarnejad SM, Prager-Khoutorsky M, Giannakas N, Kaminari A, Fragkouli A, Nader K, Price TJ, Konicek BW, Graff JR, Tzinia AK, Lacaille JC, Sonenberg N. Pharmacogenetic inhibition of eIF4E-dependent Mmp9 mRNA translation reverses fragile X syndrome-like phenotypes. Cell Rep. 2014 Dec 11;9(5):1742-1755. doi: 10.1016/j.celrep.2014.10.064. Epub 2014 Nov 26. PMID: 25466251; PMCID: PMC4294557.

Glaser, E.M., Suter, C.M., Dasheiff, R. and Goldberg, A., 1976. The human frequency-following response: its behavior during continuous tone and tone burst stimulation. *Electroencephalography and Clinical Neurophysiology*, *40*(1), pp.25-32.

Gong S, Doughty M, Harbaugh CR, Cummins A, Hatten ME, Heintz N, Gerfen CR. Targeting Cre recombinase to specific neuron populations with bacterial artificial chromosome constructs. J Neurosci. 2007 Sep 12;27(37):9817-23. doi: 10.1523/JNEUROSCI.2707-07.2007. PMID: 17855595; PMCID: PMC6672645.

Harris KC, Wilson S, Eckert MA, Dubno JR. Human evoked cortical activity to silent gaps in noise: effects of age, attention, and cortical processing speed. Ear Hear. 2012 May-Jun;33(3):330-9. doi: 10.1097/AUD.0b013e31823fb585. PMID: 22374321; PMCID: PMC3340542.

Holley AJ, Shedd A, Boggs A, Lovelace J, Erickson C, Gross C, Jankovic M, Razak K, Huber K, Gibson JR. A sound-driven cortical phase-locking change in the Fmr1 KO mouse requires Fmr1 deletion in a subpopulation of brainstem neurons. Neurobiol Dis. 2022 Aug;170:105767. doi: 10.1016/j.nbd.2022.105767. Epub 2022 May 17. PMID: 35588990; PMCID: PMC9273231.

Kim T, Thankachan S, McKenna JT, McNally JM, Yang C, Choi JH, Chen L, Kocsis B, Deisseroth K, Strecker RE, Basheer R, Brown RE, McCarley RW. Cortically projecting basal forebrain parvalbumin neurons regulate cortical gamma band oscillations. Proc Natl Acad Sci U S A. 2015 Mar 17;112(11):3535-40. doi: 10.1073/pnas.1413625112. Epub 2015 Mar 2. Erratum in: Proc Natl Acad Sci U S A. 2015 May 26;112(21):E2848. PMID: 25733878; PMCID: PMC4371918.

Kokash J, Alderson EM, Reinhard SM, Crawford CA, Binder DK, Ethell IM, Razak KA. Genetic reduction of MMP-9 in the Fmr1 KO mouse partially rescues prepulse inhibition of acoustic startle response. Brain Res. 2019 Sep 15;1719:24-29. doi: 10.1016/j.brainres.2019.05.029. Epub 2019 May 22. PMID: 31128097; PMCID: PMC6640842.

Kraus, N., Anderson, S., White-Schwoch, T. (2017). The Frequency-Following Response: A Window into Human Communication. In: Kraus, N., Anderson, S., White-Schwoch, T., Fay, R., Popper, A. (eds) The Frequency-Following Response. Springer Handbook of Auditory Research, vol 61. Springer, Cham. https://doi.org/10.1007/978-3-319-47944-6_1

Krishnan, A., 2002. Human frequency-following responses: representation of steady-state synthetic vowels. *Hearing research*, *166*(1-2), pp.192-201.

Lisman JE. Bursts as a unit of neural information: making unreliable synapses reliable. Trends Neurosci. 1997 Jan;20(1):38-43. doi: 10.1016/S0166-2236(96)10070-9. PMID: 9004418.

Lovelace JW, Ethell IM, Binder DK, Razak KA. Translation-relevant EEG phenotypes in a mouse model of Fragile X Syndrome. Neurobiol Dis. 2018 Jul;115:39-48. doi:

10.1016/j.nbd.2018.03.012. Epub 2018 Mar 29. PMID: 29605426; PMCID: PMC5969806.

Lovelace JW, Rais M, Palacios AR, Shuai XS, Bishay S, Popa O, Pirbhoy PS, Binder DK, Nelson DL, Ethell IM, Razak KA. Deletion of Fmr1 from Forebrain Excitatory Neurons Triggers Abnormal Cellular, EEG, and Behavioral Phenotypes in the Auditory Cortex of a Mouse Model of Fragile X Syndrome. Cereb Cortex. 2020 Mar 14;30(3):969-988. doi: 10.1093/cercor/bhz141. PMID: 31364704; PMCID: PMC7132927.

Ma, X. and Suga, N., 2001a. Plasticity of bat's central auditory system evoked by focal electric stimulation of auditory and/or somatosensory cortices. *Journal of Neurophysiology*, *85*(3), pp.1078-1087.

Ma, X. and Suga, N., 2001b. Corticofugal modulation of duration-tuned neurons in the midbrain auditory nucleus in bats. *Proceedings of the National Academy of Sciences*, *98*(24), pp.14060-14065.

Nakamoto, K.T., Jones, S.J. and Palmer, A.R., 2008. Descending projections from auditory cortex modulate sensitivity in the midbrain to cues for spatial position. *Journal of Neurophysiology*, *99*(5), pp.2347-2356.

Nguyen AO, Binder DK, Ethell IM, Razak KA. Abnormal development of auditory responses in the inferior colliculus of a mouse model of Fragile X Syndrome. J Neurophysiol. 2020 Jun 1;123(6):2101-2121. doi: 10.1152/jn.00706.2019. Epub 2020 Apr 22. PMID: 32319849; PMCID: PMC7474255.

Rais, M., Binder, D. K., Razak, K. A., & Ethell, I. M. (2018). Sensory processing phenotypes in fragile X syndrome. *ASN neuro*, *10*, 1759091418801092.

Rais M, Lovelace JW, Shuai XS, Woodard W, Bishay S, Estrada L, Sharma AR, Nguy A, Kulinich A, Pirbhoy PS, Palacios AR, Nelson DL, Razak KA, Ethell IM. Functional consequences of postnatal interventions in a mouse model of Fragile X syndrome. Neurobiol Dis. 2022 Jan;162:105577. doi: 10.1016/j.nbd.2021.105577. Epub 2021 Dec 4. PMID: 34871737.

Razak, K.A., Binder, D.K. and Ethell, I.M., 2021. Neural correlates of auditory hypersensitivity in fragile X syndrome. *Frontiers in Psychiatry*, *12*, p.720752.

Rocha-Muniz, C. N., Befi-Lopes, D. M., & Schochat, E. (2012). Investigation of auditory processing disorder and language impairment using the speech-evoked auditory brain stem response. Hearing Research, 294, 143–152.

Rotschafer, Sarah E., and Khaleel A. Razak. "Auditory processing in fragile x syndrome." *Frontiers in cellular neuroscience* 8 (2014): 19.

Rumschlag JA, Razak KA. Age-related changes in event related potentials, steady state responses and temporal processing in the auditory cortex of mice with severe or mild hearing loss. Hear Res. 2021 Dec;412:108380. doi: 10.1016/j.heares.2021.108380. Epub 2021 Oct 23. PMID: 34758398.

Russo, N.M., Skoe, E., Trommer, B., Nicol, T., Zecker, S., Bradlow, A. and Kraus, N., 2008. Deficient brainstem encoding of pitch in children with autism spectrum disorders. *Clinical Neurophysiology*, *119*(8), pp.1720-1731.

Russo N, Nicol T, Trommer B, Zecker S, Kraus N. Brainstem transcription of speech is disrupted in children with autism spectrum disorders. Dev Sci. 2009 Jul;12(4):557-67. doi: 10.1111/j.1467-7687.2008.00790.x. PMID: 19635083; PMCID: PMC2718770.

Russo, N.M., Hornickel, J., Nicol, T., Zecker, S. and Kraus, N., 2010. Biological changes in auditory function following training in children with autism spectrum disorders. Behavioral and Brain Functions, 6, pp.1-8.

Seymour, Robert A., et al. "Reduced auditory steady state responses in autism spectrum disorder." *Molecular autism* 11 (2020): 1-13.

Sidhu H, Dansie LE, Hickmott PW, Ethell DW, Ethell IM. Genetic removal of matrix metalloproteinase 9 rescues the symptoms of fragile X syndrome in a mouse model. J Neurosci. 2014 Jul 23;34(30):9867-79. doi: 10.1523/JNEUROSCI.1162-14.2014. PMID: 25057190; PMCID: PMC4107404.

Smith, James C., James T. Marsh, and Warren S. Brown. "Far-field recorded frequency-following responses: evidence for the locus of brainstem sources." *Electroencephalography and clinical neurophysiology* 39.5 (1975): 465-472.

Suga N. Tuning shifts of the auditory system by corticocortical and corticofugal projections and conditioning. Neurosci Biobehav Rev. 2012 Feb;36(2):969-88. doi: 10.1016/j.neubiorev.2011.11.006. Epub 2011 Dec 2. PMID: 22155273; PMCID: PMC3265669.

Thuné, Hanna, Marc Recasens, and Peter J. Uhlhaas. "The 40-Hz auditory steady-state response in patients with schizophrenia: a meta-analysis." *JAMA psychiatry* 73.11 (2016): 1145-1153.

Tichko, P. and Skoe, E., 2017. Frequency-dependent fine structure in the frequency-following response: The byproduct of multiple generators. *Hearing research*, *348*, pp.1-15.

Van der Molen, M. J. W., Van der Molen, M. W., Ridderinkhof, K. R., Hamel, B. C. J., Curfs, L. M. G., & Ramakers, G. J. A. (2012). Auditory and visual cortical activity during selective attention in fragile X syndrome: a cascade of processing deficiencies. *Clinical Neurophysiology*, *123*(4), 720-729.

Weible AP, Moore AK, Liu C, DeBlander L, Wu H, Kentros C, Wehr M. Perceptual Gap Detection Is Mediated by Gap Termination Responses in Auditory Cortex. Current Biology (2014) 24(13):1447–1455.

Wen TH, Afroz S, Reinhard SM, Palacios AR, Tapia K, Binder DK, Razak KA, Ethell IM. Genetic Reduction of Matrix Metalloproteinase-9 Promotes Formation of Perineuronal Nets Around Parvalbumin-Expressing Interneurons and Normalizes Auditory Cortex Responses in Developing Fmr1 Knock-Out Mice. Cereb Cortex. 2018 Nov 1;28(11):3951-3964. doi: 10.1093/cercor/bhx258. PMID: 29040407; PMCID: PMC6188540.

White-Schwoch, T., Woodruff Carr, K., Thompson, E. C., Anderson, S., et al. (2015b). Auditory processing in noise: A preschool biomarker for literacy. PLoS Biology, 13(7), e1002196.

Yan, J. and Ehret, G., 2002. Corticofugal modulation of midbrain sound processing in the house mouse. *European Journal of Neuroscience*, *16*(1), pp.119-128.

Yan, J. and Zhang, Y., 2005. Sound-guided shaping of the receptive field in the mouse auditory cortex by basal forebrain activation. *European Journal of Neuroscience*, *21*(2), pp.563-576.

Zhou, X. and Jen, P.H.S., 2005. Corticofugal modulation of directional sensitivity in the midbrain of the big brown bat, Eptesicus fuscus. *Hearing research*, *203*(1-2), pp.201-215.

# Chapter 4: Combined Treatment with Minocycline and an mGluR5 Antagonist Improves Resting EEG Spectral Power, but not Sound-Evoked Responses, in a Mouse Model of Fragile X Syndrome

**Abstract**

Fragile X Syndrome (FXS) is a leading genetic cause of intellectual disability and autism-like behaviors. Glutamatergic mGluR5 receptors and matrix metalloproteinase-9 (MMP-9) have been suggested as potential therapeutic targets to treat symptoms. Here, we tested a novel approach to determine effects of combined treatment with an mGluR5 antagonist and minocycline, non-specific MMP-9 inhibitor, on electroencephalographic (EEG) phenotypes in a mouse model of FXS. EEG phenotypes are useful in studying autism spectrum disorders and FXS, as they provide objective physiological probes of sensory processing deficits that are remarkably similar in human patients and rodent models. Here, we tested if the phenotypes related to auditory hypersensitivity and temporal processing are reversed with the combined treatment affecting mGluR5 receptors and MMP-9. Adult male *Fmr1* knockout (KO) mice on the C57bl6/J background were given 10 days (oral gavage) of CTEP (mGluR5 antagonist) alone or in combination with minocycline. A 2x2 (genotype x treatment) design was used to compare with vehicle-treated KO and wild-type (WT) mice. Three types of group comparisons were made: 1) *Fmr1* WT pre-treatment vs. *Fmr1* KO pre-treatment to identify phenotypes, 2) WT-vehicle vs. *Fmr1* KO-drug to determine if the drugs normalized phenotypes to WT levels and 3) *Fmr1* KO-vehicle vs. *Fmr1* KO-drug to test for effects that are non-specific to the drug. Resting (no stimulus) and sound-evoked EEGs were recorded 1-day and 10-days after the start of treatments to test acute effects and potential tachyphylaxis. In pre-treatment WT and KO mice comparisons, we replicated previously published *Fmr1* KO mouse EEG phenotypes including elevated

power in the resting gamma band, single trial power, and reduced phase-locking to spectrotemporally dynamic auditory stimuli. Our data emphasize the replicability of the EEG phenotypes in different cohorts of mice and studies. CTEP treatment alone did not show any benefit compared to vehicle treatment in *Fmr1* KO mice after either 1 or 10 days of treatment. CTEP + minocycline reduced resting gamma band power in the *Fmr1* KO mice to a greater extent than vehicle at both treatment time points. There were no effects on sound evoked responses with the combined treatment. Taken together, these data suggest that combined treatment with CTEP and minocycline provides benefits for resting EEG spectral density measures while each treatment administered separately do not yield the same benefits. High power in broadband gamma frequency correlates with irritability, stereotyped behaviors, and hyperactivity in FXS patients, suggesting a combination of drugs reducing mGluR5 excitation and MMP-9 activity may be beneficial in FXS.

## 4.1 Introduction

Fragile X Syndrome (FXS) is a leading monogenic cause of developmental intellectual disability, affecting 1 in 4,000 males and 1 in 8,000 females (Warren & Nelson, 1994; Jin & Warren, 2000). FXS symptoms include learning, speech and language deficits, anxiety and hyperactive behavior (Warren & Nelson, 1994), and sensory hypersensitivity (Rais et al., 2018). FXS is the leading known genetic cause of autism spectrum disorder (ASD)-like behaviors (Crawford et al., 2001). FXS is caused by a mutated Fragile X messenger ribonucleoprotein 1 gene (*Fmr1*) on the X chromosome that is preceded by repeats of CGG trinucleotide segments. The neurotypical number of CGG repeats is between 6 and 50. An extensive number of copies of the CGG segment (>200 copies) is present in individuals with FXS, preventing expression of Fragile X messenger ribonucleoprotein (FMRP; Kremer et al., 1991; Yu et al., 1991; Verkerk et al., 1991; Oberle et al., 1991). FMRP regulates mRNA translation of various genes. With the loss of FMRP, there is abnormal protein synthesis, synapse development, altered excitatory/inhibitory synaptic balance, widespread increase in neuronal activity, and sensory deficits that are thought to underlie ASD-like phenotypes (Rais et al., 2018).

Sensory hypersensitivity is one of the most debilitating and consistent clinical symptoms in humans with FXS. Mechanistically, cortical hyper-excitability may lead to sensory hypersensitivity (Razak et al., 2021). Ethridge et al. (2019) revealed impaired habituation of the event-related potential (ERP) in response to noise bursts in adolescents and adults with FXS compared to typically-developing adults. There is elevated single

trial power and increased resting EEG power in the gamma band. In addition, compared to neurotypical participants, FXS participants have reduced phase-locking to temporally dynamic stimuli, particularly in gamma frequencies (Ethridge et al., 2019). Furthermore, high gamma power is present concurrently with reduced phase-locking to amplitude modulation of sounds at gamma frequencies, suggesting a low signal-to-noise ratio of cortical activity in the gamma range and potential heightening of excitation in the brain (Ethridge et al., 2019; Bhaskaran et al., 2023). These robust and repeatable EEG measures are correlated with clinical measures indicating relevance to daily functioning in humans with FXS. Clinical measures testing verbal and non-verbal ASD-like symptomology, such as the Social Communication Questionnaire (SCQ) scores and the ABC (including social communication and stereotyped behaviors), correlate with reduced habituation of the ERP and reduced phase-locking to chirp stimulus in FXS patients (Ethridge et al., 2019), although increased frontal gamma power in boys with FXS has been shown to correlate with better language abilities (Wilkinson & Nelson, 2021). In both males and females with FXS, increased theta power is present, and in males this phenotype correlates with better performance on the Auditory Attention speech-processing task (Smith et al., 2021).

The *Fmr1* knockout (KO) mouse model of FXS also shows cortical hyperexcitability and sensory hypersensitivity. Electrophysiological recordings from *Fmr1* KO mice in the auditory and frontal cortex (AC, FC) using similar paradigms as those used in humans show remarkably conserved phenotypes, including elevated gamma band power, reduced phase-locking to temporally modulated stimuli, reduced habituation

to repeated stimuli, and increased response magnitudes and total power (Rotschafer & Razak, 2013; Lovelace et al., 2016; 2018, Wen et al., 2018; 2019; Croom et al., 2023; reviewed in Razak et al., 2021). Enhanced cortical noise and reduced signal-to-noise ratio may underlie processing deficits and increased variability to temporally modulated stimuli (Rotschafer & Razak, 2013; Wen et al., 2018; Bhaskaran et al., 2023). There is currently no successful treatment for symptoms in FXS. The highly similar EEG phenotypes across species provide an avenue for objective and translationally-relevant outcome measures to test treatments and to elucidate underlying circuit dysregulation in FXS.

There are several cellular pathways affected by the loss of FMRP in FXS. Of these, the impact of elevated *m*etabotropic *Glu*tamatergic *R*eceptor subunit *5* (mGluR5) and Matrix Metalloproteinase-9 (MMP-9) pathways have received much attention. mGluR5 is classified as belonging to group I mGluRs, which are localized to dendritic spines (Lujan et al., 1997) and often act post-synaptically to promote neuronal excitation (Niswender & Conn, 2010). mGluRs facilitate long-term depression (LTD) or long-term potentiation (LTP), and hence play a major role in synaptic regulation and neuronal excitability (Niswender & Conn, 2010). The mGluR5 signaling pathway acts through phosphoinositide 3-kinase (PI3K) to promote a cascade involving Akt and mammalian target of rapamycin (mTOR) that ultimately leads to the transcription of genes relating to synaptic plasticity and synaptogenesis (Stoppel et al., 2017). Lack of FMRP expression results in unregulated protein synthesis downstream of mGluR5 (Dölen & Bear, 2008). mGluR5 is highly expressed in the forebrain (Bhakar et al., 2012), i.e., cortex,

hippocampus, and ventral striatum (Romano et al., 1995). Therefore, changes associated with the over-activation of mGluR5 signaling may be measured using cortical EEG to understand mechanisms of sensory abnormalities in FXS. A number of studies have targeted the mGluR5 pathway for potential treatment of FXS and have shown beneficial effects in preclinical studies (Yan et al., 2005; Dolen et al., 2007; Michalon et al., 2012). But whether EEG signals are affected by modulating mGluR5 is not known *Fmr1* KO mice.

MMP-9 is an endopeptidase that cleaves extracellular matrix (Ethell and Ethell, 2007) and its translation is negatively regulated by FMRP (Janusz et al., 2013). MMP-9 is elevated in multiple brain regions in humans with FXS and *Fmr1* KO mice (Sidhu et al., 2014, Gkogkas et al., 2014; Wen et al., 2018; Kokash et al., 2019). Genetic deletion of *Mmp-9* in *Fmr1* KO mice reverses some FXS-associated molecular, physiological, and behavioral deficits (Sidhu et al., 2014; Lovelace et al., 2016; Wen et al., 2018; Toledo et al., 2019). Pharmacological approaches to inhibit MMP-9 function with a non-specific inhibitor such as minocycline and more specific inhibitors such as SB-3CT show reduction of physiological and behavioral deficits in *Fmr1* KO mice (Rotschafer et al., 2012; Toledo et al., 2019; Lovelace et al., 2020; Pirbhoy et al., 2020). In humans as well, minocycline reduced deficits in sound evoked response habituation in FXS (Schneider et al., 2013; although no effects were found by Erickson et al., 2023).

Findings pointing to mGluR5 and MMP-9 dysfunction in FXS have led to two emerging theories in the field. The ‘mGluR5 theory’ suggests that neural symptoms in FXS can be linked to unregulated translation of genes downstream the mGluR5 pathway

(Bear et al., 2004; McBride et al., 2005; Yan et al., 2005; Chuang et al., 2005; Tucker et al., 2006; Dölen & Bear, 2008; Gkogkas et al., 2014). The 'MMP-9 theory' ties elevated MMP-9 activity in FXS to excessive cleavage of extracellular matrices called perineuronal nets (PNNs; Dziembowska et al., 2013; Sidhu et al., 2014; Reinhard et al., 2015; Wen et al., 2018; Pirbhoy et al., 2020; Dziembowska 2023; see Laroui et al., 2022 for clinical evidence). PNNs surround parvalbumin-positive GABAergic interneurons, and PNN cleavage leads to the reduced excitability of inhibitory neurons and ultimately disrupts inhibition levels in brain circuitry (Rankin-Gee et al., 2015; Balmer 2016). Furthermore, increased MMP-9 is associated with abnormal dendritic morphology and synaptic connections (Bilousova et al., 2009; Sidhu et al., 2014; Stawarski et al., 2014; Reinhard et al., 2015; Magnowska et al., 2016; Gore et al., 2021; reviewed in Dziembowska 2023). The translation of MMP-9 is promoted by a protein cascade downstream of mGluR5 activation (Gkogkas et al., 2014; Stoppel et al., 2017). mGluR5 activates Ras which in turn activates extracellular signal-regulated kinase (ERK), in turn activating mitogen-activated protein kinase interacting kinases (Mnk; Stoppel et al., 2017). Specifically, Mnk1 and Mnk2 phosphorylate eukaryotic Initiation Factor 4E (eIF4E), which regulates translation of MMP-9 mRNA (Stoppel et al., 2017). Pharmacological and genetic manipulations of MMP-9 activity via reduction of eIF4E phosphorylation (Gkogkas et al., 2014) or via Het models (Gkogkas et al., 2014; Lovelace et al., 2016) in the *Fmr1* KO mouse reveal improved spine morphology, cortical habituation to noise bursts based on the auditory ERP, and preference for social novelty and hyperexcitable behavior. Furthermore, mGluR-mediated LTD in hippocampal slices,

which is normally upregulated in the *Fmr1* KO mouse model compared to wild-type (WT), serves as a robust indication of synaptic dysregulation in the absence of FMRP (Huber et al., 2002). Reduction of MMP-9 activity via pharmacological or genetic means targeting eIF4E phosphorylation results in WT-level mGluR-LTD, suggesting a direct connection between MMP-9 and mGluR-mediated synaptic function (Gkogkas et al., 2014). These data therefore suggest that manipulating the cascade of proteins that connect mGluR5 activity to MMP-9 activity is an effective way to restore WT-like responses in *Fmr1* KO mice, suggesting a need to target multiple stages in the biochemical pathway.

Here we tested a novel combinatorial approach in which both the mGluR5 and the MMP-9 pathways were targeted simultaneously using CTEP, a negative allosteric modulator (NAM) of mGluR5, and minocycline, which inhibits MMP-9 activity. We recorded EEG phenotypes from the AC and FC of *Fmr1* KO mice before and after 1 day and 10 days of treatment. The longer treatment allows some time for potential circuit remodeling, as well as tests for any buildup of drug tolerance. The outcome measures we chose in this study were EEG phenotypes that are similar in rodents and humans. Indeed, previous studies have shown that MMP-9 reduction or inhibition can modify EEG phenotypes (Lovelace et al., 2016; Wen et al., 2018). Whether mGluR5 antagonists can improve *in vivo* EEG responses, and whether mGluR5 modulation combined with reduced MMP-9 signaling (CTEP + minocycline) can modify EEG responses, is unknown. These questions were addressed in this study, with the specific hypothesis that

EEG phenotypes recorded from AC and FC would be reduced in *Fmr1* KO mice to a greater extent with CTEP + minocycline than with CTEP alone.

## 4.2 Materials and Methods

### *4.2.1 Mice*

We tested male *Fmr1* KO and WT littermate mice on the C57bl6/J background strain (B6.129P2-Fmr1tm1Cgr/J, stock #003025) at postnatal age P60-P100. Mice were obtained by breeding WT male and *fmr1*$^{+/-}$ female mice in an in-house breeding colony that originated from Jackson Laboratory (Bar Harbor, ME). Pups were weaned at P21 and group-housed (2-4 mice per cage) until surgery. All procedures were approved by the Institutional Animal Care and Use Committee at the University of California, Riverside. Mice were maintained in an AAALAC accredited facility in 12 h light/dark cycles and fed standard mouse chow. Food and water were provided *ad libitum*. Standard tail snip was performed on mice for genotyping (Transnetyx). Experimenters were blind to genotype. The study used a total of 25 KO and 39 WT littermates.

### *4.2.2 Overview of Experimental Procedures*

All experiments were conducted on adult male C57BL/6 mice. After surgical implantation of electrodes, mice were given 4-5 full days of recovery before EEG experiments. The AC and FC were recorded using epidural screw electrodes, with occipital lobe as reference. All mice were recorded on all EEG protocols pre-drug administration. A total of 25 *Fmr1* KO mice and 39 WT mice were tested in the "pre" groups before any drug administration. The mice then received either CTEP, CTEP +

minocycline, or vehicle solution through oral gavage daily for 10 days followed by "post" EEG tests. Experiment timeline is presented in **Figure 1**, and sample sizes are as indicated in **Table 1**.

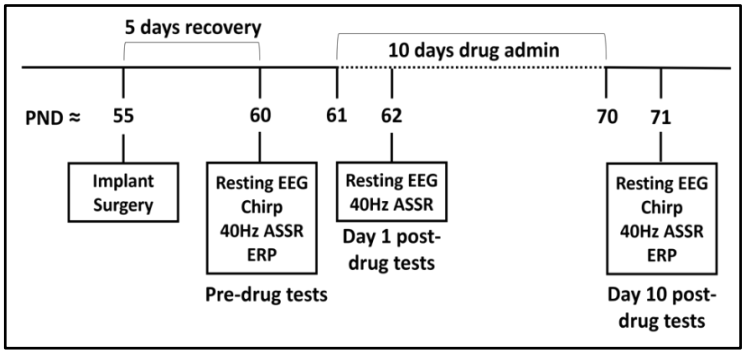


*Figure 4.1. Detailed timeline of experimental procedures* PND – postnatal day; ASSR – auditory steady state responses; ERP – event related potential, which was used to generate STP – single trial power. Ages shown are a stereotypical example of mouse treatment and experiment schedule. Mouse age varied from P60-100 at the start of the experiment.

| Genotypes (littermates) | Treatments | n |
|---|---|---|
| Fmr1-knock out (KO) | CTEP | 9 |
| | CTEP + Minocycline | 8 |
| | Vehicle | 8 |
| Wild-type (WT) | CTEP | 12 |
| | CTEP + Minocycline | 18 |
| | Vehicle | 9 |

*Table 4.1.* Sample sizes for each experimental group (genotype/treatment).

*4.2.3 EEG surgeries*

Mice were anesthetized for the entire duration of the surgery through i.p. injections of 120 μg/g of ketamine and 5 μg/g of xylazine. The anesthetic state of mice was monitored using the toe-pinch reflex tested every 10-15 minutes. Surgery commenced only when the mouse did not react (withdrawal reflex) to this procedure. Supplemental doses of ketamine (0.25mg/g body weight) were further administered, if

required. Each mouse was placed into a standard rodent stereotaxic frame (model 930; Kopf, CA, United States). Body temperature was monitored and maintained around 37° C using a rectal thermometer linked to a DC temperature controller system connected to a heating pad (FHC Inc). An ophthalmic ointment was administered to keep eyes moist throughout the procedure. A cosmetic hair remover (Nair) was applied on the head to clear hair and the skin was sterilized using alcohol wipes and gentle application of betadine. An incision was made in the skin for skull exposure. 0.9% saline was applied to the skull intermittently to clean the skull and maintain moisture. Three 1mm-diameter holes were drilled (Foredom dental drill) through the skull, exposing the right AC (-1.6mm caudal, +4.3-4.8mm lateral to bregma), the right FC (+3.0 mm rostral, +1.6 mm lateral to bregma) and the left occipital lobe (−4.8 mm caudal, −2.95 mm lateral). Screw electrodes (Plastics One, 00-96 X1/16) connected to a three-channel headpost (Plastics One, MS333-2-A-SPC) were implanted epidurally in the right AC and in the FC for EEG recording and in the occipital lobe for reference. The screws were advanced into the skull holes until secure and to the point of contact with the dura. Dental cement was applied onto the exposed skull and around the incision site to additionally secure the screws to the skull, sealing the surgical site completely.

*4.2.4 Recovery*

Antibiotic ointment was applied around the surgical site. Body temperature was monitored until mice showed signs of waking. Upon waking, mice were administered with buprenorphine, a potent analgesic (0.1 mg/kg body weight), subcutaneously. Mice were placed, singly housed, in a new cage on top of a heat pad (Sunbeam) until fully

awake and moving around. They were closely monitored for 48 hours, with buprenorphine administered subcutaneously approximately every 8 hours. Mice were allowed 4-5 days of recovery.

*4.2.5 Drug administration*

KO and WT littermates received one of the following treatments over the course of 10 days: CTEP (2mg/kg per 48 hrs), CTEP (1mg/kg per 48 hrs) + minocycline (15mg/kg per day), or vehicle (veh; 0.9% NaCl saline + 0.8% Tween-80). All treatments were delivered via oral gavage. All mice were orally gavaged daily throughout the 10-day timeline of the experiment to control for the gavage procedure across treatment regimens (see **Figure 1** for the detailed timeline). To the groups receiving CTEP alone, CTEP was delivered once every 48 hrs, and vehicle was delivered on the days in between CTEP administration such that mice were orally gavaged daily. The groups that received CTEP + minocycline were given CTEP every 48 hrs and minocycline every 24 hrs, resulting in alternating CTEP + minocycline and only minocycline administrations across the 10 days of treatment. Previously, we published the effects of minocycline treatment (30mg/kg every 24 hrs) on EEG markers in *Fmr1* KO mice (Lovelace et al., 2020). Administration doses and regimens were based on previous studies that tested dose and efficacy of each drug (Bilousova et al., 2009 for minocycline; Lindemann et al., 2011 for CTEP), as CTEP efficacy lasts longer than minocycline (48 hrs versus 24 hrs). We chose to use half dose of each drug in the combined treatment (1mg/kg CTEP and 15mg/kg minocycline) to achieve a synergistic effect. Vehicle alone was administered on each day to control groups.

*4.2.6 Drug preparation*

Drug solutions were prepared similarly to what was previously described (Lovelace et al., 2020). Drug solutions were prepared using a vehicle of 0.9% NaCl + 0.8% Tween-80, targeting an administration volume of 6 mL/kg and a target concentration of 2 mg/kg of CTEP for the CTEP treatment and 1 mg/kg of CTEP and 15 mg/kg of minocycline for the CTEP + minocycline treatment. Stock solutions of CTEP (Sigma) and minocycline (MP Biomedicals) were prepared regularly and kept frozen until time of use, when they were thawed, sonicated, vortexed, and then administered. All drugs and vehicle control solutions were administered through a stainless steel curved oral gavage tip (Cadence Science, product #7910). After each use, gavage tips were soaked in ethanol, rinsed with distilled water, and autoclaved before being used again.

*EEG.* The EEG recording and analysis methods described here followed previously published methods (Lovelace et al., 2018; 2020; Rumschlag et al., 2021). Briefly, awake and freely moving mice were placed in an arena surrounded by a custom-built Faraday cage inside a sound-insulated booth (GretchKen Industries, Oregon). They were attached to an EEG cable (Plastics One, 335-SL/3) via the implanted headpost for recording. To determine if movement was a factor in creating genotype differences in power spectral density, a piezoelectric transducer was placed underneath the recording cage to detect when a mouse was moving during EEG recordings. Percent time spent moving was analyzed as a covariate in the experimental design.

Signals were recorded with filters set to high-pass (>0.5 Hz) and low-pass (<100 Hz). The gain was maintained the same (10,000×) between all recordings. Data were

sampled at 2.5 kHz (Acqknowledge software) and down sampled to 1024 Hz post hoc using Analyzer 2.2 (Brain Vision Inc). TTL pulses were used to synchronize stimulus onset in each train with EEG recording. Following 10 minutes of habituation in the arena, resting EEG was recorded (5 minutes) during which no sounds were presented. Following resting EEG, ERP recordings in response to trains of broadband noise, chirps and ASSR were recorded.

*4.2.7 Acoustic stimulation*

Sound stimuli were generated using RPvdsEx software and RZ6 hardware (Tucker Davis Technologies, FL, United States) and presented through a free-field speaker (MF1, Tucker-Davis Technologies, FL, United States) situated 20 cm above the floor of the arena. The speaker output was ~70 dB SPL at the floor of the arena. Broadband noise stimulus (BBN, bandwidth 1-12 kHz, 100 ms in duration, 5 ms rise/fall time) was presented at 70 dB SPL. BBN was presented in trains of 10 noise bursts at a repetition rate of 1 or 2 Hz, with a total of 100 trains per repetition rate. The interval between each stimulus train was 8 s. Auditory steady state response (ASSR) was recorded using clicks presented at a rate of 40 Hz. Each click train lasted 1 s in duration; there were 200 repetitions of the click train. Mice were presented with a broadband noise stimulus that was amplitude-modulated with increasing frequency (1-100 Hz; upsweep chirp). Each presentation lasted 2 s in duration. There were 300 repetitions of the chirp stimulus. EEG signal acquisition was done as previously described by Lovelace et al. (2020) using the BioPac system (BIOPAC Systems, Inc).

*4.2.8 EEG analysis*

Resting EEG data were divided into 2 s segments, and each segment was subjected to Fast Fourier Transforms (FFT) analysis using a 10% Hanning window at 0.5 Hz bin resolution. The average power density ($\mu V^2$/Hz) was calculated for each mouse from 1 to 100 Hz. Power was binned according to spectral bands: theta (4– 8 Hz), alpha (8–13 Hz), beta (13–30 Hz), low gamma (30– 55 Hz), and high gamma (65–100 Hz). Chirp, ASSR, and ERP traces were processed using Morlet wavelets linearly spaced from 1 to 100 Hz using voltage (μV). Wavelet coefficients were exported as complex values for use with Inter Trial Phase Coherence (ITPC) analysis. Wavelets were run with a Morlet parameter of 10. To measure phase synchronization at each frequency across trials, ITPC was calculated as previously described (Lovelace et al., 2020). We measured baseline-corrected single trial power (STP) for ERP analysis. Real values of spectral power ($\mu V^2$) were derived from Morlet wavelets. Baseline correction was done by taking the average power from −250 ms through −150 ms of the ERP window for each frequency layer and directly subtracting that average power from all values for their respective frequency layer in the window on a trial-by-trial basis. After baseline was corrected for each trial, the trials were averaged together.

*4.2.9 Statistical analysis*

Data analysis was done similarly to Lovelace et al. (2020). Briefly, statistical group comparisons of ITPC and baseline-corrected STP for the various stimulation paradigms were quantified using a Monte Carlo permutation approach. The details of the analysis are as described by Lovelace et al. (2018, 2020). Time-frequency analysis was

conducted by binning time into 256 parts and frequency into 100 parts, resulting in a 100 × 256 matrix. Non-parametric analysis was used to determine contiguous regions in the matrix that were significantly different from a distribution of 2000 randomized Monte Carlo permutations based on previously published methods (Maris and Oostenveld, 2007). If the cluster sizes of the real genotype assignments (both positive and negative direction, resulting in a two-tailed alpha of $p = 0.025$) were larger than 97.25% of the random group assignments, those clusters were considered significantly different between experimental conditions.

The differences between experimental conditions in resting power were analyzed using one-way MANCOVA with movement as the covariate. Specifically, the movement was the proportion of time spent moving during the 5 min recording session. This was done to identify genotype effects and control for potential effects of hyperactivity on cortical responses. Genotype and drug treatment were the independent variables, and the dependent variables were 5 frequency bins from theta to high gamma. This resulted in a 2 × 2 design: genotype (WT or *Fmr1* KO) × drug treatment (CTEP, CTEP + minocycline, or vehicle). Genotype comparisons were corrected for multiple comparisons using Bonferroni adjustments by using an effective $\alpha = 0.01$ to account for five frequency bands.

## 4.3 Results

### *4.3.1 Relevant experimental group comparisons*

The following group comparisons of EEG outcomes were made to determine the effects of a treatment:

a) *Fmr1* WT vs *Fmr1* KO mice pre-treatment condition – this comparison was made to identify EEG phenotypes in KO mice before any drug administration.
b) *Fmr1* KO-drug vs WT-vehicle – this comparison was made to determine if the drug treatment, isolated from any other effects, actually produces therapeutic results to the *Fmr1* KO mice.
c) *Fmr1* KO-drug vs *Fmr1* KO-vehicle – this comparison was made to identify drug effects on EEG of *Fmr1* KO mice.

### *4.3.2 EEG phenotypes in Fmr1 KO mice in the pre-treatment condition*

We have previously reported a number of EEG phenotypes in the *Fmr1* KO mice that are similar to those observed in humans with FXS. This includes elevated resting EEG gamma band power, reduced phase-locking to spectrotemporally dynamic stimuli and higher single-trial power (STP). The previous mouse studies tested male mice born to homozygous breeding pairs and were not littermates. Comparison of WT and *Fmr1* KO littermate mice used in the pre-drug condition of the present study (n=25 KO and 39 WT mice) replicated the mouse EEG phenotypes in this larger sample (**Figure 2**). **Figure 2A, B** show the average spectral power density across canonical frequency bands in the AC and FC, respectively, in the pre-drug condition. The ordinate axis of panels

(A) and (B) shows absolute power as a ratio of KO:WT mice, with '1' indicating equal power, and a value greater (lower) than '1' indicating higher (lower) power in the KO mice. While there was little genotype difference in the theta, alpha and beta bands, there was a clear elevation in the gamma band (40-100 Hz) in both cortical regions. The difference was seen in both low (40-60 Hz) and high (60-100 Hz) gamma power (AC, low gamma: $p<.001$; AC, high gamma: $p=.004$; FC, low gamma: $p=.004$; FC, high gamma: $p=.005$). MANCOVA was performed (genotype x frequency with percentage of time spent in movement as covariate) and Bonferroni correction was used for multiple comparisons ($*p < 0.01$). **Figure 2C, D** show the difference in STP (KO-WT) in the AC and FC, respectively. Higher power in the KO mice is represented by warmer colors. The STP in each mouse was analyzed from the EEGs recorded during the presentation of 100 ms noise bursts (1 Hz repetition rate; 2 Hz repetition rate data not shown as outcomes were similar). STP, a measure of total power, also showed elevated gamma (~40-100 Hz; shown as dashed or solid line contours in the panels) power in the *Fmr1* KO mice compared to WT in both cortical regions, consistent with abnormalities in cortical circuits that generate gamma spectral power in FXS. Dotted line contours in **Figure 2C, D** delineate clusters of significant differences in the KO vs WT comparisons: dashed lines indicate significantly higher power in the KO compared to WT, and solid lines indicate significantly lower power in the KO compared to WT. A third robust and replicable phenotype in *Fmr1* KO mice and humans with FXS is the reduced ability of the cortex to produce consistently phase-locked responses across trials when presented with a steady auditory stimulus such as a relatively long (1 sec) 40 Hz click train stimulus or a dynamic

auditory stimulus such as the chirp. The 40 Hz auditory steady state response (ASSR) is a commonly used stimulus paradigm to identify temporal processing abnormalities. The consistency of responses across trials is measured using the intertrial phase coherence (ITPC), which is typically lower in the *Fmr1* KO mice. **Figure 2E, F** show that the phase-locking in the 40 Hz ASSR as measured using ITPC was reduced at the onset of the stimulus in the AC and throughout the stimulus presentation in the FC. The FC showed continuous reduction in the KO mice across the stimulus duration, while the AC showed a reduction at the onset of the stimulus. The chirp is a sound in which a 2 sec long noise stimulus is amplitude-modulated with increasing frequency of modulation over time (upward modulated chirp). As reported previously, we observed a reduction of ITPC to the chirp in both the AC and the FC (**Figure 2G, H**). Different bands of frequencies were affected in the AC (~10-30 Hz) and FC (15, 60-100 Hz; shown as dashed or solid line contours in the panels), but the major effect was that ITPC in the KO mice was significantly reduced compared to WT. Taken together, we replicated the major EEG phenotypes reported in *Fmr1* KO mice that can be used to test the effects of the CTEP and CTEP + minocycline treatments. This indicates the consistency and robustness of EEG phenotypes across studies, cohorts of mice and parental genotypes.

*4.3.3 Effects of 1-day CTEP treatment on EEG responses*

The effects of CTEP treatment on EEG responses and the possibility of tachyphylaxis from continued administration of the drug was examined by recording EEG 1-day and 10-day after CTEP treatment onset in the same mice. While the full EEG data set (resting, STP, ASSR and chirp) was collected at 10-day post treatment onset,

only the resting EEG and ASSR data were collected on 1-day post-treatment. The sample size for 1-day post CTEP recordings is: 9 *Fmr1* KO with CTEP, 8 *Fmr1* KO with vehicle, 9 WT with vehicle and 12 WT with CTEP (data from WT treated with CTEP is not shown).

**Figure 3** shows EEG responses after 1 day of CTEP treatment. In the AC, there was no effect of CTEP on elevated gamma power (**Figure 3A**; AC, low gamma: p=.003). Resting power in the AC of *Fmr1* KO mice was similar with CTEP or vehicle (**Figure 3C**; all p>.01), indicating no effect of treatment. In the FC, CTEP treatment reduced gamma power to WT-vehicle level (**Figure 3B**; all p>.01), however, because there was no difference between KO-drug and KO-vehicle (**Figure 3D**; all p>.01), we interpret this to indicate a handling effect of the experimental procedure and likely the oral gavage, and not a specific drug outcome. None of the other frequency bands showed any significant effects of treatment or vehicle (all p>.01). MANCOVA was performed (genotype or treatment x frequency band, with movement as covariate) and Bonferroni correction was made for multiple comparisons (*p < 0.01).

CTEP-treated KO mice did not show improved sound-driven phase-locking in the 40 Hz ASSR (**Figure 3E-H**). In the AC (**Figure 3E, G**), while ITPC increased in the CTEP-treated KO mice compared to vehicle-treated WT mice (**Figure 3E**; dashed-line cluster around 40 Hz), the treatment outcome in the KO mice was similar for drug and vehicle (**Figure 3G**; no clusters around 40 Hz). The outcome was essentially similar in the FC (**Figure 3F, H**). Taken together, these data show that 1-day CTEP treatment did not have specific effects on resting EEG power or sound-driven phase-locking.

Differences seen in resting and evoked power were likely due to the experimental procedure, as vehicle conditions were not significantly different from drug treatment.

*4.3.4 Effects of 10 days of CTEP treatment on EEG responses*

The sample size for 10-day post-CTEP recordings was: 9 *Fmr1* KO with CTEP, 8 *Fmr1* KO with vehicle, 9 WT with vehicle and 12 WT with CTEP (WT-CTEP data is not shown). CTEP treatment over 10 days had no significant effect on resting or sound driven EEG responses in KO mice (**Figure 4**). In the AC, 10-day CTEP-treated mice continued to show increased gamma band power compared to WT-vehicle (**Figure 4A**; AC, low gamma: $p<.001$; AC, high gamma: $p<.001$) and compared to KO-vehicle (**Figure 4C**; AC, theta: $p=.004$; AC, high gamma: $p<.001$). In the FC, CTEP treatment reduced gamma power to WT-vehicle level (**Figure 4B**; $p>.01$). However, CTEP-treated KO mice showed increased gamma power compared to vehicle-treated KO mice (**Figure 4D**; FC, high gamma: $p=.003$). CTEP treatment increased low-frequency power (theta, alpha) in the FC of KO mice (**Figure 4B**; FC, theta $p=.007$; FC, alpha $p=.004$). The elevated theta power in the KO-CTEP mice when compared to WT-vehicle is also present when compared to KO-vehicle (**Figure 4D**; FC, theta: $p=.005$), indicating a true drug effect. MANCOVA was performed (genotype or treatment x frequency, with movement as covariate) and Bonferroni correction was made for multiple comparisons ($*p < 0.01$).

*Fmr1* KO mice with 10 days of CTEP treatment continued to show elevated STP during sound stimulation compared to vehicle-treated WT mice. STP during the presentation of 100 ms noise bursts showed elevated power in the *Fmr1* KO treated with

CTEP across all frequencies in the AC (**Figure 4E**) and FC (**Figure 4G**) compared to WT-vehicle, including in low frequencies (~1-40 Hz) which were not present in the pre-treatment comparisons (**Figure 2**). Compared to vehicle, treatment with CTEP in the KO mice increased STP in the AC (**Figure 4F**; all frequencies) and did not significantly change STP in the FC (**Figure 4H**; clusters were found only around 0-10 Hz). These data suggest that CTEP, compared to vehicle, increases power to levels higher than the genetic mutation without treatment.

CTEP administration to *Fmr1* KO mice over 10 days did not improve their ITPC to ASSR stimulus or to chirp. ITPC to ASSR stimulus in CTEP-treated KO mice was similar to WT in the FC (**Figure 4K**; no significant clusters around 40 Hz) but remained lower than WT in the AC (**Figure 4I**; cluster indicating lower ITPC at 40 Hz in the KO compared to WT at the stimulus onset). In the FC, there was reduced ITPC in the KO group compared to WT group at the 80 Hz harmonic and higher ITPC at frequencies lower than 40 Hz (**Figure 4K**; cluster around 80 Hz harmonic indicating lower ITPC in the KO compared to WT; one cluster around 10-35 Hz indicating higher ITPC in the KO group compared to WT). Treatment of KO mice with CTEP resulted in similar ITPC levels as vehicle treatment in both cortical regions, suggesting no treatment effect (**Figure 4J, L**; no significant clusters). Likewise, ITPC to the chirp stimulus in the CTEP-treated *Fmr1* KO mice remained lower than WT-vehicle in the AC (**Figure 4M**; clusters around the chirp indicate lower ITPC in the KO group compared to WT group around ~1-20 Hz and ~60-80 Hz amplitude modulation) but showed similar ITPC in the FC (**Figure 4N**; no significant clusters around the chirp stimulus). However, CTEP

treatment in KO mice resulted in lower ITPC compared to vehicle treatment in the AC (**Figure 4O**; clusters around ~15 Hz and ~60-80 Hz of the chirp stimulus indicating lower ITPC in the KO-ctep group compared to KO-veh group) and was not different in the FC (**Figure 4P**; no significant clusters around the chirp stimulus). Taken together, we interpret these data to mean that 1- or 10-day CTEP treatment had no major effect on EEG phenotypes in the *Fmr1* KO mice.

*4.3.5 Effects of 1-day combined CTEP + minocycline treatment on EEG responses*

The sample size for the combined treatment measured 1-day post treatment onset was: 8 *Fmr1* KO with CTEP + minocycline, 9 WT with vehicle, 8 *Fmr1* KO with vehicle and 18 WT with CTEP + minocycline (data from WT mice with combined treatment is not shown). When CTEP and minocycline were given in combination for 1 day, resting EEG gamma power was similar in the *Fmr1* KO mice compared to WT-vehicle in the AC (**Figure 5A**; $p>.01$) and restored power in the high gamma band, but not in the low gamma band, in the FC (**Figure 5B**; FC, low gamma: $p=.01$; FC, high gamma: $p>.01$), suggesting that drug treatment reduced KO gamma power to WT levels only in the AC. Comparison of drug-treated KO mice with vehicle-treated KO mice showed a significant reduction in high/low gamma power in the AC/FC in the drug condition, indicating a specific effect of the drug treatment (**Figure 5C, D**; AC, high gamma: $p=.002$; FC, low gamma: $p=.003$). MANCOVA was performed (genotype or treatment x frequency with movement as covariate) and Bonferroni correction was made for multiple comparisons ($*p < 0.01$).

ITPC in response to a 40 Hz click train (ASSR) was elevated in the AC of KO mice treated with CTEP + minocycline compared to WT treated with vehicle 1-day post-treatment onset (**Figure 5E**; dashed clusters around 40 Hz ASSR indicating higher ITPC in the KO compared to WT). ITPC in the FC was similar between drug-treated KO and WT-vehicle (**Figure 5F**; no significant clusters around 40 Hz). However, ITPC in response to a 40 Hz click train (ASSR) was similar between drug-treated KO and KO-vehicle in the AC (**Figure 5G**; no significant clusters around 40 Hz) and FC (**Figure 5H**; no significant clusters around 40 Hz), indicating that no specific drug effect was present following 1 day of treatment on phase-locking in the ASSR.

Taken together, resting EEG gamma power in the *Fmr1* KO mice was improved following 1 day of combined treatment (CTEP + minocycline). Specifically, there was normalization of high gamma power in the AC and low gamma power in the FC. This combined treatment induced no specific change in ASSR phase-locking.

*4.3.6 Effects of 10 days of combined CTEP + minocycline treatment on EEG responses*

The sample size for the combined treatment measured 10 days post-treatment onset was: n = 8 KO with CTEP + minocycline, 9 WT with vehicle, 8 KO with vehicle, 18 WT with CTEP + minocycline (data not shown). Like the 1-day treatment, the 10-day treatment with CTEP + minocycline restored gamma levels in the AC and FC in *Fmr1* KO mice compared to WT-vehicle, while not affecting sound-driven measures of STP and ITPC (**Figure 6**). *Fmr1* KO mice treated with CTEP + minocycline showed similar resting EEG gamma power in the AC (**Figure 6A**; $p>.01$) and FC (**Figure 6B**; $p>.01$) compared to WT-vehicle. Compared to vehicle treatment, CTEP + minocycline

treatment in the *Fmr1* KO mice significantly lowered gamma power in the AC (**Figure 6C**; AC, low gamma: p=.002; AC, high gamma: p<.001) and reduced low gamma power in the FC (**Figure 6D**; FC, low gamma: p=.006), suggesting a specific treatment effect restoring gamma power to WT levels. Additionally, theta and alpha power were reduced in the AC (**Figure 6C**; AC, theta: p=.003; AC, alpha: p=.002) and alpha power was reduced in the FC (**Figure 6D**; FC, alpha: p<.001) in the treatment group compared to vehicle. MANCOVA was performed (genotype or treatment x frequency with movement as covariate) and Bonferroni correction was made for multiple comparisons (*p < 0.01).

Day 10 post-treatment onset with CTEP + minocycline in the *Fmr1* KO mice did not reduce STP gamma power in the *Fmr1* KO mice compared to WT-vehicle (**Figure 6E-H**). STP during the presentation of 100 ms noise bursts shows elevated power in the *Fmr1* KO treated with CTEP + minocycline across gamma frequencies in the AC (**Figure 6E**; ~40-90 Hz) and FC (**Figure 6G**; ~40-100 Hz) compared to WT-vehicle. In the KO mice, compared to vehicle, treatment with CTEP + minocycline for 10 days did not reduce STP in the AC (**Figure 6F**; no significant clusters) and increased STP in the gamma range in the FC (**Figure 6H**; ~50-100 Hz). Phase-locking to the 40 Hz click train (ASSR) or to chirp as measured using ITPC in the CTEP + minocycline-treated KO mice was not improved (**Figure 6I-L**, **Figure 6M-P**). ITPC to the ASSR stimulus in CTEP + minocycline-treated *Fmr1* KO mice was reduced compared to WT-vehicle in the AC (**Figure 6I**; significant cluster around 40 Hz) and similar to WT-vehicle in the FC (**Figure 6K**; no clusters around 40 Hz). In the KO mice, treatment with CTEP + minocycline resulted in higher ITPC at the onset of the 40 Hz click stimulus and lower

ITPC levels throughout the duration of the stimulus in the AC compared to vehicle (**Figure 6J**; cluster at stimulus onset indicating higher ITPC in the treatment group around 40 Hz, followed by clusters around 40 Hz indicating lower ITPC in the treatment group) compared to vehicle and similar ITPC levels as vehicle in the FC (**Figure 6L**; no clusters around 40 Hz), indicating no specific treatment effect on phase-locking in the 40 Hz ASSR.

ITPC to the chirp stimulus in the *Fmr1* KO mice treated with CTEP + minocycline was similar to WT-vehicle levels in the AC (**Figure 6M**; no significant clusters) and lower in the FC (**Figure 6N**; cluster in the ~50-70 Hz amplitude modulation range indicating lower ITPC in the KO group). However, CTEP + minocycline treatment in KO mice resulted in lower ITPC compared to vehicle treatment in the AC (**Figure 6O**; cluster in the ~70-100 Hz amplitude modulation range indicating lower ITPC in the treatment group) and FC (**Figure 6P**; cluster at ~60 Hz amplitude modulation indicating lower ITPC in the treatment group). These results indicate no improvement by treatment in the FC and an effect in the AC that is not improved by treatment compared to vehicle. In summary, 1- or 10-day CTEP + minocycline treatment restored gamma power in resting EEG of *Fmr1* KO mice to WT levels but had no major effect on sound-evoked EEG phenotypes in the *Fmr1* KO mice.

The results show essentially no effect of CTEP alone on EEG outcomes compared to vehicle, either at 1- or 10-days following treatment, but CTEP + minocycline reduces resting EEG gamma band power at both treatment time points. There were no effects of treatments on any of the sound evoked measures in this study.

## 4.4 Discussion

The main goal of this study was to test a combination of drugs that targets two major pathways affected in FXS, mGluR5 and MMP-9. We used CTEP as an antagonist of mGluR5 activity either alone or in combination with an MMP-9 inhibitor, minocycline, in male littermate *Fmr1* KO and WT mice to test whether EEG phenotypes are rescued in the *Fmr1* KO mice. We recorded EEGs at two time points after treatment, which we refer to as acute (1-day post treatment onset) and chronic (10-day post treatment onset). The major findings can be summarized as: 1) Previously- reported EEG phenotypes in *Fmr1* KO mice tested in non-littermates are present in littermates. Specifically, resting gamma power and STP are elevated in the AC and FC. Additionally, there is a deficit in ITPC of the ASSR in the FC but not in the AC that is similar to what is previously reported in non-littermate comparisons of *Fmr1*-KO mouse models of FXS (Lovelace et al., 2020). ITPC deficits are also present in the chirp response, but the frequency bands affected in this study are different than previously reported in non-littermate studies (ITPC to 5-30 Hz and 70-80 Hz is significantly reduced and increased, respectively, in this study; vs. ITPC to 10-50 Hz and 60-100 Hz is significantly reduced in Lovelace et al., 2018). 2) CTEP treatment by itself showed no improvement compared to vehicle for either 1-day or 10-day post treatment onset, and in some instances (e.g., STP measure) resulted in an exaggerated phenotype compared to vehicle. 3) CTEP + minocycline treatment restored gamma power levels to WT that is significantly different from vehicle on both 1- and 10-day. There were no effects on sound-evoked responses. The implications of these findings are discussed below.

*4.4.1 Mouse EEG recordings reveal robust, replicable and translation-relevant phenotypes*

In a number of previous studies in *Fmr1* KO mice and in humans with FXS, remarkably similar EEG phenotypes have been reported compared to control counterparts. These phenotypes are seen across strains of mice, in the rat model of FXS, and in *in vitro* slice preparations suggesting a highly reliable and translation-relevant set of outcome measures to test the impact of drug treatments across species (reviewed in Razak et al., 2021). The phenotypes reported in mice and humans include: (1) increased gamma power in resting EEG (Wang et al., 2017; Lovelace et al., 2018; Jonak et al., 2020); (2) reduced phase-locking to spectrotemporally-modulated sound signals such as chirps (Ethridge et al., 2019; Lovelace et al., 2018; Jonak et al., 2020); and (3) increased amplitude of ERPs and STP to auditory stimuli (Knoth and Lippe 2012; Van der Molen et al., 2012; Ethridge et al., 2017; Wen et al., 2019). The previous mouse work utilized litters of homozygous *Fmr1* KO and WT breeding pairs. However, given that FXS is a neurodevelopmental disorder and that having affected siblings and carrier Het mothers may influence development of WT pups, it was first important to replicate EEG phenotypes in littermate WT/*Fmr1* KO mice. Indeed, the pre-treatment results from the current study replicates EEG findings previously reported in mice (**Figure 2**). *Fmr1* KO mice show increased resting gamma power, increased STP to noise bursts, and reduced ITPC to amplitude-modulated signals (ASSR and chirp) compared to WT mice. This approach better isolates the genetic impact of the loss of FMRP expression on EEG measures compared to non-littermate comparisons. Although the frequencies in the chirp

stimulus that are impacted in the littermate comparisons are slightly different from non-littermate comparisons, the deficit in ITPC to amplitude-modulated signals is persistent across experimental design. Across species, these data show that cortical function in FXS is likely impacted by a milieu of increased total power (elevated STP), variability in response timing across trials (reduced phase locking factor), reduced habituation to repeated stimuli, and greater synchrony of population responses (larger ERPs) due to hyper-excitability of cortical responses. These phenotypes will impact auditory processing and lead to abnormal speech and language function and social communication, which are hallmark symptoms of FXS and other ASD (Ethridge et al., 2019; Wilkinson & Nelson, 2021; Smith et al., 2021). Similar deficits are also seen in the FC, which will impact hyperactivity and top-down executive function in a task-dependent manner (Sullivan & Brake, 2003).

### *4.4.2 Rationale for targeting mGluR5 and MMP-9 to treat Fmr1-KO related phenotypes in EEG*

Perhaps the most surprising result of this study is the lack of any target engagement by CTEP in terms of EEG phenotypes in *Fmr1* KO mice compared to vehicle. This is unlikely to be due to tachyphylaxis (Stoppel et al., 2021) as we did not find any effects after 1 or 10 days of either treatment method on EEG. In rodents, mGluR5 is expressed in much of the forebrain and in some parts of the midbrain and brain stem, including the auditory cortex, inferior colliculus, and medial nucleus of the trapezoid body (MNTB; Romano et al., 1995; Shigemoto et al., 1997; Lu, 2014; Curry et al., 2018). mGluR5 plays an important role in the auditory pathway and in auditory

processing. For instance, the MNTB is crucial for temporal processing of sound signals, as it receives fast and robust excitatory input from the calyx of Held as well as glycinergic and GABAergic inputs that provide fast inhibition, resulting in its ability to phase-lock to and follow rapid fluctuations in auditory signals (Forsythe, 1994; Taschenberger & von Gersdorff, 2000; Albrecht et al., 2014). Group 1 mGluRs, including mGluR5, play a crucial role in the brainstem, for they differentially modulate spontaneous and evoked synaptic inhibition (Curry et al., 2018). Furthermore, in the AC, presynaptic and postsynaptic group 1 mGluRs regulate excitation and inhibition in cross-regional and cross-laminar circuits (Lu, 2014), possibly resulting in hyper- or hypoexcitable cortical responses to auditory signals. *Fmr1*-KO mice exhibit a translationally-upregulated mGluR5 pathway. Previous studies demonstrated that administration of MPEP, an mGluR5 antagonist, in *Fmr1* KO mice rescued a range of behavioral symptoms associated with FXS, including audiogenic seizures in developing mice (AGS; Yan et al., 2005; de Vrij et al., 2008; Gandhi et al., 2014). Furthermore, blocking mGlur5 in the *Fmr1* KO mice rescued neuronal signaling and spine morphology in the hippocampus (de Vrij et al., 2008). Therefore, there was a strong justification to expect that CTEP treatment will modulate auditory responses, particularly those involving phase locking to temporally modulated stimuli in mice. However, surprisingly, there was no improvement of phenotype following CTEP administration in *Fmr1* KO mouse resting EEG or sound-evoked responses in the AC or FC, and in some cases, the phenotype increased (**Figure 4E, 4F, 4M, 4O**: see STP and chirp). It was crucial that all drug effects in *Fmr1* KO mice were directly compared to vehicle. Luu et al. (2020)

raised concerns about placebo effects in FXS: several clinical trials demonstrated improvements in FXS patients from placebo alone. Indeed, we found improvements in phenotype in the control condition in both resting and sound-evoked EEG measures (**Figures 3** and **4**), and these effects likely confounded interpretations of drug efficacy.

The EEG differences in WT and *Fmr1* KO mice are mostly in the gamma band, with increased resting gamma power, increased STP, and decreased ITPC for 40 Hz ASSR and chirp. Altered function of parvalbumin-positive (PV) inhibitory interneurons may underlie deficits in both abnormal gamma narrowband oscillations as well as broadband gamma power. Mice lacking NMDA receptor function on PV interneurons have abnormal baseline gamma power. Billingslea et al., (2014) showed that mGluR5 inhibition via MPEP resulted in worse outcomes in self-care and sociability behaviors and in auditory N1 evoked response latency in mice with PV neuron hypofunction due to loss of NMDA receptors. They suggest that MPEP in combination with increasing PV cell function may prove beneficial. Therefore, it is possible that we did not see effects of CTEP on EEG responses because PV neuron function remained abnormal. MMP-9 inhibition increases perineuronal net expression in PV neurons. Therefore, reduced gamma power seen with the combined CTEP + minocycline treatment may arise due to reduced mGluR5 activity in conjunction with improved PV cell function, as suggested by Billingslea et al., (2014). Future studies should test the hypothesis that positive allosteric modulators of PV neurons (Kourdougli et al., 2023) in combination with CTEP/MPEP reduce a broader range of EEG phenotypes in *Fmr1* KO mice.

mGluR5 activity promotes downstream production of MMP-9 in the brain (Gkogkas et al., 2014), which is elevated in FXS and is suggested to exacerbate the cleavage of perineuronal nets (PNNs), further disrupting synaptic excitability (Lovelace et al., 2016; Wen et al., 2018). Minocycline alone restores phase-locking to temporally modulated signals, namely chirp and ASSR, and reduces sound-induced gamma power (Lovelace et al., 2020). These findings led us to investigate the combination of CTEP and minocycline as a potential treatment of established resting and auditory hypersensitivity EEG biomarkers in FXS. Dual treatment may be the optimal way to target FXS deficits and reverse phenotypes, as it allows for the rescue of multiple categories of symptoms and promotes a more-encompassing treatment strategy, as demonstrated by Chadwick et al. (2024). In the present study, we found that CTEP + minocycline reduces gamma power in resting EEG but does not improve phase-locking to amplitude-modulated sounds, nor improve induced power, which, interestingly, is different than the effects of minocycline alone. It is possible that the differential effects of treatment (combined vs CTEP alone) may be due to dose-dependent effects (2 mg/kg CTEP vs. 1mg/kg CTEP in the combined treatment), for dose-dependent effects of MTEP, another mGluR5 antagonist, were identified in the primate model for FXS on working memory performance (Yang et al., 2021). Therefore, if this phenomenon is likewise present in the effect of CTEP on the mGluR5 pathway, it is possible that the CTEP dose we used in the CTEP-alone treatment is too high to produce positive results, whereas the lower dose used in the combined treatment has greater efficacy, but this would have to be further tested. Another possible reason for a strong non-specific effect is the method of administration. We chose oral

gavage to best mimic drug administration in humans, although in rodents it entails repeated exposure to an intensely stressful procedure. Studies demonstrating improvements following CTEP administration in rodent models of FXS (Michalon et al., 2012) and of Alzheimer's (Hamilton et al., 2016) reported delivering CTEP via subcutaneous and intraperitoneal injections, respectively. This suggests that route of administration may impact drug efficacy and treatment success, although this would have to be further tested.

**4.5 Conclusions**

This study is the first to use cortical EEG measures to assess CTEP treatment effects in *Fmr1* KO animal models of FXS. EEG phenotypes are objective and translatable biomarkers across species. We argue that EEG is a reliable and objective measure for drug effectiveness that offers an intermediate level of analyses between molecular signaling effects and behavioral effects. We suggest that it is crucial for a drug to demonstrate engagement with FXS-related EEG biomarkers in rodent models before being taken to clinical tests. Specifically, measures of gamma power, temporal processing in response to amplitude-modulated sound signals, and STP to noise burst presentations are measures that have demonstrated to show similar phenotypes in humans and mice. It is also important to identify EEG-based variability across patients to determine specific outcome measures that might be engaged by a particular drug in a trial.

Furthermore, we found that a combined treatment of CTEP and minocycline yields beneficial effects in FXS. Specifically, elevated gamma power present in FXS is

reduced as a result of CTEP and minocycline administration. These benefits are absent with CTEP alone (Figures 2 & 3) or with minocycline treatment alone (Lovelace et al., 2020). Minocycline rescues sound-evoked deficits in FXS but not resting phenotype. The benefits of dual-drug treatment on FXS have been previously demonstrated, in which gaboxadol and ibudilast in combination improved multiple behavioral phenotypes in FXS (Chadwick et al., 2024). We recommend future clinical treatments to target multiple biomechanistic pathways altered by FXS to produce optimal benefits, in combination with EEG.

Finally, we found benefits to targeting mGluR5 to reverse EEG symptoms in FXS when combined with targeting MMP-9 that are different from either drug alone. Given that targeting upregulated mGluR5 activity in FXS has had various results in previous literature, we recommend future studies to use the combined approach of targeting mGluR5 activity alongside MMP-9.

PRE-TREATMENT

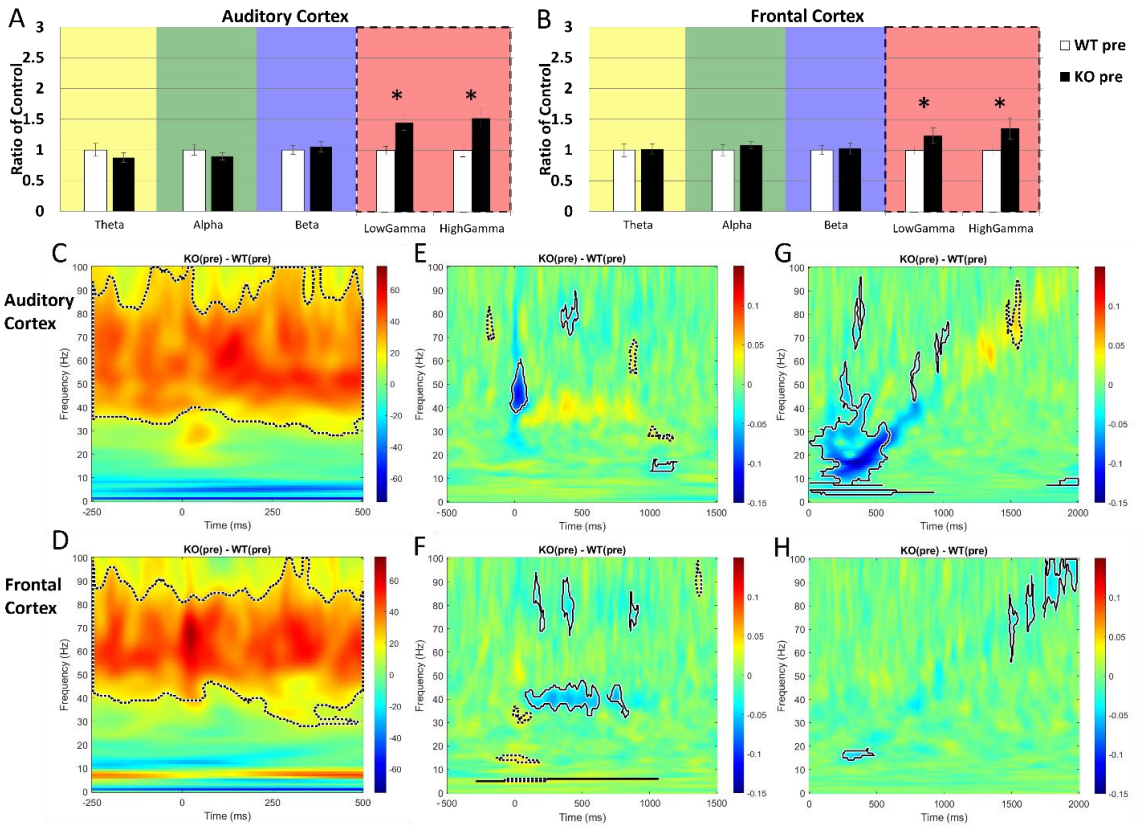


*Figure 4.2. Increased resting power, elevated STP, and reduced phase-locking were observed in Fmr1 KO mice compared to WT in the pre-drug condition*

(A,B) Mean spectral power density was calculated for AC and FC prior to any drug administration per genotype. Resting EEG power in the AC (A) and FC (B) show elevated low and high gamma power compared to WT. (C,D) STP during the presentation of 100 ms noise bursts presented at a rate of 1 Hz shows elevated low and high gamma power (area inside the dotted contour is significantly different across genotypes) in the Fmr1 KO compared to WT in the AC (C) and FC (D). (E,F) Phase-locking to the 40 Hz click train (ASSR) as measured using ITPC is reduced in AC (E) and FC (F) at 40 Hz. Each panel shows the difference in ITPC between WT and KO mice (KO-WT), with cooler colors indicating reduced phase-locking in the KO mice. Significant differences are shown as dotted line contours, with dashed lines indicating significantly higher ITPC values in the KO group compared to WT, and solid lines indicating significantly lower ITPC in the KO group compared to WT. (G,H) ITPC to the Chirp stimulus is reduced in the beta frequencies and increased in the high gamma in (G) AC and reduced in the low frequency and high gamma range in the (H) FC. These results are consistent with previously published Fmr1 KO vs WT EEG phenotypes recorded in the AC and FC. N=25 KO and 39 WT.

CTEP DAY 1

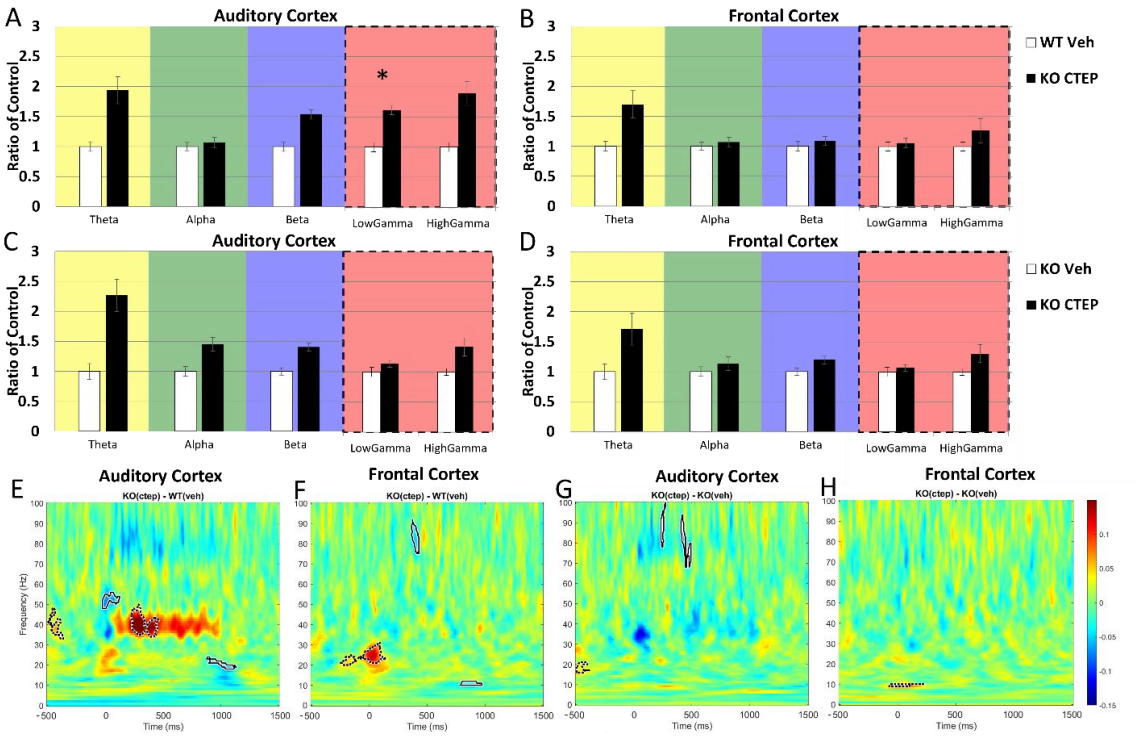


*Figure 4.3. Day 1 post-treatment with CTEP resulted in similar spectral power in resting EEG between KO and WT in the FC, but not in the AC where elevated low gamma power persists*

However, CTEP treatment is not significantly different from vehicle, suggesting an effect of handling, not treatment. (A-D) Mean power spectral density was calculated for AC and FC Day 1 post treatment onset. Resting EEG power in the (A) AC shows persisting elevated low gamma power in the KO treated with CTEP compared to WT treated with vehicle, while showing similar power across these groups in the (B) FC. Resting EEG power in the (C) AC and (D) FC of KO Day 1 post-CTEP onset compared to vehicle-treated KO shows no difference between drug and vehicle. I ITPC in response to a 40 Hz click train (ASSR) is elevated in the AC of KO mice treated with CTEP compared to WT treated with vehicle on Day 1 post treatment onset. (F) ITPC in the FC is similar between KO(ctep) and WT(veh). (G,F) However, ITPC in response to a 40 Hz click train (ASSR) is similar between KO(ctep) and KO(veh) in the (G) AC and (H) FC. This suggests that improvement shown in E, F is an effect of handling, not treatment. n = 9 KO CTEP, 9 WT veh, 8 KO veh.

CTEP DAY 10

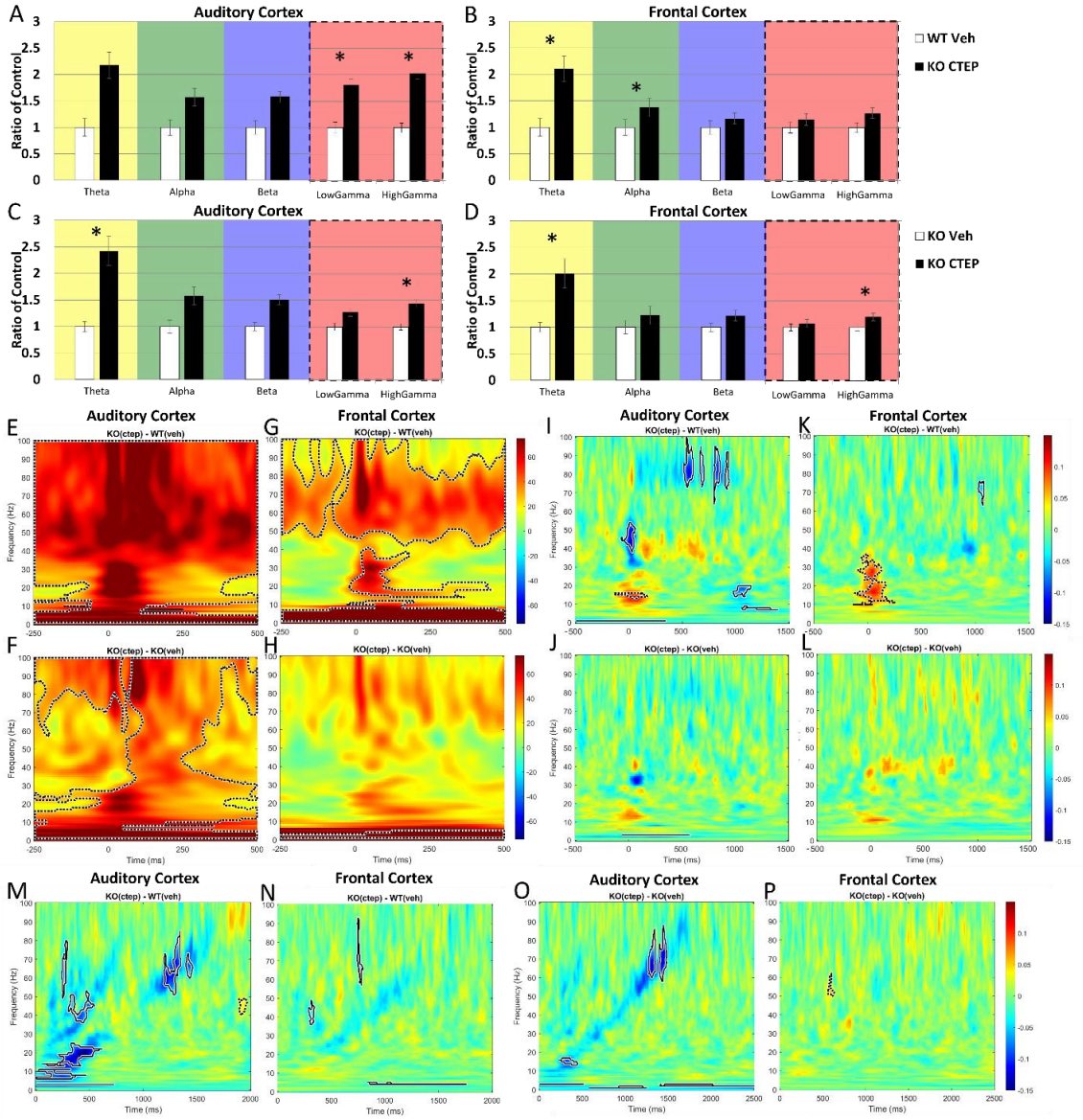
A
Auditory Cortex
Ratio of Control
Theta
Alpha
Beta
LowGamma
HighGamma
B
Frontal Cortex
WT Veh
KO CTEP
C
Auditory Cortex
D
Frontal Cortex
KO Veh
KO CTEP
E
Auditory Cortex
KO(ctep) - WT(veh)
G
Frontal Cortex
I
Auditory Cortex
K
Frontal Cortex
F
KO(ctep) - KO(veh)
H
J
L
Frequency (Hz)
Time (ms)
M
Auditory Cortex
N
Frontal Cortex
O
Auditory Cortex
P
Frontal Cortex

*Figure 4.4. Day 10 post-treatment with CTEP did not improve resting EEG or STP in the KO compared to WT but improved ITPC in the FC*

(A-D) Mean power density of AC and FC at Day 10 post treatment onset. Resting EEG power in the (A) AC of KO Day 10 post-CTEP onset compared to WT shows persisting elevated low and high gamma levels in the KO. (B) There is no difference in the FC between KO and WT in the gamma band, although theta and alpha power are elevated in the KO compared to WT. (C) Resting EEG power in the AC and of KO Day 10 post-CTEP onset compared to vehicle shows higher high gamma power in the CTEP-treated KO compared to vehicle, and increased power in theta. (D) The FC shows elevated power in the high gamma range and theta. This suggests that Day 10 post-treatment with CTEP in the KO is either worse or not different from vehicle treatment. MANCOVA was performed (genotype or treatment x freq, movement as covariate) and Bonferroni correction for multiple comparisons: *$p < 0.01$. (E,G) Day 10 post treatment onset with CTEP in the KO shows persisting elevated STP gamma power in the KO compared to WT. STP during the presentation of 100 ms noise bursts presented at a rate of 1 Hz shows elevated power in the Fmr1 KO treated with CTEP across all frequencies in tI(E) AC and (G) FC compared to WT, including in low frequencies which was not present in the pre-drug comparison (Fig. 1). (F,H) Compared to vehicle, treatment with CTEP did not reduce STP in the (H) FC and increased STP in the (F) AC. (I-L) Phase-locking to the 40 Hz click train (ASSR) as measured using ITPC in the CTEP-treated KO (I,L) and in the vehicle-treated KO (J,L). ITPC in CTEP-treated KO is similar to WT in the FC (K) but remains lower than WT in the AC (I). (J,L) Treatment with CTEP results in similar ITPC levels as vehicle, suggesting no treatment effect. (M) ITPC to the chirp stimulus in the CTEP-treated *Fmr1* KO compared to WT-vehicle in the AC (KO-ctep minus WT-veh). Significant clusters around the chirp indicate lower ITPC in the KO group compared to WT group around ~1-20 Hz and ~60-80 Hz amplitude modulation. (N) ITPC to the chirp stimulus in the CTEP-treated *Fmr1* KO is similar to WT-vehicle in the FC (no significant clusters around the chirp stimulus). (O) CTEP treatment in KO mice resulted in lower ITPC compared to vehicle treatment in the AC (clusters around ~15 Hz and ~60-80 Hz of the chirp stimulus indicating lower ITPC in the KO-ctep group compared to KO-veh group). (P) ITPC to the chirp stimulus in the CTEP-treated *Fmr1* KO is similar to KO-vehicle in the FC (no significant clusters around the chirp stimulus). n = 9 KO CTEP, 9 WT veh, 8 KO veh.

CTEP + MINO DAY 1

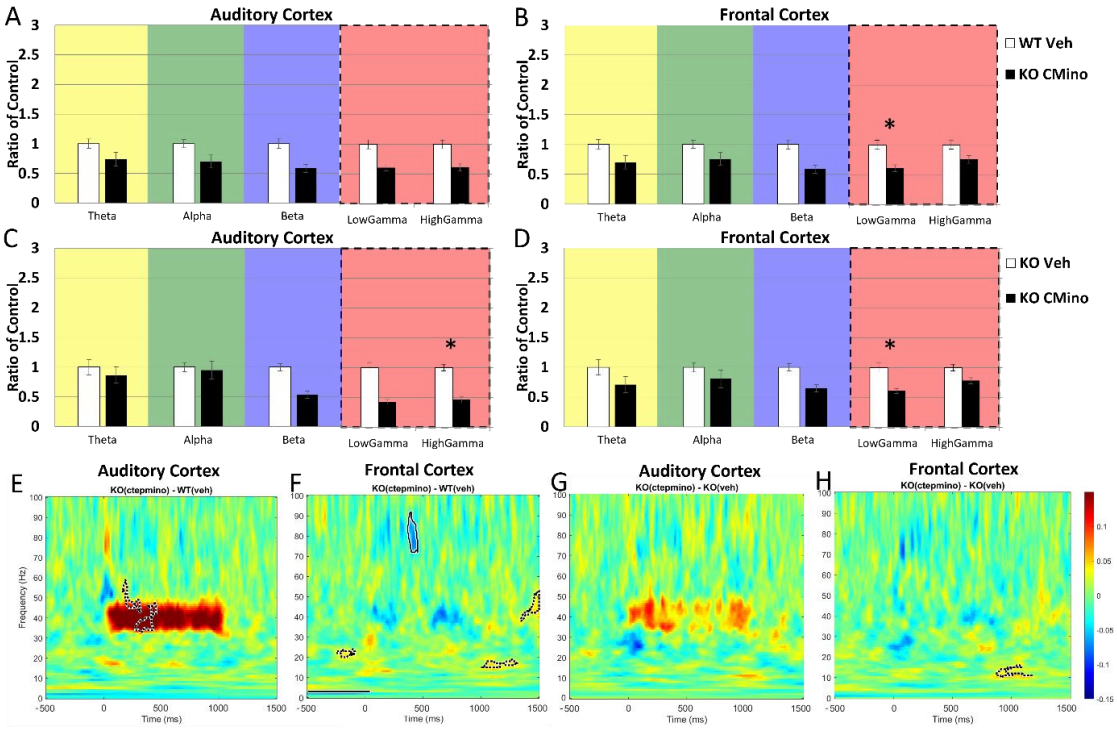


*Figure 4.5. Day 1 post-treatment with CTEP + minocycline in the KO resulted in similar resting spectral power as the WT(veh) in the AC and FC*

Treatment with CTEP + minocycline reduced high gamma and low gamma power in the AC and FC, respectively, compared to vehicle. (A-D) Mean power density was calculated for AC and FC Day 1 post treatment onset. CTEP + minocycline results in similar EEG levels in KO compared to WT in the (A) AC and (B) FC. Resting EEG power in the (C) AC and (D) FC of KO Day 1 post-CTEP + minocycline onset compared to vehicle-treated KO shows reduced high and low gamma power, respectively. (E) ITPC in response to a 40 Hz click train (ASSR) is elevated in the AC of KO mice treated with CTEP + minocycline compared to WT treated with vehicle on Day 1 post treatment onset. (F) ITPC in the FC is similar between KO(ctep + minocycline) and WT(veh). (G,F) However, ITPC in response to a 40 Hz click train (ASSR) is similar between KO(ctep + minocycline) and KO(veh) in the (G) AC and (H) FC, suggesting an effect of handling, not treatment. n = 8 KO CTEP + minocycline, 9 WT veh, 8 KO veh.

CTEP + MINO DAY 10

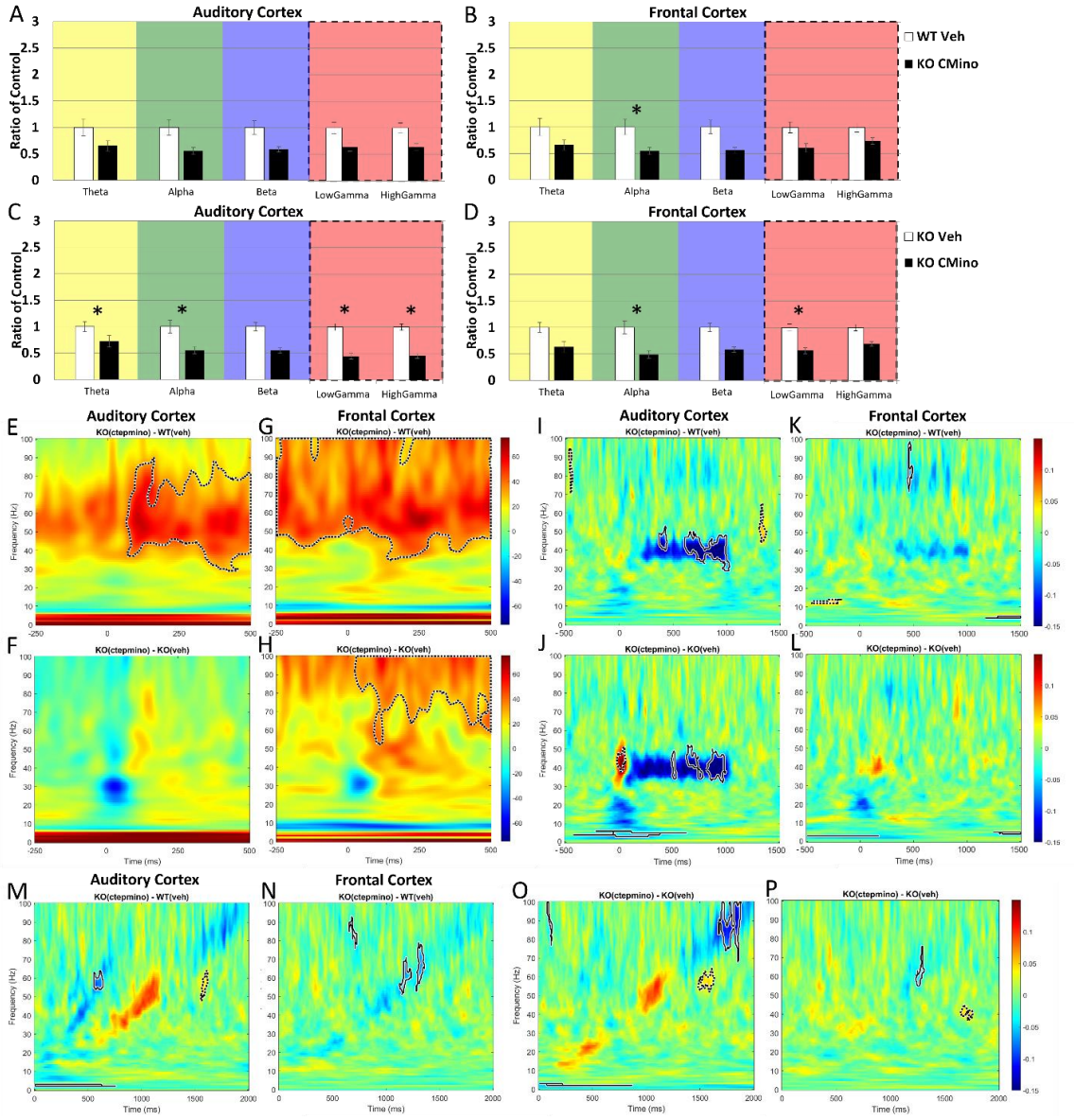

*Figure 4.6. Day 10 post-treatment with CTEP + minocycline restored low and high gamma levels in the AC and FC in KO compared to WT, while not improving STP nor ITPC*

(A-D) Mean power density of AC and FC at Day 10 post treatment onset. KO treated with CTEP + minocycline show similar resting EEG power in the (A) AC and (B) lower alpha power in the FC, with low and high gamma bands power being similar. (C,D) Compared to vehicle, treatment with CTEP + minocycline significantly (C) lowered low and high gamma power in the AC and (D) reduced low gamma power in the FC, suggesting a treatment effect restoring low and high gamma power to WT levels. Additionally, (C) theta and alpha power are reduced in the AC and (D) alpha power is reduced in the FC in the treatment group compared to vehicle. MANCOVA was performed (genotype or treatment x freq, movement as covariate) and Bonferroni correction for multiple comparisons: *$p < 0.01$. (E,G) Day 10 post treatment onset with CTEP + minocycline in the KO shows persisting elevated STP gamma power in the KO compared to WT. STP during the presentation of 100 ms noise bursts presented at a rate of 1 Hz shows elevated power in the Fmr1 KO treated with CTEP + minocycline across gamma frequencies in tI(E) AC and (G) FC compared to WT. (F,H) Compared to vehicle, treatment with CTEP did not reduce STP in the (F) AC and increased STP in the (H) FC. (I-L) Phase-locking to the 40 Hz click train (ASSR) as measured using ITPC in the CTEP + minocycline-treated KO (I,L) and in the vehicle-treated KO (J,L). ITPC in CTEP + minocycline-treated KO is (I) reduced compared to WT in the AC and (K) similar to WT in the FC. (J,L) Treatment with CTEP + minocycline results in (J) lower ITPC levels in the AC compared to vehicle and (L) similar ITPC levels as vehicle, suggesting no treatment effect. (M) ITPC to the chirp stimulus in the *Fmr1* KO mice treated with CTEP + minocycline was similar to WT-vehicle levels in the AC (no significant clusters). (N) *Fmr1* KO mice treated with CTEP + minocycline showed lower ITPC compared to WT-vehicle levels in the FC (significant cluster in the ~50-70 Hz amplitude modulation range). (O,P) CTEP + minocycline treatment in KO mice resulted in lower ITPC compared to vehicle treatment in the (O) AC (cluster in the ~70-100 Hz amplitude modulation range) and (P) FC (cluster at ~60 Hz amplitude modulation). n = 8 KO CTEP + minocycline, 9 WT veh, 8 KO veh.

## References


Albrecht, O., Dondzillo, A., Mayer, F., Thompson, J.A. and Klug, A., 2014. Inhibitory projections from the ventral nucleus of the trapezoid body to the medial nucleus of the trapezoid body in the mouse. *Frontiers in neural circuits*, *8*, p.83.

Balmer, T.S., 2016. Perineuronal nets enhance the excitability of fast-spiking neurons. *ENeuro*, *3*(4).

Bear, M.F., Huber, K.M. and Warren, S.T., 2004. The mGluR theory of fragile X mental retardation. *Trends in neurosciences*, *27*(7), pp.370-377.

Bhakar, A.L., Dölen, G. and Bear, M.F., 2012. The pathophysiology of fragile X (and what it teaches us about synapses). *Annual review of neuroscience*, *35*, pp.417-443.

Bhaskaran, A.A., Gauvrit, T., Vyas, Y., Bony, G., Ginger, M. and Frick, A., 2023. Endogenous noise of neocortical neurons correlates with atypical sensory response variability in the Fmr1−/y mouse model of autism. Nature Communications, 14(1), p.7905.

Billingslea, E.N., Tatard-Leitman, V.M., Anguiano, J., Jutzeler, C.R., Suh, J., Saunders, J.A., Morita, S., Featherstone, R.E., Ortinski, P.I., Gandal, M.J. and Lin, R., 2014. Parvalbumin cell ablation of NMDA-R1 causes increased resting network excitability with associated social and self-care deficits. *Neuropsychopharmacology*, *39*(7), pp.1603-1613.

Bilousova, T.V., Dansie, L., Ngo, M., Aye, J., Charles, J.R., Ethell, D.W. and Ethell, I.M., 2009. Minocycline promotes dendritic spine maturation and improves behavioural performance in the fragile X mouse model. *Journal of medical genetics*, *46*(2), pp.94-102.

Chadwick, W., Angulo-Herrera, I., Cogram, P., Deacon, R.J., Mason, D.J., Brown, D., Roberts, I., O'Donovan, D.J., Tranfaglia, M.R., Guilliams, T. and Thompson, N.T., 2024. A novel combination treatment for fragile X syndrome predicted using computational methods. *Brain Communications*, *6*(1), p.fcad353.

Chuang, S.C., Zhao, W., Bauchwitz, R., Yan, Q., Bianchi, R. and Wong, R.K., 2005. Prolonged epileptiform discharges induced by altered group I metabotropic glutamate receptor-mediated synaptic responses in hippocampal slices of a fragile X mouse model. *Journal of Neuroscience*, *25*(35), pp.8048-8055.

Crawford DC, Acuña JM, Sherman SL. FMR1 and the Fragile X syndrome: human genome epidemiology review. *Genet Med*. 2001;3:359-371.

Croom, K., Rumschlag, J.A., Erickson, M.A., Binder, D.K. and Razak, K.A., 2023. Developmental delays in cortical auditory temporal processing in a mouse model of Fragile X syndrome. *Journal of Neurodevelopmental Disorders*, *15*(1), p.23.

Curry, R.J., Peng, K. and Lu, Y., 2018. Neurotransmitter-and release-mode-specific modulation of inhibitory transmission by group I metabotropic glutamate receptors in central auditory neurons of the mouse. *Journal of Neuroscience*, *38*(38), pp.8187-8199.

de Vrij, F.M., Levenga, J., Van der Linde, H.C., Koekkoek, S.K., De Zeeuw, C.I., Nelson, D.L., Oostra, B.A. and Willemsen, R., 2008. Rescue of behavioral phenotype and neuronal protrusion morphology in Fmr1 KO mice. *Neurobiology of disease*, *31*(1), pp.127-132.

Dölen G, Osterweil E, Rao BS, Smith GB, Auerbach BD, Chattarji S, Bear MF. Correction of fragile X syndrome in mice. Neuron. 2007 Dec 20;56(6):955-62. doi: 10.1016/j.neuron.2007.12.001. PMID: 18093519; PMCID: PMC2199268.

Dölen, G. and Bear, M.F., 2008. Role for metabotropic glutamate receptor 5 (mGluR5) in the pathogenesis of fragile X syndrome. *The Journal of physiology*, *586*(6), pp.1503-1508.

Dziembowska, M., Pretto, D.I., Janusz, A., Kaczmarek, L., Leigh, M.J., Gabriel, N., Durbin-Johnson, B., Hagerman, R.J. and Tassone, F., 2013. High MMP-9 activity levels in fragile X syndrome are lowered by minocycline. *American journal of medical genetics Part A*, *161*(8), pp.1897-1903.

Dziembowska, M., 2023. How dendritic spines shape is determined by MMP-9 activity in FXS. *International Review of Neurobiology*, *173*, pp.171-185.

Erickson, C.A., Shaffer, R.C., Will, M. et al. Brief Report: A Double-Blind, Placebo-Controlled, Crossover, Proof-of-Concept Study of Minocycline in Autism Spectrum Disorder. J Autism Dev Disord (2023). https://doi.org/10.1007/s10803-023-06132-1

Ethell, I.M. and Ethell, D.W., 2007. Matrix metalloproteinases in brain development and remodeling: synaptic functions and targets. *Journal of neuroscience research*, *85*(13), pp.2813-2823.

Ethridge, L.E., White, S.P., Mosconi, M.W., Wang, J., Pedapati, E.V., Erickson, C.A., Byerly, M.J. and Sweeney, J.A., 2017. Neural synchronization deficits linked to cortical hyper-excitability and auditory hypersensitivity in fragile X syndrome. *Molecular Autism*, *8*, pp.1-11.

Ethridge, L.E., De Stefano, L.A., Schmitt, L.M., Woodruff, N.E., Brown, K.L., Tran, M., Wang, J., Pedapati, E.V., Erickson, C.A. and Sweeney, J.A., 2019. Auditory EEG biomarkers in fragile X syndrome: clinical relevance. *Frontiers in integrative neuroscience*, *13*, p.60.

Forsythe, I.D., 1994. Direct patch recording from identified presynaptic terminals mediating glutamatergic EPSCs in the rat CNS, in vitro. *The Journal of physiology*, *479*(3), pp.381-387.

Gandhi, R.M., Kogan, C.S. and Messier, C., 2014. 2-Methyl-6-(phenylethynyl) pyridine (MPEP) reverses maze learning and PSD-95 deficits in Fmr1 knock-out mice. *Frontiers in Cellular Neuroscience*, *8*, p.70.

Gkogkas, C.G., Khoutorsky, A., Cao, R., Jafarnejad, S.M., Prager-Khoutorsky, M., Giannakas, N., Kaminari, A., Fragkouli, A., Nader, K., Price, T.J. and Konicek, B.W., 2014. Pharmacogenetic inhibition of eIF4E-dependent Mmp9 mRNA translation reverses fragile X syndrome-like phenotypes. *Cell reports*, *9*(5), pp.1742-1755.

Gore, S.V., James, E.J., Huang, L.C., Park, J.J., Berghella, A., Thompson, A.C., Cline, H.T. and Aizenman, C.D., 2021. Role of matrix metalloproteinase-9 in neurodevelopmental deficits and experience-dependent plasticity in Xenopus laevis. *Elife*, *10*, p.e62147.

Hamilton, A., Vasefi, M., Vander Tuin, C., McQuaid, R.J., Anisman, H. and Ferguson, S.S., 2016. Chronic pharmacological mGluR5 inhibition prevents cognitive impairment and reduces pathogenesis in an Alzheimer disease mouse model. *Cell reports*, *15*(9), pp.1859-1865.

Huber, K.M., Gallagher, S.M., Warren, S.T. and Bear, M.F., 2002. Altered synaptic plasticity in a mouse model of fragile X mental retardation. *Proceedings of the National Academy of Sciences*, *99*(11), pp.7746-7750.

Janusz, A., Miłek, J., Perycz, M., Pacini, L., Bagni, C., Kaczmarek, L. and Dziembowska, M., 2013. The Fragile X mental retardation protein regulates matrix metalloproteinase 9 mRNA at synapses. *Journal of Neuroscience*, *33*(46), pp.18234-18241.

Jin P, Warren ST. Understanding the molecular basis of fragile X syndrome. Hum Mol Genet. 2000 Apr 12;9(6):901-8. doi: 10.1093/hmg/9.6.901. PMID: 10767313.

Jonak, C.R., Lovelace, J.W., Ethell, I.M., Razak, K.A. and Binder, D.K., 2020. Multielectrode array analysis of EEG biomarkers in a mouse model of Fragile X Syndrome. *Neurobiology of disease*, *138*, p.104794.

Kokash, J., Alderson, E.M., Reinhard, S.M., Crawford, C.A., Binder, D.K., Ethell, I.M. and Razak, K.A., 2019. Genetic reduction of MMP-9 in the Fmr1 KO mouse partially rescues prepulse inhibition of acoustic startle response. *Brain research*, *1719*, pp.24-29.

Kourdougli, N., Suresh, A., Liu, B., Juarez, P., Lin, A., Chung, D.T., Sams, A.G., Gandal, M.J., Martínez-Cerdeño, V., Buonomano, D.V. and Hall, B.J., 2023. Improvement of sensory deficits in fragile X mice by increasing cortical interneuron activity after the critical period. *Neuron*, *111*(18), pp.2863-2880.

Knoth, I.S. and Lippé, S., 2012. Event-related potential alterations in fragile X syndrome. *Frontiers in Human Neuroscience*, *6*, p.264.

Kremer EJ, Pritchard M, Lynch M, Yu S, Holman K, Baker E, Warren ST, Schlessinger D, Sutherland GR, Richards RI. Mapping of DNA instability at the fragile X to a trinucleotide repeat sequence p(CCG)n. *Science*. 1991;252:1711-1714.

Laroui, A., Galarneau, L., Abolghasemi, A., Benachenhou, S., Plantefève, R., Bouchouirab, F.Z., Lepage, J.F., Corbin, F. and Çaku, A., 2022. Clinical significance of matrix metalloproteinase-9 in Fragile X Syndrome. *Scientific Reports*, *12*(1), p.15386.

Lindemann, L., Jaeschke, G., Michalon, A., Vieira, E., Honer, M., Spooren, W., Porter, R., Hartung, T., Kolczewski, S., Büttelmann, B. and Flament, C., 2011. CTEP: a novel, potent, long-acting, and orally bioavailable metabotropic glutamate receptor 5 inhibitor. *Journal of Pharmacology and Experimental Therapeutics*, *339*(2), pp.474-486.

Lovelace JW, Wen TH, Reinhard S, Hsu MS, Sidhu H, Ethell IM, Binder DK, Razak KA. Matrix metalloproteinase-9 deletion rescues auditory evoked potential habituation deficit in a mouse model of Fragile X Syndrome. Neurobiol Dis. 2016 May;89:126-35. doi: 10.1016/j.nbd.2016.02.002. Epub 2016 Feb 2. PMID: 26850918; PMCID: PMC4785038.

Lovelace, J.W., Ethell, I.M., Binder, D.K. and Razak, K.A., 2018. Translation-relevant EEG phenotypes in a mouse model of Fragile X Syndrome. *Neurobiology of disease*, *115*, pp.39-48.

Lovelace, J.W., Ethell, I.M., Binder, D.K. and Razak, K.A., 2020. Minocycline treatment reverses sound evoked EEG abnormalities in a mouse model of Fragile X Syndrome. *Frontiers in neuroscience*, *14*, p.550324.

Lu, Y., 2014. Metabotropic glutamate receptors in auditory processing. *Neuroscience*, *274*, pp.429-445.

Luján, R., Roberts, J.D.B., Shigemoto, R., Ohishi, H. and Somogyi, P., 1997. Differential plasma membrane distribution of metabotropic glutamate receptors mGluR1α, mGluR2 and mGluR5, relative to neurotransmitter release sites. *Journal of chemical neuroanatomy*, *13*(4), pp.219-241.

Luu, S., Province, H., Berry-Kravis, E., Hagerman, R., Hessl, D., Vaidya, D., Lozano, R., Rosselot, H., Erickson, C., Kaufmann, W.E. and Budimirovic, D.B., 2020. Response to placebo in fragile X syndrome clinical trials: an initial analysis. *Brain sciences*, *10*(9), p.629.

Magnowska, M., Gorkiewicz, T., Suska, A., Wawrzyniak, M., Rutkowska-Wlodarczyk, I., Kaczmarek, L. and Wlodarczyk, J., 2016. Transient ECM protease activity promotes synaptic plasticity. *Scientific reports*, *6*(1), p.27757.

Maris, E. and Oostenveld, R., 2007. Nonparametric statistical testing of EEG-and MEG-data. *Journal of neuroscience methods*, *164*(1), pp.177-190.

McBride, S.M., Choi, C.H., Wang, Y., Liebelt, D., Braunstein, E., Ferreiro, D., Sehgal, A., Siwicki, K.K., Dockendorff, T.C., Nguyen, H.T. and McDonald, T.V., 2005. Pharmacological rescue of synaptic plasticity, courtship behavior, and mushroom body defects in a Drosophila model of fragile X syndrome. *Neuron*, *45*(5), pp.753-764.

Michalon A, Sidorov M, Ballard TM, Ozmen L, Spooren W, Wettstein JG, Jaeschke G, Bear MF, Lindemann L. Chronic pharmacological mGlu5 inhibition corrects fragile X in adult mice. Neuron. 2012 Apr 12;74(1):49-56. doi: 10.1016/j.neuron.2012.03.009. PMID: 22500629; PMCID: PMC8822597.

Niswender, C.M. and Conn, P.J., 2010. Metabotropic glutamate receptors: physiology, pharmacology, and disease. *Annual review of pharmacology and toxicology*, *50*, pp.295-322.

Oberle I, Rousseau F, Heitz D, Kretz C, Devys D, Hanauer A, Boue J, Bertheas MF, Mandel JL. Instability of a 550-base pair DNA segment and abnormal methylation in fragile X syndrome. Science. 1991;252:1097-1102.

Pirbhoy, P.S., Rais, M., Lovelace, J.W., Woodard, W., Razak, K.A., Binder, D.K. and Ethell, I.M., 2020. Acute pharmacological inhibition of matrix metalloproteinase-9 activity during development restores perineuronal net formation and normalizes auditory processing in Fmr1 KO mice. *Journal of neurochemistry*, *155*(5), pp.538-558.

Rais M, Binder DK, Razak KA, Ethell IM. Sensory Processing Phenotypes in Fragile X Syndrome. ASN Neuro. 2018 Jan-Dec;10:1759091418801092. doi: 10.1177/1759091418801092. PMID: 30231625; PMCID: PMC6149018.

Rankin-Gee, E.K., McRae, P.A., Baranov, E., Rogers, S., Wandrey, L. and Porter, B.E., 2015. Perineuronal net degradation in epilepsy. *Epilepsia*, *56*(7), pp.1124-1133.

Razak, K.A., Binder, D.K. and Ethell, I.M., 2021. Neural correlates of auditory hypersensitivity in fragile X syndrome. *Frontiers in Psychiatry*, *12*, p.720752.

Reinhard, S.M., Razak, K. and Ethell, I.M., 2015. A delicate balance: role of MMP-9 in brain development and pathophysiology of neurodevelopmental disorders. *Frontiers in cellular neuroscience*, *9*, p.280.

Romano, C., Sesma, M.A., McDonald, C.T., O'malley, K., van den Pol, A.N. and Olney, J.W., 1995. Distribution of metabotropic glutamate receptor mGluR5 immunoreactivity in rat brain. *Journal of Comparative Neurology*, *355*(3), pp.455-469.

Rotschafer SE, Trujillo MS, Dansie LE, Ethell IM, Razak KA. Minocycline treatment reverses ultrasonic vocalization production deficit in a mouse model of Fragile X Syndrome. Brain Res. 2012 Feb 23;1439:7-14. doi: 10.1016/j.brainres.2011.12.041. Epub 2011 Dec 31. PMID: 22265702.

Rotschafer, S. and Razak, K., 2013. Altered auditory processing in a mouse model of fragile X syndrome. *Brain research*, *1506*, pp.12-24.

Rumschlag, J.A., Lovelace, J.W. and Razak, K.A., 2021. Age-and movement-related modulation of cortical oscillations in a mouse model of presbycusis. *Hearing Research*, *402*, p.108095.

Schneider A, Leigh MJ, Adams P, Nanakul R, Chechi T, Olichney J, Hagerman R, Hessl D. Electrocortical changes associated with minocycline treatment in fragile X syndrome. J Psychopharmacol. 2013 Oct;27(10):956-63. doi: 10.1177/0269881113494105. Epub 2013 Aug 27. PMID: 23981511; PMCID: PMC4962861.

Shigemoto, R., Kinoshita, A., Wada, E., Nomura, S., Ohishi, H., Takada, M., Flor, P.J., Neki, A., Abe, T., Nakanishi, S. and Mizuno, N., 1997. Differential presynaptic localization of metabotropic glutamate receptor subtypes in the rat hippocampus. *Journal of Neuroscience*, *17*(19), pp.7503-7522.

Sidhu, H., Dansie, L.E., Hickmott, P.W., Ethell, D.W. and Ethell, I.M., 2014. Genetic removal of matrix metalloproteinase 9 rescues the symptoms of fragile X syndrome in a mouse model. *Journal of Neuroscience*, *34*(30), pp.9867-9879.

Smith, E.G., Pedapati, E.V., Liu, R., Schmitt, L.M., Dominick, K.C., Shaffer, R.C., Sweeney, J.A. and Erickson, C.A., 2021. Sex differences in resting EEG power in Fragile X Syndrome. *Journal of psychiatric research*, *138*, pp.89-95.

Stawarski, M., Stefaniuk, M. and Wlodarczyk, J., 2014. Matrix metalloproteinase-9 involvement in the structural plasticity of dendritic spines. *Frontiers in neuroanatomy*, *8*, p.68.

Stoppel, L.J., Osterweil, E.K. and Bear, M.F., 2017. The mGluR theory of fragile X: from mice to men. In *Fragile X Syndrome* (pp. 173-204). Academic Press.

Stoppel, D.C., McCamphill, P.K., Senter, R.K., Heynen, A.J. and Bear, M.F., 2021. mGluR5 negative modulators for fragile X: treatment resistance and persistence. *Frontiers in Psychiatry*, *12*, p.718953.

Sullivan, R.M. and Brake, W.G., 2003. What the rodent prefrontal cortex can teach us about attention-deficit/hyperactivity disorder: the critical role of early developmental events on prefrontal function. *Behavioural brain research*, *146*(1-2), pp.43-55.

Taschenberger, H. and Von Gersdorff, H., 2000. Fine-tuning an auditory synapse for speed and fidelity: developmental changes in presynaptic waveform, EPSC kinetics, and synaptic plasticity. *Journal of Neuroscience*, *20*(24), pp.9162-9173.

Toledo, M.A., Wen, T.H., Binder, D.K., Ethell, I.M. and Razak, K.A., 2019. Reversal of ultrasonic vocalization deficits in a mouse model of Fragile X Syndrome with minocycline treatment or genetic reduction of MMP-9. *Behavioural brain research*, *372*, p.112068.

Tucker, B., Richards, R.I. and Lardelli, M., 2006. Contribution of mGluR and Fmr1 functional pathways to neurite morphogenesis, craniofacial development and fragile X syndrome. *Human molecular genetics*, *15*(23), pp.3446-3458.

Van der Molen, M.J.W., Van der Molen, M.W., Ridderinkhof, K.R., Hamel, B.C.J., Curfs, L.M.G. and Ramakers, G.J.A., 2012. Auditory and visual cortical activity during selective attention in fragile X syndrome: a cascade of processing deficiencies. *Clinical Neurophysiology*, *123*(4), pp.720-729.

Verkerk AJ, Pieretti M, Sutcliffe JS, Fu YH, Kuhl DP, Pizzuti A, Reiner O, Richards S, Victoria MF, Zhang FP *et al*. Identification of a gene (FMR-1) containing a CGG repeat coincident with a breakpoint cluster region exhibiting length variation in fragile X syndrome. *Cell*. 1991;65:905-914.

Wang, J., Ethridge, L.E., Mosconi, M.W., White, S.P., Binder, D.K., Pedapati, E.V., Erickson, C.A., Byerly, M.J. and Sweeney, J.A., 2017. A resting EEG study of neocortical hyperexcitability and altered functional connectivity in fragile X syndrome. *Journal of neurodevelopmental disorders*, *9*, pp.1-12.

Warren ST, Nelson DL. Advances in molecular analysis of fragile X syndrome. *J. Am. Med. Assoc*. 1994;271:536-542.

Wen TH, Afroz S, Reinhard SM, Palacios AR, Tapia K, Binder DK, Razak KA, Ethell IM. Genetic Reduction of Matrix Metalloproteinase-9 Promotes Formation of Perineuronal Nets Around Parvalbumin-Expressing Interneurons and Normalizes Auditory Cortex Responses in Developing Fmr1 Knock-Out Mice. Cereb Cortex. 2018 Nov 1;28(11):3951-3964. doi: 10.1093/cercor/bhx258. PMID: 29040407; PMCID: PMC6188540.

Wen, T.H., Lovelace, J.W., Ethell, I.M., Binder, D.K. and Razak, K.A., 2019. Developmental changes in EEG phenotypes in a mouse model of fragile X syndrome. *Neuroscience*, *398*, pp.126-143.

Wilkinson, C.L. and Nelson, C.A., 2021. Increased aperiodic gamma power in young boys with Fragile X Syndrome is associated with better language ability. *Molecular autism*, *12*, pp.1-15.

Yan QJ, Rammal M, Tranfaglia M, Bauchwitz RP. Suppression of two major Fragile X Syndrome mouse model phenotypes by the mGluR5 antagonist MPEP. Neuropharmacology. 2005 Dec;49(7):1053-66. doi: 10.1016/j.neuropharm.2005.06.004. Epub 2005 Jul 27. PMID: 16054174.

Yang, S.T., Wang, M., Galvin, V., Yang, Y. and Arnsten, A.F., 2021. Effects of blocking mGluR5 on primate dorsolateral prefrontal cortical neuronal firing and working memory performance. *Psychopharmacology*, *238*, pp.97-106.

Yu S, Pritchard M, Kremer E, Lynch M, Nancarrow J, Baker E, Holman K, Mulley JC, Warren ST, Schlessinger D *et al*. Fragile X genotype characterized by an unstable region of DNA. *Science*. 1991;252:1179-1181.

# Chapter 5: Conclusion

In the first study, we found that inactivating PV neurons reduced gamma power in right and left AC, and it elevated theta power during locomotion traces. Furthermore, we found elevated ongoing non-phase-locked power in the beta band and lower frequencies during noise burst presentation in the right AC, where PV neurons were chemogenetically inactivated. Phase-locking of the ASSR during the presentation of click trains at 40 Hz is reduced with PV neuron inactivation in both hemispheres of the AC. These findings point to the role of PV neurons in promoting resting gamma power and reducing movement-related theta and sound-related beta power in the AC. Furthermore, they demonstrate that PV neurons promote the 40-Hz ASSR in AC, and this phenomenon is projected bilaterally. There was no effect on the gap-ASSR, which instead showed a deficit in the second study presented with midbrain deletion of FMRP, pointing to the role of midbrain expression of FMRP in encoding gaps in noise. This finding suggests that speech and gap-encoding deficits present in FXS may be associated with loss of midbrain expression of FMRP. In the third study, we found that resting deficits in FXS are rescued by the combined treatment with CTEP, an mGluR5 antagonist, and minocycline, an MMP-9 inhibitor, suggesting combined drug treatments as an effective approach to treat FXS. In summary, we found differential contributions of the auditory cortex and subcortical auditory regions in their impact on FXS-related phenotypes, and targeting multiple mechanisms is key to treating the symptoms of FXS collectively.

The advantages of using EEG in the present studies are several. First, the high temporal resolution of EEG allows for large population-level recordings of the brain that reflect the activity of multiple contributing brain sources. Through the high temporal

fidelity of this technique, we recorded ASSR in auditory and frontal regions, an effective and highly translatable method in neuropathophysiology across species. This brings us to the second strength of our study, which is the remarkable similarity of FXS-related EEG biomarkers between humans and mouse models of FXS, generating high translatability of these findings to the clinical realm. We further established translatability by recording from the right AC in all our present studies, which has been shown to elicit stronger ASSR compared to the left AC (Ross et al., 2005; Grent-‘t-Jong et al., 2021; Toso et al., 2024).

Future directions of this research are to test additional combinations of drug treatments on EEG phenotypes of FXS. For example, gaboxadol and ibudilast in combination improved multiple behavioral phenotypes in FXS (Chadwick et al., 2024), and should next be tested in EEG to identify potential preclinical advantages. Additionally, the direct role of PV neurons in FXS phenotypes has yet to be elucidated. A follow up to the second and third chapter would be to delete FMRP from all PV-expressing neurons in the brain, as well as regional deletions of FMRP from PV cell, i.e., in the midbrain vs forebrain. Finally, the receptor and channel subtypes crucial to FXS phenotypes have yet to be further explored. Disruption of n-methyl-d-aspartic acid receptors (NMDAR) on PV interneurons results in autism-like phenotypes, namely increases in N1 latency, impaired sociability, and reduced mating vocalizations (Saunders et al., 2013). An interesting follow-up study would be to explore the potential contribution of PV neuron-specific NMDA receptors on auditory function and processing and to identify whether their expression is regulated by FMRP.

## References


Chadwick, W., Angulo-Herrera, I., Cogram, P., Deacon, R.J., Mason, D.J., Brown, D., Roberts, I., O'Donovan, D.J., Tranfaglia, M.R., Guilliams, T. and Thompson, N.T., 2024. A novel combination treatment for fragile X syndrome predicted using computational methods. *Brain Communications*, *6*(1), p.fcad353.

Grent-'t-Jong, T., Gajwani, R., Gross, J., Gumley, A.I., Krishnadas, R., Lawrie, S.M., Schwannauer, M., Schultze-Lutter, F. and Uhlhaas, P.J., 2021. 40-Hz auditory steady-state responses characterize circuit dysfunctions and predict clinical outcomes in clinical high-risk for psychosis participants: a magnetoencephalography study. *Biological Psychiatry*, *90*(6), pp.419-429.

Ross, B., Herdman, A.T. and Pantev, C., 2005. Right hemispheric laterality of human 40 Hz auditory steady-state responses. *Cerebral cortex*, *15*(12), pp.2029-2039.

Toso, A., Wermuth, A.P., Arazi, A., Braun, A., Grent, T., Uhlhaas, P.J. and Donner, T.H., 2024. 40 Hz Steady-State Response in Human Auditory Cortex Is Shaped by GABAergic Neuronal Inhibition. *Journal of Neuroscience*.